Coherent terahertz Smith-Purcell radiation generated by the microbunched electron beam

Huibo Zhang

Hertford College, Oxford



Thesis submitted in fulfilment of the requirements for the degree of

Doctor of Philosophy at the University of Oxford

Trinity Term, 2018

Coherent terahertz Smith-Purcell radiation generated by the microbunched electron beam

Huibo Zhang
Hertford College, Oxford

Thesis submitted in fulfilment of the requirements for the degree of Doctor of Philosophy at the University of Oxford

Trinity Term, 2018

Abstract

The main objective of the thesis is to investigate the generation of coherent terahertz (THz) Smith-Purcell radiation using microbunched electron beams. Several ways of generating electron microbunches were considered and a method to monitor the separation between microbunches was developed. Microbunch trains, with picosecond (or sub-picosecond) periodicities, were generated through a variety of methods, including the modulation of a long electron bunch in a plasma channel, direct generation of microbunches from a photocathode (at KEK-LUCX, Japan), and the modulation of a long bunch (with an initial density modulation) using the longitudinal space charge forces during its propagation in the beamline (at TTX, China). The method to monitor the periodicity of microbunch trains was based on the analysis of coherent Smith-Purcell radiation and experiments were carried out with two microbunches to confirm its validity. Furthermore, the generation of coherent THz Smith-Purcell radiation using microbunch trains with tunable periodicities was investigated. The properties of the radiation generated were studied. Numerical simulations and experimental measurements have confirmed that the microbunching of electron bunches results in the intensity of the generated coherent Smith-Purcell radiation concentrating at around the microbunch frequency. These proof of concept studies demonstrate the possibility of the generation of high power, broadly tunable THz radiation using microbunched electron beams.

Acknowledgements

Writing up this thesis is like finishing a long journey, which gives me the opportunity to remember and think about all the things happened along the way. I realised that there are so many people who deserve acknowledgement here for their help in the past four years.

First I would like to thank my supervisor Dr Ivan Konoplev. He has been a great inspiration to me over the whole process of the thesis. I also would like to thank Dr George Doucas, and the discussions with him always make me benefit. Thanks also go to previous group members: Dr Andrew Lancaster and Dr Faissal Bakkali Taheri, and current group member: Ms Hannah Harrison. I have been very lucky to work together with them.

This work would not have been possible without the access to the accelerator facilities: KEK-LUCX in Japan and TTX in China. For the KEK-LUCX team, I would like to thank Dr Alex Aryshev and Dr Mikhail Shevelev. For the TTX team, I must thank Professor Chuanxiang Tang, Professor Lixin Yan, Dr Dan Wang, Dr Xiaolu Su and Yifan Liang. The experiments which were carried out at nights make me unforgettable. A special thanks goes to Dr Jonathan Smith and Dr Konstantin Lekomtsev, who helped me a lot on the VSim and CST simulations. I am also glad to have some wonderful JAI colleagues. The discussions with them during lunch and coffee breaks make me feel like in a big family.

I am also extremely grateful to my parents for their constant support. Studying abroad means I can't spend much time with them, even when they needed me. Finally, last but not least, I would like to thank my beautiful wife Bohui. To support my work, she undertook most of the responsibilities on looking after our son George, who was born few months ago in Oxford. Without her support I would never have been able to finish this thesis.

Contents

1 Introduction **1**

1.1 Overview of terahertz radiation 3

1.2 THz radiation generation driven by microbunched electron beams 6

1.3 Generation of a train of microbunches 9

1.4 Outline of the thesis 12

2 Theoretical and numerical studies of coherent Smith-Purcell radiation **13**

2.1 Introduction of Smith-Purcell radiation 13

2.2 Analytical description 16

2.2.1 Radiation generated by an electron bunch 16

2.2.2 Effect of beam microbunching 18

2.3 Numerical studies of cSPr in the near-field region in VSim 21

2.3.1 Introduction of PIC simulation VSim 21

2.3.2 Simulation setup 22

2.3.3 Radiation generated by a single bunch 23

2.3.4 Radiation generated by microbunch trains 26

2.4 Numerical studies of cSPr in the far-field region in CST 28

2.4.1 Introduction of PIC simulation CST 28

2.4.2 Simulation setup 28

2.4.3 cSPr from a single bunch 29

2.4.4 cSPr from a train of microbunches 31

2.5 Summary 34

3 The generation of a train of microbunches in a plasma 35

3.1 Basic principle and analytical model 36

3.1.1 Basic principle 36

3.1.2 Theoretical analysis 37

3.1.3 Dependence of modulation on the parameters of beam and plasma . . 39

3.2 Numerical studies of beam modulation 45

3.2.1 Dependence of modulation on bunch profiles 45

3.2.2 Comparison of theoretical analysis with numerical predictions 48

3.3 Numerical studies of beam collimation and propagation in vacuum area . . . 49

3.3.1 Beam collimation from plasma channel to vacuum region 49

3.3.2 Beam propagation in vacuum drift area 51

3.3.3 Dependence of beam modulation depth on plasma parameters 53

3.4 THz radiation generated by plasma modulated microbunches 56

3.5 Summary 58

4 Generation of microbunch trains in photocathode RF gun and the monitoring of microbunch separation 59

4.1 Generation of microbunch trains at KEK-LUCX 60

4.1.1 An introduction to the KEK-LUCX facility 60

4.1.2 Variation of the microbunch separation 62

4.1.3 Basis of the measurement of the microbunch separation 65

4.2 Experiments with two microbunches 67

4.2.1 Experimental setup 67

4.2.2 Spectrum of cSPr 69

4.2.3 Tuning the microbunch separation 71

4.3 Microbunch separation measurement 74

4.3.1 Measurement of the separation based on experimental data 74

4.3.2 Comparison of measurement with analytical predictions 77

4.4 Discussion 79

4.4.1 Multiple-frequency measurements 80

4.4.2 Analysis for two different bunches 81
4.4.3 Possibilities for trains with more microbunches 83
4.5 Summary 83

5 THz radiation generated by microbunch trains with tunable periodicities 85
5.1 An introduction to the TTX facility 85
5.2 Experiments with a single bunch 87
5.2.1 Experimental setup 87
5.2.2 Confirming cSPr from a single bunch 89
5.3 Experiments with microbunch trains 92
5.3.1 cTR from microbunch trains 92
5.3.2 cSPr from microbunch trains 95
5.4 Summary and Discussion 100

6 Summary and suggestions for future work 102

A Radiation from a bunch of charged particles 105

B Beam envelope model 107

C Linear wakefield theory 109

D THz detectors 117

Bibliography 120

List of Figures

1.1 A diagram of the electromagnetic spectrum. 1

1.2 A schematic of the radiation generated by a train of electron microbunches. . 7

1.3 Dependence of $I(\nu)/I_1(\nu)$ on radiation frequency ν for a train of 2, 4, and 8 microbunches with a fixed microbunch separation Δt. 8

1.4 Photograph of the KEK-LUCX facility. 9

1.5 Photograph of the TTX facility. 10

2.1 A schematic of Smith-Purcell radiation. 14

2.2 A schematic of the coordinates used in the surface current model. 16

2.3 Comparison of the bandwidth of Smith-Purcell radiation (observed at 1 THz) considering (dashed line) and without considering the microbunching effect (solid line). 19

2.4 The square of form factor $|F(\nu)|^2$ as a function of frequency for a single Gaussian bunch with longitudinal lengths σ of 0.1 ps, 0.3 ps, and 0.5 ps. . . 20

2.5 Normalised density distributions of a train of microbunches (in same total charge) with microbunch separation of 1 ps (a) and the corresponding form factors (b). The length σ of each single Gaussian microbunch is 0.1 ps. . . . 20

2.6 One computational cycle of the PIC simulation. 22

2.7 Schematic diagram of the VSim simulation showing THz radiation generation. 23

2.8 Snapshots of the distribution of magnetic field B_y at simulation time $t = 20$ ps, 40 ps, 60 ps, and 80 ps. 24

2.9 Normalised transient waveform of B_y observed at 90 degrees. 25

2.10 Comparison of the form factor obtained from theoretical predictions (dashed line) and the FFT of the signal shown in Figure 2.9 (solid line). 25
2.11 Comparison of the form factor obtained from theoretical predictions (dashed lines) and the FFT of the signal from the VSim simulation (solid lines) for a train consisting 4 identical microbunches with separations of 1 ps, 1.33 ps, 1.67 ps, and 2 ps. 26
2.12 A schematic of the CST simulation showing THz radiation generation. . . . 29
2.13 Normalised transient waveform of field $B_\phi(t)$ observed at an angle θ of 80° (a) and the corresponding FFT $B_\phi(\nu)$ (b). 30
2.14 Normalised spectrum of the radiation generated by a single bunch as a function of the observation angle θ and the emission frequency (observation distance=1 m, azimuthal angle ϕ=0°). 31
2.15 Comparison of radiation obtained from the CST simulation and theoretical calculation using a train consisting of 4 identical microbunches with separations of 1 ps, 1.33 ps, 1.67 ps, and 2 ps. 32

3.1 Schematic diagram of the evolution of charge distribution showing the self-modulation instability of a long electron bunch in a plasma (w_0 is the beam transverse size, λ_p is the plasma wavelength). 36
3.2 Normalised longitudinal charge density distributions of beams with trapezoidal profile (a) and Gaussian profile (b). 40
3.3 Beam modulation parameter σ_r/σ_{r0} plotted as a function of the position along the plasma channel. 42
3.4 Dependence of function $f(\xi)$ on different bunch profiles (plasma period T_p=1 ps). 43
3.5 Beam modulation parameter σ_r/σ_{r0} plotted as a function of the position along the plasma channel. 44
3.6 Numerical simulations of the bunch modulation after propagating a distance of 2.1 cm, for different plasma densities and bunch profiles. 46

3.7 Numerical simulations of the beam modulation for Gaussian profile (left) and haf-Gaussian profile (right) after propagating the distance of 1 cm (a, d), 2 cm (b, e) and 3 cm (c, f) in a plasma with a period T_p of 1 ps (λ_p=300 μm). 47
3.8 Comparison of the charge density distributions on axis obtained from theoretical analysis (a) and VSim simulation (b). The plasma wavelength λ_p is 300 μm. 48
3.9 A schematic of the VSim simulation showing the beam propagation through a collimator. 50
3.10 Normalised longitudinal charge distribution along the beam propagation direction for originally modulated beam and collimated beam. 50
3.11 Comparison of the bunch profiles (top) and the corresponding form factors (bottom) after propagating 1 cm (black dashed line) and 10 cm (solid red line) in vacuum when the beam energy is 50 MeV (a, b), 20 MeV (c, d), and 10 MeV (e, f). 51
3.12 Charge distributions of a collimated beam with propagation distances of 2.1 cm (a), 2.3 cm (b), 2.6 cm (c), 2.8 cm (d), and 3.0 cm (e) in a plasma with a plasma period of 1 ps. 54
3.13 Charge distributions of a collimated beam with propagation distances of 2.3 cm (a), 2.8 cm (b), 3.0 cm (c), 3.3 cm (d), and 3.5 cm (e) in a plasma with a plasma period of 0.67 ps. 54
3.14 Charge distributions of a collimated beam with propagation distances of 2.3 cm (a), 3.0 cm (b), 3.2 cm (c), 3.5 cm (d), and 3.7 cm (e) in a plasma with a plasma period of 0.5 ps. 54
3.15 Comparison of the charge density distributions (left) and their corresponding bunch form factors (right) for beams shown in Figure 3.12. 55
3.16 Comparison of the charge density distributions (left) and their corresponding bunch form factors (right) for beams shown in Figure 3.13. 55
3.17 Comparison of the charge density distributions (left) and their corresponding bunch form factors (right) for beams shown in Figure 3.14. 55

3.18 Contour plots of the charge distributions of microbunch trains after beam collimation with microbunch periodicities of (a) 1 ps, (b) 0.67 ps, and (c) 0.5 ps. Beam energy=50 MeV. 56
3.19 Normalised spectra of the radiation generated by microbunch trains after beam collimation with microbunch periodicities of 1 ps, 0.67 ps, and 0.5 ps. . 57

4.1 Schematic layout of the KEK-LUCX facility. 60
4.2 Schematic diagram of the laser splitting system. 61
4.3 Schematic diagram of the generation and acceleration of two microbunches. . 62
4.4 Lorentz factor γ of an electron at the exit of the accelerating region as a function of the initial RF phase ϕ_0 of the electron at the cathode surface. . . 64
4.5 Final RF phase ϕ of an electron at the end of the accelerating region as a function of the initial RF phase ϕ_0 of the electron at the cathode surface. . . 65
4.6 Dependence of $G_2(\nu_0, \Delta t)$ on the microbunch separation Δt between two microbunches at an observation frequency ν_0. 66
4.7 A schematic of experimental setup which includes the photocathode gun, 3.6-cell RF cavity, grating, sapphire window, Michelson interferometer, and detector. 67
4.8 Photograph of the Michelson interferometer system. 68
4.9 Schematic diagram of the grating with a sawtooth profile used at KEK-LUCX. 68
4.10 Normalised spectrum of the transition radiation signal generated by a single bunch. 69
4.11 Normalised spectrum of the cSPr signal generated by a single bunch and measured at a detection angle of 90 degrees. 70
4.12 Normalised spectrum of the cSPr signal generated by two microbunches and measured at a detection angle of 90 degrees. 71
4.13 Total charge of the two microbunches measured (ICT counts) for different RF phases as a function of the position of mirror M_2. 72
4.14 Smith-Purcell radiation intensity measured (FCT counts) at 90 degrees for different RF phases as a function of the position of mirror M_2. 72

4.15 MBSM intensity measured at 90 degrees for a set of RF phases and as a function of the initial microbunch separation varying from 0 to 22 ps. 74
4.16 Intensity of the cSPr signal measured and predicted showing the dependence of the radiation on the separation between the two microbunches. 75
4.17 Microbunch separations calculated from measurement. 76
4.18 Comparison of the normalised intensity of the cSPr signal measured and predicted after the corrections of the microbunch separation. 77
4.19 Dependence of the final microbunch separation on the initial separation between microbunches. 78
4.20 Multi-frequency measurements to identify the microbunch separation. 80
4.21 Dependence of $G_2(\nu, \Delta t)$ on the microbunch separation Δt between two microbunches having different distributions of charges, at a given frequency ν. . 82

5.1 Schematic layout of the beamline for the generation of microbunch trains at the TTX facility. 86
5.2 A schematic of the laser bunching system at the TTX facility. 87
5.3 A schematic of the experimental setup at TTX. 88
5.4 Photograph of the Michelson interferometer system 88
5.5 Photograph of the THz chamber and the sawtooth grating. 89
5.6 Normalised spectrum of the cSPr signal generated by a single bunch. 90
5.7 Photograph of the wire grid polariser (left) and the WAP filter (right) used in the experiment. 91
5.8 Radiation intensity versus the angle of the rotation of the polariser with and without a WAP filter in front of the detector. 92
5.9 Typical temporal profile of the microbunched beam at the TTX facility. . . . 93
5.10 Typical spectrum of the cTR signal generated by a train of microbunches. . 94
5.11 Normalised spectra of the cTR signal generated by a train of microbunches at RF gun phases of 20°, 30°, 40°, 50°, and 55°. 94
5.12 A schematic of the setup for the measurement of cSPr at different detection angles. 96

5.13 Radiation intensity of cSPr versus RF gun phase. 97
5.14 Photograph of the chamber where grating was positioned inside at previous experiment. 98
5.15 Normalised spectrum of the cSPr signal generated by microbunch trains. . . 99

A.1 A schematic of radiation from a bunch of particles. 105

C.1 Comparison of the transverse wakefield component $f(\xi)$ for bunches with different linear rise times. 115
C.2 Comparison of the transverse wakefield component $f(\xi)$ for bunches with different sinusoidal rise times. 116

D.1 (a) Scanning electron micrograph of a planar Schottky diode; (b) Schematic cross-section of the diode. 118
D.2 Measured current-voltage characteristic of the zero-bias WR-10 Schottky detector diode. 119

List of Tables

1.1 THz sources 6

2.1 Beam and grating parameters 23

3.1 Beam and plasma parameters 40

4.1 KEK-LUCX parameters 61

5.1 Comparison of the line width of cTR generated by microbunch trains 95

5.2 Comparison of the line width of cSPr generated by microbunch trains. 100

Abbreviations

cSPr coherent Smith-Purcell radiation

cTR coherent Transition Radiation

EM electromagnetic

FFT fast Fourier transform

FWHM full width at half maximum

GFW Grating of Finite Width

KEK High Energy Accelerator Research Organization

LUCX Laser Undulator Compact X-ray source facility

PIC particle-in-cell

PML perfectly matched layer

RF radiofrequency

SMI self-modulation instability

TTX Tsinghua Thomson scattering X-ray source

THz terahertz

ZBD Zero Bias Diode

Chapter 1

Introduction

The electromagnetic radiation in the terahertz (THz) frequency range bridges the gap between microwaves (wavelengths up to 3 millimetres) and far infrared (from 10 micrometres) in the electromagnetic spectrum, as shown in Figure 1.1, with typical frequencies ranging from 0.1 to 30 THz. In terms of the photon energy of THz radiation, it covers the range from around 0.4 to 124 milli-electronvolt, which corresponds to the energy levels of the bands of many materials, such as the shallow impurities in semiconductors and rotational interactions in gases [1, 2]. Due to some of its features, such as: (a) its significant penetration depth of many non-metallic and non-polar materials; (b) strong absorption by some organic materials and by water at certain frequencies, the THz region has acquired great importance over a wide range of topics in research and industry.

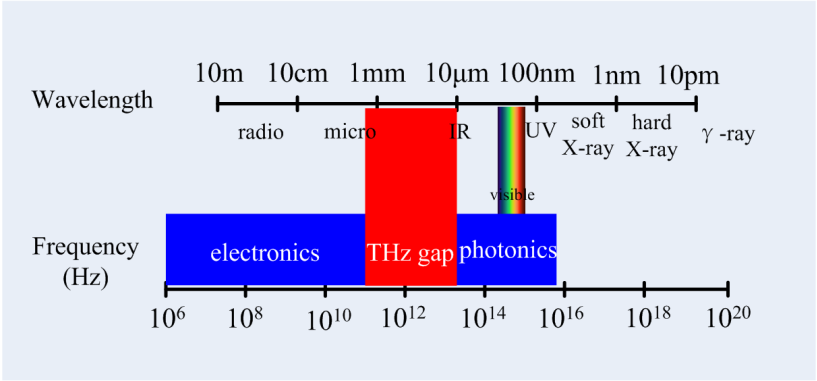


Figure 1.1: A diagram of the electromagnetic spectrum.

THz technology has been used for security and defence applications, such as the detection of explosives [3, 4], personnel and security mail screening [5], and the detection of noxious gases [6, 7]. THz radiation has been used in many other areas, including in communications [8], astronomy [9], chemistry [10], and condensed matter physics [11]. Studies and designs of THz sources and detectors have been carried out for decades. Several positive results have been achieved, for example, THz time-domain spectroscopy, boosting the development of THz technologies.

THz radiation is in the region where the use of open path optical techniques (short wave) and waveguides (long wave) overlap. At around 10 micrometres (μm), systems can be designed similar to those used in the visible or near infrared regions with lenses, prisms, and mirrors. In this case, spectroscopy can be performed with diffraction gratings or Michelson interferometers. With the increase in wavelength, the size of the optical components must also be increased to avoid diffraction losses. This makes traditional optical methods difficult to apply across the whole THz spectrum region.

On the other hand, at the low frequency region of THz spectrum, THz radiation can be generated using conventional vacuum electronic devices, such as travelling-wave tubes and backward-wave oscillators. In order to increase the operating frequency, the dimensions of the devices must be decreased, which leads to the challenges associated with high power handling and radiofrequency (RF) breakdowns. The radiation power achievable by broadly accessible THz devices falls to milliwatt (mW) and microwatt (μW) levels at both the long and short wavelength regions, which results the long recognised THz technological "gap".

In this chapter, I will first review some of the available THz sources. Subsequently, THz radiation generated by microbunched electron beams driven by accelerators will be discussed. Some techniques for the generation of relativistic electron microbunch trains with ps or sub-ps periodicity will also be introduced.

1.1 Overview of terahertz radiation

Based on different radiation mechanisms, THz radiation sources can be classified into thermal emission sources, photonics based sources (gas lasers, quantum cascade lasers and laser photoconductive antennas), electronics based sources (typically vacuum tubes driven by mildly relativistic beams), and accelerator based sources (such as synchrotrons and FELs) [12, 13].

Thermal emission sources

According to Planck's radiation law, a black body with a temperature above absolute zero (0 K) will emit electromagnetic radiation over a certain spectral range. The relation between radiation peak wavelength λ_{peak} and temperature T is $\lambda_{\text{peak}}T = 2.898 \times 10^{-3}$m.K. THz sources based on natural thermal emission include mercury arc lamps and silicon carbide globars, with a typical output power is on the level of μW [1].

Photonics based sources

There are two main THz laser sources, gas lasers and quantum cascade lasers (QCLs). The frequency of a THz gas laser depends on the rotational transitions of a polar gas molecule in its excited vibrational state. Typical commercially available systems were developed by Edinburgh Instruments in the 1980s [14, 15]. By selecting different FIR molecules and CO_2 pump lines, the operating frequency of this type of system can range from 0.25 THz to 7.5 THz (not continuously) with typical power up to 150 mW.

Unlike the operating principle of conventional semiconductor lasers (the recombination of electrons and holes), QCLs use only electrons in the lasing process. The electrons move through a superlattice consisting of a periodic series of thin layers of varying materials. If the population inversion between two different energy levels is satisfied, laser emission can be achieved [16]. THz QCLs were developed quickly and this was largely due to the advancement of semiconductor bandgap engineering. Nowadays THz QCLs cover the frequencies range

from 1 to 5 THz, and their output power can be more than 100 mW in CW operation [17] and with peak powers in excess of 1 W at 3.4 THz [18]. Although cryogenic cooling is still required, with appropriate electrical bias and strong magnetic field (above 16 T), the laser operation temperature can be up to 225 K at 3 THz [19].

Another method for the generation of THz radiation is to use laser photoconductive antennas. When an ultrafast femtosecond laser pulse (typically 100 fs or shorter) illuminates a semiconductor material, for instance, Gallium Arsenide (GaAs), it will create charge carriers (electron-hole pairs). The electric current is accelerated and transmitted across the antenna by applying an electric bias. THz radiation is induced by the short current pass with a typical frequency range from 0.05 to 4 THz. This generation method has been used in THz time-domain spectroscopy.

Vacuum electronics based sources

Vacuum tubes are one of the most common used sources of EM radiation. Their generation mechanism is based on the conversion of the kinetic energy of electrons into electromagnetic radiation. One type of vacuum tube is the travelling-wave tube. They normally operate in the radiation frequencies range from 0.1 to 1 THz, and are capable of generating power from 10^6 W (at 0.1 THz) to 10^{-3} W (at 1 THz). To optimise the energy conversion, a slow wave structure (SWS) is required, which ensures the phase velocity of the waves is slow enough to interact and exchange energy with the propagating electrons along the length of interaction region. The dimension of the SWS should be on the scale of the operating wavelength, in the THz region this requires structures with dimensions around mm or sub-mm, which puts pressure on the fabrication technique. Another limitation factor is that the circuit losses increase dramatically when the operating frequency goes up, leading to overheating of the system at high power regimes of operation. All of these challenges limit the output power of vacuum tubes based on SWS in the THz frequency region.

Another kind of vacuum electronic source is the gyrotron. The typical operating frequency of a gyrotron ranges from 0.1 to 1 THz with power from 10^7 W (at 0.1 THz) to 10^{-3}

W (at 1 THz). The radiation frequency is determined by the external magnetic fields. In some gyrotrons with superconducting coils, the magnetic field achieved can be more than 10 T, allowing its operation in THz region. In order to maintain the radiation power while increasing the radiation frequency, high order circular modes need to be excited. This requires precise control of the position of the electron beam and the interaction region. These devices have limited tunability (below 1%) and relatively low power in the THz range.

Accelerator based sources

With the recent developments in accelerator technology around the world, there has been a growing interest in the generation of THz radiation driven by accelerators [20, 21, 22, 23, 24, 25, 26]. Compared with mildly relativistic beams, the space charge effects of relativistic electron beams can be inhibited dramatically. This means that charge density can be increased. If the bunch size is compressed small enough (compare with the operating wavelength), coherent radiation can be generated (see Chapter 2 for detailed explanations). The attractive features of such sources include tunability over a broad frequency and their power range, from 0.1 THz to 10 THz and from 10 W to 10^9 W (pulse regime), respectively.

This group of accelerator-based sources includes synchrotron radiation sources, free-electron lasers (FELs), transition radiation sources and diffraction radiation sources. Synchrotron radiation is emitted when relativistic charged particles are deflected by a magnet (or magnets). FELs generate radiation in a similar way but using the bunching effect of the beam during the radiation process, and this leads to a narrowband coherent radiation. They can operate over a broad range of wavelengths by changing the period of undulators or the relativistic factor of the beam. The radiation produced emerges in a narrow cone and has a characteristic polarization. The spectrum generated by synchrotrons and FELs can range from millimetre waves to X-rays.

Transition radiation is a form of electromagnetic radiation emitted when charged particles pass through the interface of two different media (the refractive indexes are different) [27]. As the electric fields generated by the particles are different in the two media, according to

the law of energy conservation, the particles have to emit energy which forms the radiation. One of the main limitations is that the beam intersects with the target which may lead to the destruction of the beam or the target.

Diffraction radiation happens when a charged particle moves in close proximity to an inhomogeneous structure [28]. Unlike the generation of transition radiation, the particles don't come into direct contact with the target, so the beam is not destroyed. If the inhomogeneity is periodic, for example, a metal grating, Smith-Purcell radiation is observed (see Chapter 2 for details).

Table 1.1: THz sources

Type	Frequency (THz)	Power(W)	Size
Thermal emission	Broadband	$10^{-6} - 10^{-5}$	Small
Lasers	0.25 - 7.5	$10^{-5} - 10$	Desktop
Vacuum electronics	0.1 - 1	$10^{-6} - 10^{7}$ †	Medium
Accelerator based	0.2 - 10	$10^{-5} - 10^{9}$ ††	Large

† CW and pulsed
†† Average and pulsed

In summary, it can be seen from Table 1.1 that accelerator based THz radiation sources have advantages over other THz radiation sources in terms of tunability and radiation power. The focus of this thesis will be on the generation of THz radiation generated by relativistic electron beams driven by accelerators.

1.2 THz radiation generation driven by microbunched electron beams

Coherent radiation generated by a short (compared with the operating wavelength) relativistic electron bunch is usually broadband (up to tens of THz), and the radiation intensity is proportional to the square of the number of electrons in the bunch [29, 30, 31, 32]. In some cases it is difficult to drive a femtosecond high charge (above 1 nC) beam through the system when the beam has relatively low energy (<10 MeV) due to the strong dispersion

caused by space charge effects, which limits the radiation intensity. To solve these issues, a train of electron microbunches with relatively low charge within each microbunch can be utilised.

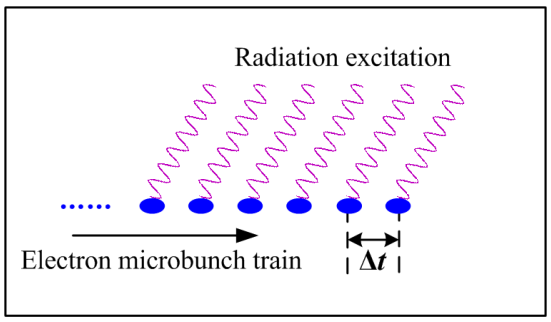


Figure 1.2: A schematic of the radiation generated by a train of electron microbunches.

To illustrate the radiation generated by microbunch trains, I consider that the radiation is excited by a train consisting of M identical microbunches with an equal separation of Δt, as shown in Figure 1.2. Assuming the radiation wave generated by the i^{th} (i=1,2,...,M) microbunch, at an observation frequency ν in the far-field region, the electric field can be written as:

$$E_i = E_{0i} \exp(-j\theta_i), \theta_i = kz_i + 2\pi\nu t_i \tag{1.1}$$

where E_{0i} is the amplitude of the wave, $\theta_i = kz_i + 2\pi\nu t_i$ is the phase, ν is the observation frequency, $k = 2\pi\nu/c$ is the wave number, z_i is the propagation distance and t_i is the propagation time of the radiation from the i^{th} microbunch. The total electric field E of the waves emitted by microbunch trains is the superposition of the electric field generated by each microbunch given by $E = \sum_{i=1}^{M} E_i$. As the microbunches are identical, the electric field generated by each microbunch is equal (E_{01}=E_{02}=...=E_0). The phase difference of the two waves excited by two adjacent microbunches can be written as $\Delta\theta = \theta_i - \theta_{i-1} = 2\pi\nu\Delta t$.

In the frequency domain, the relationship between the total radiation energy $I(\nu)$ ($\propto |E|^2$) and radiation energy from a single microbunch $I_1(\nu)$ ($\propto |E_0|^2$) at a given observation frequency ν is given by Equation 1.2 (detailed derivation can be seen in Chapter 2):

$$\frac{I(\nu)}{I_1(\nu)} = \frac{\sin^2(M\pi\nu\Delta t)}{\sin^2(\pi\nu\Delta t)} \tag{1.2}$$

Assuming a train of M microbunches with a fixed microbunch separation Δt, the ratio of radiation energy from microbunch trains and from a single microbunch as a function of radiation frequency ν is shown in Figure 1.3. It indicates that the peaks of radiation generated by microbunch trains correspond to the microbunch frequency ν_b ($\nu_b = 1/\Delta t$) and its harmonics $n\nu_b$ ($\nu = n/\Delta t, n = 1, 2, 3...$). The more microbunches in the train, the narrower the radiation distribution bandwidth around the peaks. Also the maximum of $I(\nu)/I_1(\nu)$ is equal to M^2, meaning that increasing the number of microbunches results in a significant increase of the total radiation energy.

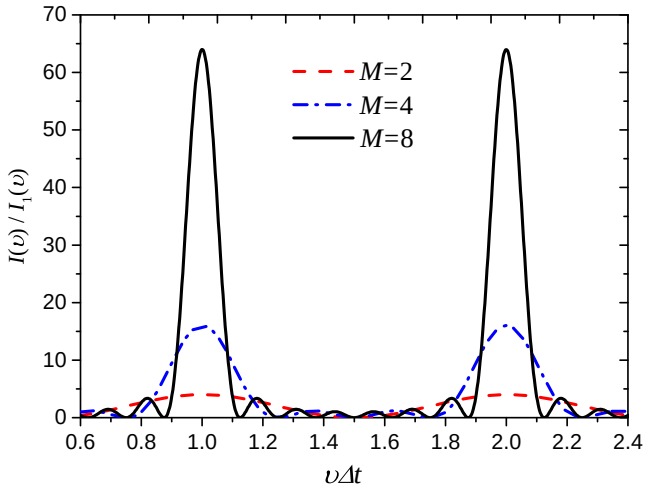


Figure 1.3: Dependence of $I(\nu)/I_1(\nu)$ on radiation frequency ν for a train of 2, 4, and 8 microbunches with a fixed microbunch separation Δt.

For microbunch trains with short single microbunch size (compare with the operating wavelength), coherent radiation can be observed. The radiation frequency is determined by the Fourier components of the modulated beam. The radiation spectrum can be changed by adjusting the periodicity of microbunches, thus leading to observation of a narrowband, tunable, coherent THz radiation for practical applications. Hence, it is possible to achieve high power THz radiation generated by a train of microbunches, which otherwise would be challenging for a single bunch with the same total charge due to space charge effects.

1.3 Generation of a train of microbunches

One of the challenges is to generate relativistic electron microbunch trains with ps or sub-ps periodicity. Some of the currently available and promising future techniques are discussed follow.

Direct modulation at the photocathode: KEK-LUCX

A photoinjector typically consists of a specially shaped accelerating structure with the photocathode positioned at one end of the structure. The photocathode is made from light-sensitive material from which the electrons are extracted via the photoemission process when an electromagnetic wave (normally laser) strikes the surface. The emitted electrons are accelerated to relativistic energies by the RF or DC electric fields generated in the accelerating structure.

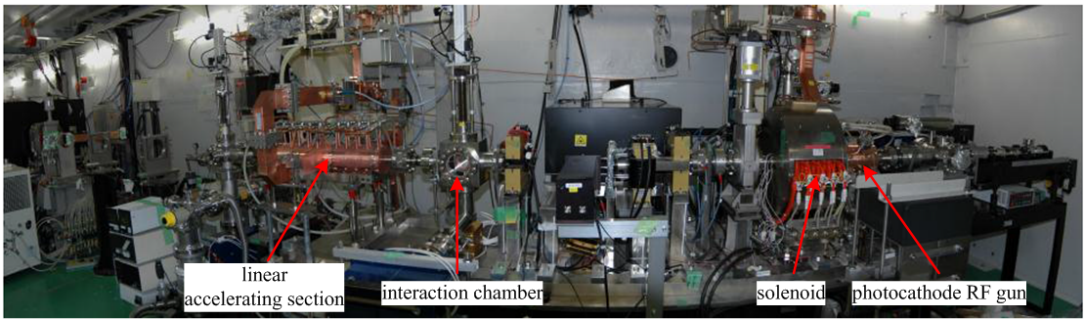


Figure 1.4: Photograph of the KEK-LUCX facility.

By imposing an intensity modulation with a periodicity in the ps or sub-ps range on the drive laser pulse, a modulated electron microbunch train can be emitted directly from the photoinjector [33, 34, 35]. One example of the implementation of the technique is the Laser Undulator Compact X-ray source facility (LUCX) at KEK, Japan (High Energy Accelerator Research Organization). A photo of the KEK-LUCX facility is shown in Figure 1.4. In the figure the main components, such as photocathode RF gun, beam focusing solenoid, interaction chamber, and linear accelerating section (not used in our experiments), are shown. It has been demonstrated that microbunches with a tunable separation (from sub-ps to few ps) can be generated with up to 4 microbunches per train [36, 35] (detailed information on

microbunch generation at the KEK-LUCX facility can be found in Chapter 4).

Modulation based on longitudinal space charge oscillation: TTX

Unlike the relative low microbunch charge (typically 30 pC) generated at KEK-LUCX, another method has been utilised by Tsinghua Thomson scattering X-ray source (TTX) in China to generate microbunched beam with higher charge (>100 pC). The first step is similar to KEK-LUCX. Illuminating the RF photocathode with a modulated drive laser pulses and this leads to the microbunching of electron beam with a small modulation depth. As the initial beam charge is large enough (>100 pC), the modulated beam undergoes evolution in the RF section due to longitudinal space charge forces. The exchange of modulation between the density and energy profiles will happen, which will further modulate the electron beam. This process was not presented at KEK-LUCX due to the low beam charge. But it has been used to control the modulation of intense beams at TTX in China [25]. A photo of the TTX facility is shown in Figure 1.5. Several ways have been used to tune the modulation depth and periodicity in the beamline: changing the initial drive laser profile, tuning the launching phase of the RF gun, tuning the compression of a downstream magnetic chicane, and adjusting the amount of charge in the beam. Microbunch trains (up to 7 microbunches) with tunable periodicities range from 0.6 and 2 ps and with a peak current of 250 A have been generated.

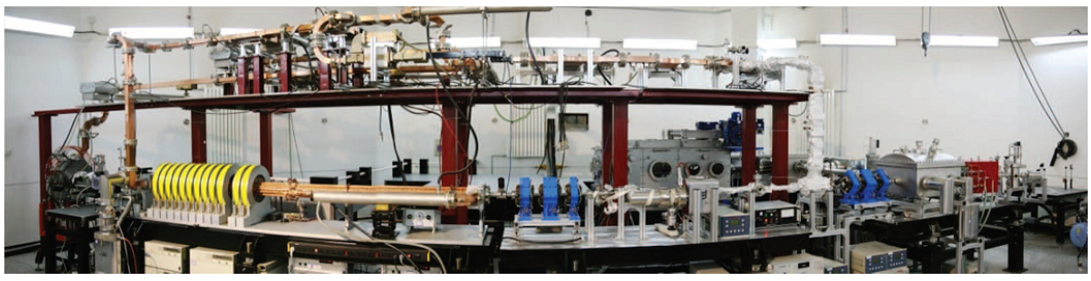


Figure 1.5: Photograph of the TTX facility [37].

Dielectric wakefield induced modulation

Wakefields are generated when a charged beam passes through a hollow dielectric structure. For a long beam, with a length comparable to or much longer than the wavelength of the fundamental mode of the wakefield, the longitudinal component of the wakefield will induce energy modulation of the long beam. Microbunch trains with sub-ps periodicity (from 1.11 ps to 1.47 ps) [24, 38] have been achieved by tuning the bunch energy chirp of the initial microbunches via magnetic optics, for example, a chicane.

Transverse to longitudinal phase space exchanging

Tunable sub-ps electron microbunch trains can also be produced using a transverse to longitudinal phase space exchange technique in combination with a multislit mask [39, 40]. The principle is as follows. At the beginning, a bunch with a correlated energy spread is produced. Defocusing the beam and letting the beam pass through a mask which is placed in a region of the beam line where the beam transverse size is dominated by this correlated energy spread. Then a group of transversely separated beamlets are generated. Afterwards, focusing the beamlets and letting them enter a dispersion-free region of the beam line. Due to the energy spread of the beamlets, the transverse modulation is converted into longitudinal modulation for applications. The number and periodicity of the electron microbunches can be controlled by tuning the beam and using masks with different profiles.

Summary

In summary, the laser based methods (direct modulation at the photocathode or modulation due to space charge effects) have been demonstrated to be efficient at bunching the electron beams. However, the introduction of a laser system along the beamline makes the accelerator system more complex and expensive. The dielectric wakefield induced modulation and the transverse to longitudinal phase space exchange methods require no additional complex components, however, the tunability is limited as it is necessary to change the dielectric

structure or the mask to alter the periodicity of the generated microbunch trains.

A promising alternative uses the interaction of an electron beam with a plasma to introduce modulation. It has been observed that by importing a long electron beam into a plasma, the beam can be divided into a train of microbunches via the self-modulation instability (SMI) [41, 42]. The periodicity of the microbunches is defined by plasma waves generated. The biggest advantage of this approach is its simplicity, as the periodicity of microbunches can be tuned by changing the plasma density. Assuming the plasma is produced via the high voltage discharge of a gas in a plasma capillary, the plasma density can be modified by changing the gas pressure. The generation of microbunch trains in a plasma and the utilization of modulated beam for THz radiation will be presented in Chapter 3.

1.4 Outline of the thesis

The main objective of the thesis is to investigate the generation of coherent THz Smith-Purcell radiation generated by microbunched electron beams. The thesis is organised as follows:

In Chapter 2, the theoretical and numerical descriptions of coherent THz Smith-Purcell radiation generated by a single electron bunch and a train of microbunches are presented.

In Chapter 3, the generation of microbunch trains in a plasma and the utilization of the modulated beam for the generation of THz radiation is investigated.

In Chapter 4, a method of monitoring the separation between microbunches is proposed and experiments carried out at the KEK-LUCX facility, demonstrating this method, are presented.

In Chapter 5, experiments carried out at the TTX facility investigating the generation of coherent THz radiation generated by a single electron bunch and a train of microbunches are discussed. The tunability of the resultant coherent THz radiation, produced using the Smith-Purcell mechanism, by changing the microbunch periodicity is demonstrated.

Chapter 2

Theoretical and numerical studies of coherent Smith-Purcell radiation

In this chapter, an analytical model to describe coherent Smith-Purcell radiation (cSPr) generated by an electron beam is presented. The analysis on the microbunching effect of a train of microbunches is discussed. Afterwards, numerical studies of cSPr using the software packages VSim and CST are carried out and the results observed are discussed.

2.1 Introduction of Smith-Purcell radiation

Smith-Purcell radiation is generated when an electron beam propagates in the vicinity of a periodic metallic grating. It was first studied by S. J. Smith and E. M. Purcell in 1953 [43]. A schematic of the radiation process is shown in Figure 2.1. A Huygens construction law was used by the authors to illustrate the dispersion relation in the far-field region:

$$\lambda = \frac{l}{n}(\frac{1}{\beta} - \cos\theta) \tag{2.1}$$

where λ is the radiation wavelength, l is the period of the grating, n is the radiation order, $\beta = v/c$ is the relativistic factor of the beam, and θ is the observation angle relative to the

beam propagation direction.

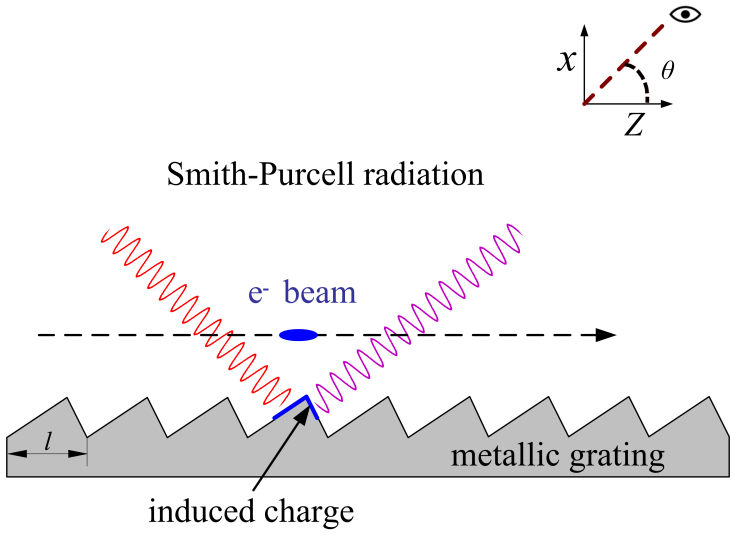


Figure 2.1: A schematic of Smith-Purcell radiation.

According to Equation 2.1, the spectrum of Smith-Purcell radiation is monochromatic and contains a series of harmonics (order $n > 1$) at a fixed observation angle. The radiation in space covers a wide range of frequencies with short wavelengths radiate in the forward direction and the long wavelengths radiate in the backward direction. The shortest and longest wavelengths should be observed at the observation angle of $\theta = 0°$ and $180°$, respectively. In the case of infinitely short relativistic beam $\beta \approx 1$, the radiation wavelengths range from 0 to $2l$. However, in practise the radiation efficiency becomes very low before the observation angle θ reaches $0°$ due to the limitation of the finite small size of the beam.

By selecting the grating period in the range of millimetre (mm) or sub-mm, THz radiation can be observed. Unlike other methods of generating radiation using high energy electron beams, such as transition mechanism, the Smith-Purcell radiation mechanism causes no beam loss or material destruction. Therefore, there has been an increasing interest in the THz Smith-Purcell radiation.

There are a number of different theoretical models to describe Smith-Purcell radiation mechanism. The first approach is based on the description of the electric field of the moving beam by a set of evanescent waves and the radiation is due to the diffraction of the evanescent waves on the surface of a grating. This model was proposed by Toraldo di Francia in 1960

[44]. From this, van den Berg developed a model to analyse the radiation generated by an infinitely long grating [45, 46], which was further developed by Haeberlé later [47]. The model was subsequently evolved into the Electric Field Integral Model (EFIE) by Kesar et al. [48]. Van den Berg's model provides a rigorous analysis of the EM boundary-value problem at the grating surface, which means it is applicable to a grating with an arbitrary profile. The corresponding problem is that it demands large and difficult numerical calculations, especially when wavelengths are much shorter than the period of grating.

Another model was suggested by Smith and Purcell that a surface charge is induced when an electron passes over a grating and radiation is generated when the induced current is passing the grooves in the grating [43]. The analytical description of the surface current model was developed by Brownell and Doucas et al. [49, 50, 51]. Surface current model is easy to understand in physics and the calculation is much faster than van den Berg's model, it is suitable for shallow gratings where the influence of resonant cavity modes is neglected. The predictions of the surface current model have been confirmed by experiments at SLAC with multi-GeV beams, which are the highest energy Smith-Purcell radiation experiments to date [30].

There are some other models providing alternative explanations of Smith-Purcell radiation, such as the resonant diffraction radiation model considered by Potylitsyn [52, 28] and the polarization current model considered by Karlovets [53]. Resonant diffraction radiation model is suitable for calculating the radiation characteristics for a grating consisting of a number of conducting strips spaced by vacuum gaps. Polarization current model assumes the radiation is generated by the polarization current induced in a medium by the field of a moving charge. This model is more general and complex. It could be used to calculate the radiation induced both from dielectrics and conductors. In the case of medium being conductor, polarization current model coincides with surface current model.

In the thesis, I mainly consider the radiation from metallic gratings. Considering the complexity and applicability of these models, surface current model has been used for theoretical analysis in the following.

2.2 Analytical description

2.2.1 Radiation generated by an electron bunch

Considering a spherical coordinate system shown in Figure 2.2, where $\vec{k}$ is the wave vector of the emission, ϕ is the azimuthal angle of emission, θ is the angle relative to the beam axis, and the grating is a perfect conductor with an infinite width. The energy of Smith-Purcell radiation emitted by a single electron per unit solid angle is given in Reference [50], as:

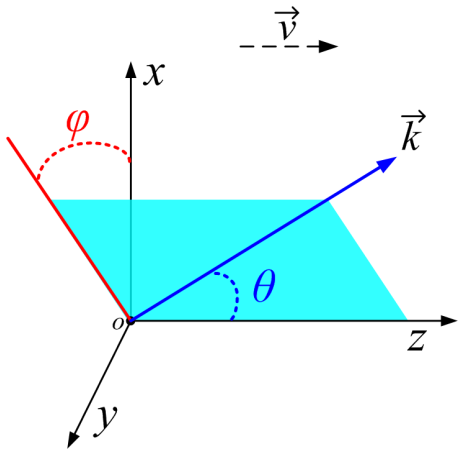


Figure 2.2: A schematic of the coordinates used in the surface current model.

$$\left(\frac{dI}{d\Omega}\right)_1 = 2\pi e^2 \frac{L}{l^2} \frac{n^2\beta^3}{(1-\beta\cos\theta)^3} R^2 \exp(-2x_0/\lambda_e) \tag{2.2}$$

where e is the unit charge, L is the total length of the grating, l is the period of the grating, n is the radiation harmonic number, the relativistic factors $\beta = v/c$ and $\gamma = (1-\beta^2)^{-1/2}$, R^2 is a parameter defining the dependence of radiation energy on the profile of grating (details are given in Reference [49]), x_0 is the position of the beam above the grating surface, and λ_e is the "evanescent wavelength" defined by:

$$\lambda_e = \frac{\lambda}{2\pi} \frac{\beta\gamma}{\sqrt{1+\beta^2\gamma^2\sin^2\theta\sin^2\phi}} \tag{2.3}$$

where λ is the observation wavelength. As shown in Equation 2.2, the effective coupling

between electron beam and grating is described by $\exp(-2x_0/\lambda_e)$ and the radiation decreases exponentially as the beam-grating separation increases.

The above analysis is applicable to a single electron passing above a grating. For a distribution of N electrons moving along z axis, the energy radiated per unit solid angle is given by [50]:

$$\left(\frac{dI}{d\Omega}\right)_N = \left(\frac{dI}{d\Omega}\right)_1 [NS_{inc} + N(N-1)S_{coh}] \tag{2.4}$$

Assuming the charge distribution of the electrons in the bunch is uncorrelated, $\rho(x, y, t = z/v) = X(x)Y(y)T(t)$, the incoherent integral S_{inc} can be written as:

$$S_{inc} = \int_0^{+\infty} X(x) \exp[-2(x - x_0)/\lambda_e] dx \tag{2.5}$$

while the coherent integral S_{coh} is given by:

$$\begin{aligned} S_{coh} = & \left| \int_0^{+\infty} X(x) \exp[-(x - x_0)/\lambda_e] dx \right|^2 \times \left| \int_{-\infty}^{+\infty} Y(y) \exp(-jk_y y) dy \right|^2 \\ & \times \left| \int_{-\infty}^{+\infty} T(t) \exp(-j2\pi\nu t) dt \right|^2 \end{aligned} \tag{2.6}$$

Normally the transverse dimension of the bunch can be focused to be much smaller than the observation wavelength and the influence of the transverse profile can be neglected. In this case:

$$\left(\frac{dI}{d\Omega}\right)_N \approx \left(\frac{dI}{d\Omega}\right)_1 [N + N(N-1)|F(\nu)|^2] \tag{2.7}$$

where $F(\nu) = \int_{-\infty}^{+\infty} T(t) \exp(-j2\pi\nu t) dt$ is the longitudinal bunch form factor. It can be seen from Equation 2.7 that the first term in the square brackets describes the incoherent radiation and is proportional to N, while the second term represents the coherent radiation, proportional to N^2. Typical value for N is around $10^8 - 10^9$. The coherent radiation is

much higher than the incoherent one when the bunch length is smaller than the operating wavelength, in which case $|F(\nu)|^2$ is of order unity.

In other words, when the transverse and longitudinal dimensions of a bunch are both much smaller than the operating wavelength, the time delay differences for the radiation signals from particles to arrive at the observation point can be neglected. The phase of radiation due to individual particles in the bunch is the same and the radiation is fully coherent.

2.2.2 Effect of beam microbunching

The effect of beam microbunching on the bandwidth and intensity of Smith-Purcell radiation is studied in the following. In the case of a train of microbunches, i.e. an electron beam consisting of M identical microbunches equally separated by an interval Δt with a repetitive longitudinal temporal profile $T(t - n\Delta t), n = 0, 1..., M - 1$, the form factor $|F(\nu)|$ is given by:

$$\begin{aligned} |F(\nu)|^2 &= |F_1(\nu)|^2 G_M(\nu, \Delta t) \\ G_M(\nu, \Delta t) &= \frac{1}{M^2} \frac{\sin^2(M\pi\nu\Delta t)}{\sin^2(\pi\nu\Delta t)} \end{aligned} \tag{2.8}$$

where $|F_1(\nu)|$ is the form factor of a single microbunch and $G_M(\nu, \Delta t)$ is a modulation function depending on the observation frequency and the microbunch spacing. For example, $|F_1(\nu)|^2$ becomes $\exp[-(2\pi\nu\sigma)^2]$ for a single Gaussian microbunch with rms longitudinal length σ (in the unit of time).

For a grating with N periodic facets, the factor defining the Smith-Purcell radiation from the grating is given by [54]:

$$G_{facet}(\nu) = \frac{\sin^2(N\pi\nu\phi)}{\sin^2(\pi\nu\phi)} \tag{2.9}$$

where N is the number of periodic facets, $\phi = l/c(\beta^{-1} - \cos\theta)$, β is the relativistic factor of the beam, and θ is the observation angle. When $N \gg 1$, the factor G_{facet} gives the dispersion relation shown in Equation 2.1 and the value of the factor becomes N^2.

Considering a train of 8 microbunches ($M = 8$) with a single microbunch length σ of 0.1 ps and microbunch periodicity Δt of 1 ps, the number of periodic facets N in the grating is 25, the parameter ϕ in Equation 2.9 to be 1 ps (the corresponding frequency is 1 THz), the influence of beam microbunching on the bandwidth of Smith-Purcell radiation is shown in Figure 2.3. It can be seen that there is no obvious difference in bandwidth after considering the effect of microbunching. In the thesis, it is considered that the number of periodic facets N (> 20) is much larger than the number of microbunches M (less than 10). In this case, the effect of beam microbunching on the bandwidth of Smith-Purcell radiation can be neglected. Therefore the bandwidth of radiation at observation frequency ν is defined by ν/N.

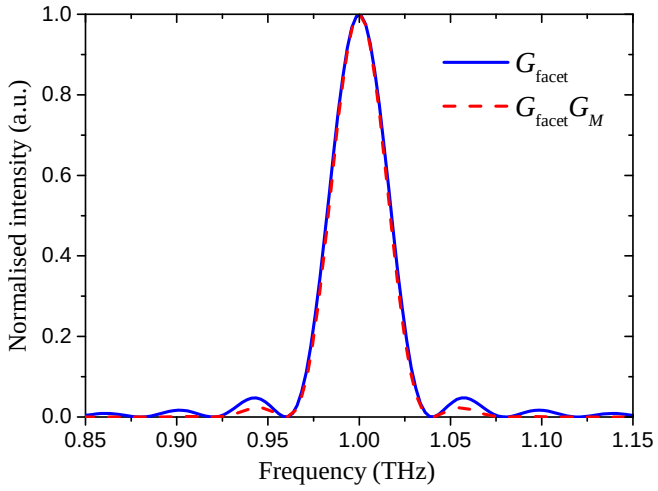


Figure 2.3: Comparison of the bandwidth of Smith-Purcell radiation (observed at 1 THz) considering (dashed line) and without considering the microbunching effect (solid line).

The effect of microbunching on the intensity distribution of Smith-Purcell radiation in space is considered in the following. First a single Gaussian bunch is considered. The square of form factor $|F(\nu)|^2$ for a single Gaussian bunch with longitudinal lengths σ of 0.1 ps, 0.3 ps, and 0.5 ps is shown in Figure 2.4. It shows that form factor decays exponentially as the frequency increases and that the smaller bunch length the larger the form factor (maximum

is 1). The bunch length should be of the order of 0.3 ps or smaller if one wants to achieve significant radiation above 1 THz.

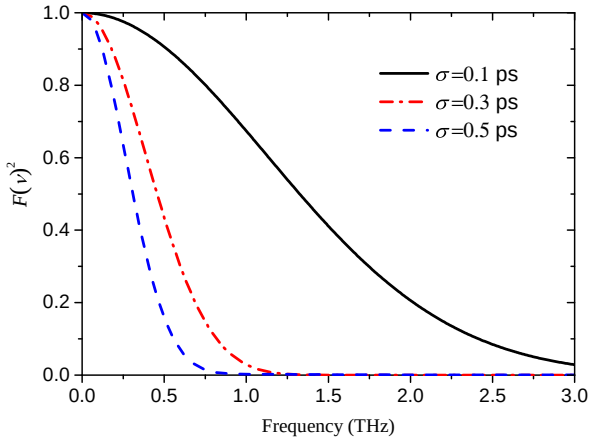


Figure 2.4: The square of form factor $|F(\nu)|^2$ as a function of frequency for a single Gaussian bunch with longitudinal lengths σ of 0.1 ps, 0.3 ps, and 0.5 ps.

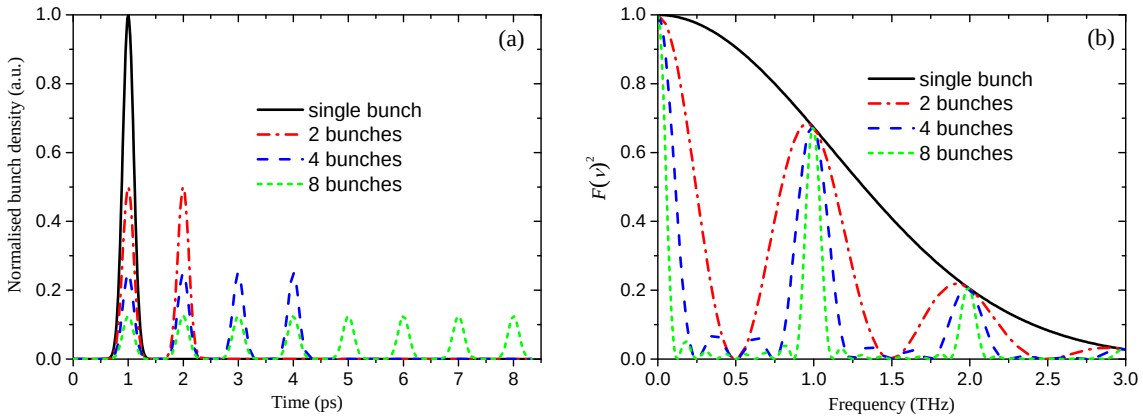


Figure 2.5: Normalised density distributions of a train of microbunches (in same total charge) with microbunch separation of 1 ps (a) and the corresponding form factors (b). The length σ of each single Gaussian microbunch is 0.1 ps.

Next a train of microbunches is considered. As shown in Equation 2.8, the form factor $|F(\nu)|$ depends on the observation frequency and the microbunch periodicity. For the same single microbunch length of 0.1 ps, the form factors for a single bunch and a train of microbunches with the same total charge are shown in Figure 2.5. For microbunch trains, the charge is distributed evenly into the equally spaced identical microbunches with periodicity

Δt of 1 ps. Unlike the broad spectrum of a single bunch, the form factor of a microbunch train has peaks at the microbunch frequency ν_b (1 THz) with the high harmonics located at $n\nu_b$. As the radiation intensity is proportional to $|F(\nu)|^2$ (shown in Equation 2.7), meaning the more microbunches, the more radiation intensity concentrating at around the microbunch frequency and its harmonics.

2.3 Numerical studies of cSPr in the near-field region in VSim

2.3.1 Introduction of PIC simulation VSim

The particle-in-cell (PIC) method is one of the techniques to solve electromagnetic partial differential equations. The key point of the PIC method is the calculation of the self-consistent fields of particles taking into account particle dynamics. Here 'particle' means an individual particle or a macroparticle consisting of many real particles. The space where the analysis takes place is divided into cells (grids). As shown in Figure 2.6, a full computational cycle of the PIC simulation starts with the initialization of the electric and the magnetic fields, and the positions and velocities of particles. Particles are accelerated under the Lorentz force and the new velocities and positions of the particles can be obtained using Newton's second law of motion. Subsequently the current deposited on the grids can be updated. Based on the new current and the known fields, new fields can be computed which will be used next to push the particles moving further until the end of desired simulation duration. Therefore, PIC method is self-consistent during the calculation.

VSim (also called Vorpal) is a flexible, cross-platform computational software tool for running computationally intensive electromagnetic and plasma simulations [55]. The simulation can be in one, two, or three dimensions, which makes it suitable for both desktop and computing clusters. Simulations in three dimensions are normally computationally intensive and require clusters with more than hundreds of cores. Due to the lack of sufficient memory

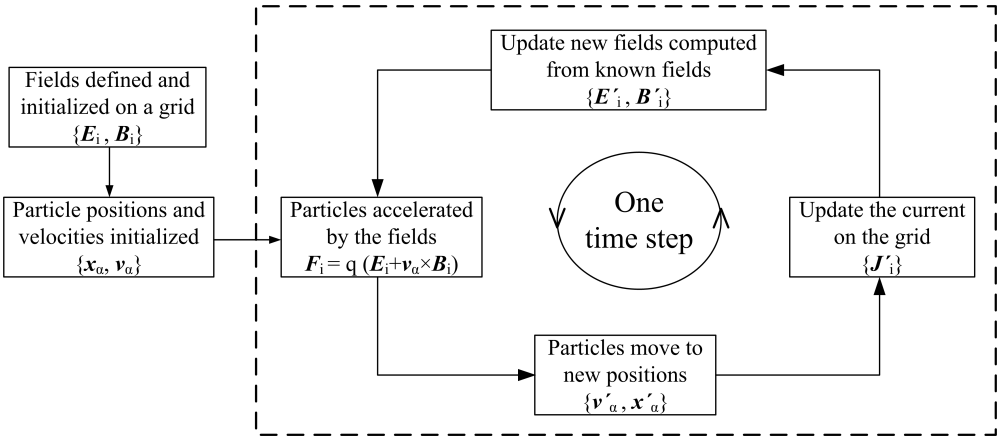


Figure 2.6: One computational cycle of the PIC simulation.

and cores, far-field simulations are impossible as large simulation dimensions increase the computing load significantly. Therefore, all the VSim simulations in this thesis were performed in two dimensions (2D) by neglecting the spatial variation in the third dimension. This is also called '2.5D simulation', as time evolution is taken into account in the simulation.

As I mainly deal with simulation problems with open boundaries, a module in VSim called perfectly matched layer (PML) was used in the simulations. The PML is an artificial absorbing layer which is designed to absorb the incident waves without reflection at the interference. There are some limitations of such an approach as the PML operates over a finite range of frequencies. The broad frequency range (up to several THz) in our simulations means that part of the waves incident on the PML will be reflected. For particles, an absorbing box is used to absorb the particles incident upon the surface of the box.

2.3.2 Simulation setup

The schematic of the model in VSim is shown in Figure 2.7 with the grating located below the beam. The boundaries of the box were formed by the PML to absorb the emitted EM waves. The beam and grating parameters are shown in Table 2.1. The beam profiles were assumed to be Gaussian both in the longitudinal and the transverse directions.

To generate Smith-Purcell radiation, the beam passed above the grating and the distance between beam centre and the grating was 0.5 mm. The field monitor, which was used to

record the magnetic field in the y direction B_y in the near-field region, was positioned 10 mm above the grating centre and at 90 degrees to its surface.

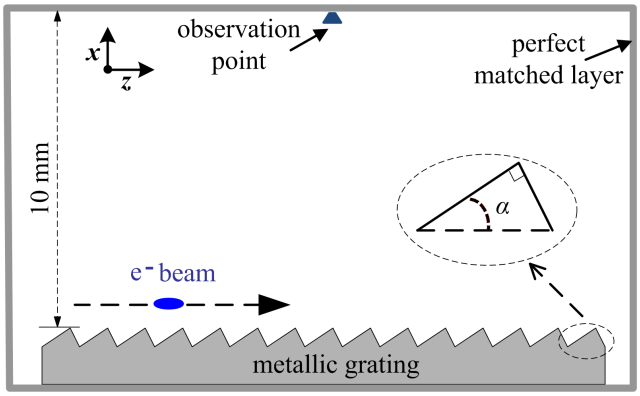


Figure 2.7: Schematic diagram of the VSim simulation showing THz radiation generation.

Table 2.1: Beam and grating parameters

Description	Parameters	Value
Beam energy	E	50 MeV
Beam charge	Q	1 nC
Beam longitudinal size	σ_l	50 μm
Beam transverse size	σ_t	30 μm
Grating period	l	500 μm
Facet number	N_f	25
Facet angle	α	30°
Beam grating distance	d	500 μm

Since the transverse dimensions of beam and beam-grating separation are both much smaller than the transverse dimension of grating (normally tens of mm), 2D approximation for numerical model is reasonable (grating in y direction is considered to be infinite). The dimensions of simulation box are 23 mm (longitudinal direction) by 12 mm (transverse direction) and it is divided into 2758 by 2058 cells, respectively. Numerical studies are carried out to investigate the radiation characteristics of both a single bunch and microbunch trains.

2.3.3 Radiation generated by a single bunch

The beam moves along z direction above the grating. In order to demonstrate the evolution of the Smith-Purcell radiation pattern, the snapshots of the magnetic field B_y in y direction

(perpendicular to the simulation plane) at different times are shown in Figure 2.8. The effect of the beam self-fields and of the diffraction radiation from the edge of the grating can be accounted for by subtracting from the signal observed from a blank target, i.e. an identical piece of metal but with no corrugations on the surface. In this case the signal which contributes to the low frequency part of the radiation spectrum has been removed by subtracting the signal radiated from periodic grating to that of from blank target.

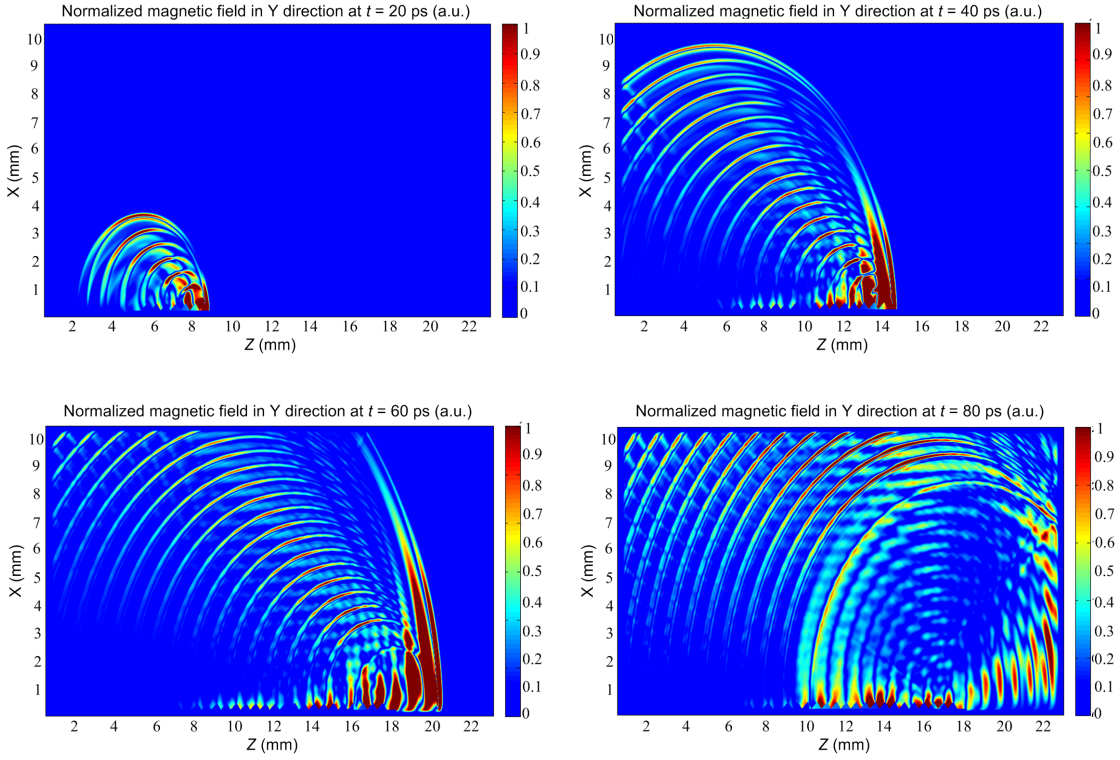


Figure 2.8: Snapshots of the distribution of magnetic field B_y at simulation time $t = 20$ ps, 40 ps, 60 ps, and 80 ps.

As discussed earlier, each time the beam passes above a facet, the discontinuity of the facet disturbs the propagation of the induced current and generates radiation propagating into space. In Figure 2.8, at $t = 20$ ps, the beam was on the top of the 7^{th} sawtooth, there were 6 wavefronts propagating into free space. At $t = 40$ ps, the beam was passing the 19^{th} sawtooth, there were 18 wavefronts propagating into space. The radiation waves from an array of facets will interfere with each other in the far-field region, forming the dispersion relation defined by Equation 2.1.

Without loss of generality, the radiation signal observed at 90 degrees has been chosen

for analysis and it is expected to be representative of the total radiation spectrum. The amplitude of the signal and its Fourier transform in the near-field are shown in Figures 2.9 and 2.10 (solid black line). The predictions (red dashed line) were calculated using $F(\nu) = \exp[-2(\pi\nu\sigma_l)^2]$ for a Gaussian bunch. It can be seen that, there is an exponential decay of the amplitude of the spectrum from 0.5 THz to 3 THz and the predictions show similar pattern. The drop of the radiation intensity at the "cut-off" frequency for Smith-Purcell radiation (0.3 THz, angle $\theta = 180°$) is evident.

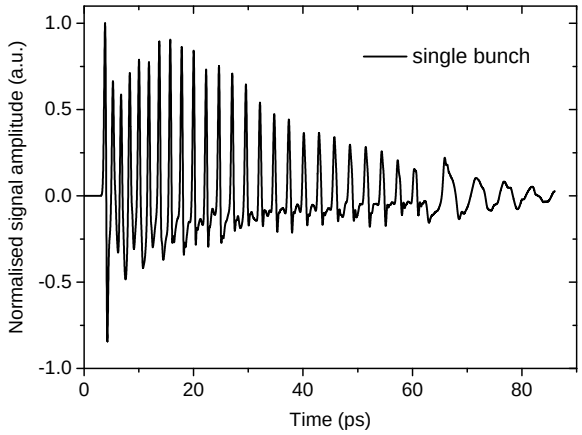


Figure 2.9: Normalised transient waveform of B_y observed at 90 degrees.

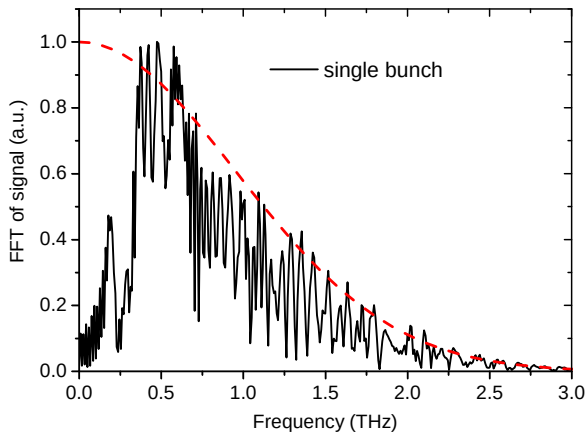


Figure 2.10: Comparison of the form factor obtained from theoretical predictions (dashed line) and the FFT of the signal shown in Figure 2.9 (solid line).

Traditionally, cSPr is investigated in the far-field region, which means that the dispersion

relation which relates the radiated frequency to the emission angle is always fulfilled. In Figures 2.9 and 2.10, however, there was no monochromatic radiation at a frequency 0.6 THz (grating period of 0.5 mm at the observation angle of 90 degrees). In this case the monitor collected the generated with the whole spectrum. Without the monochromatic interference effects, the dispersion relation is not satisfied.

2.3.4 Radiation generated by microbunch trains

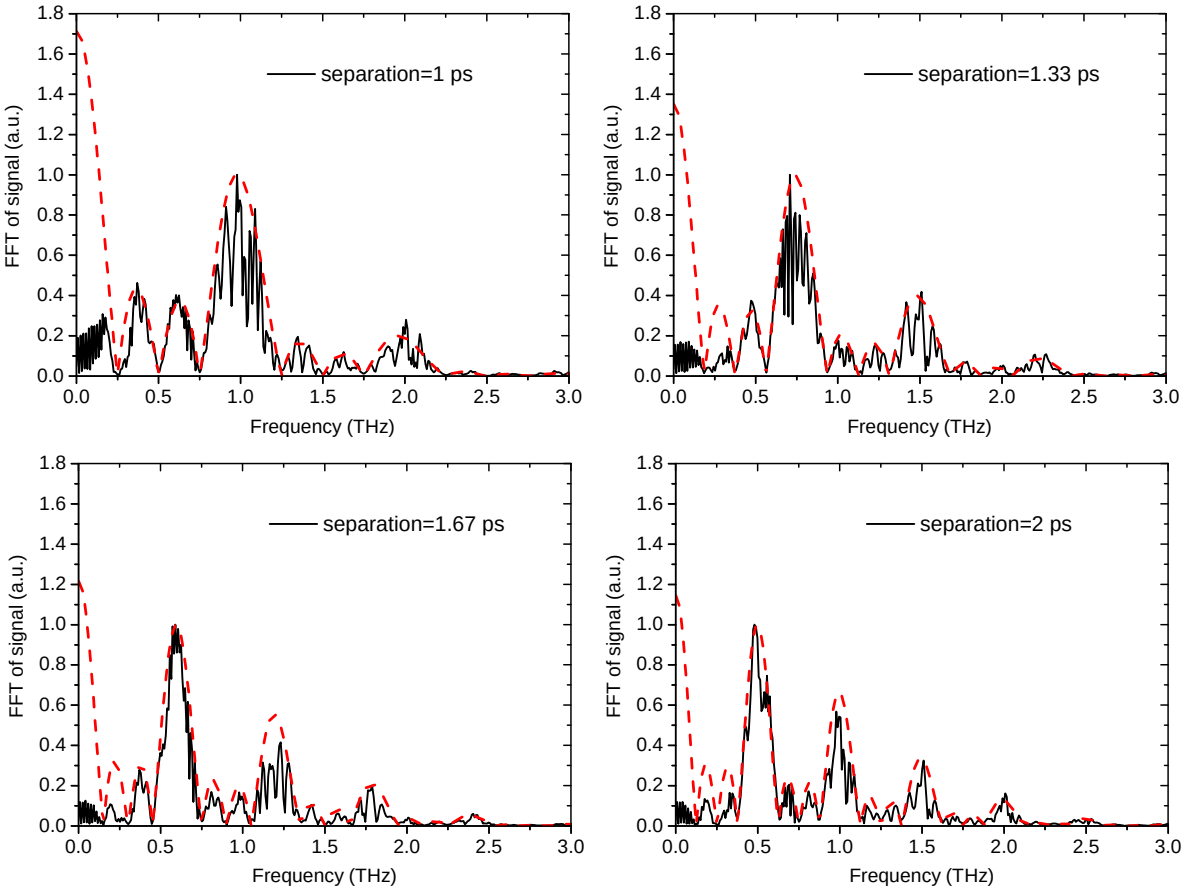


Figure 2.11: Comparison of the form factor obtained from theoretical predictions (dashed lines) and the FFT of the signal from the VSim simulation (solid lines) for a train consisting 4 identical microbunches with separations of 1 ps, 1.33 ps, 1.67 ps, and 2 ps.

Using the same beam parameters and splitting the total charge into 4 identical microbunches, the simulations were repeated for the case of microbunch trains. The Fourier

transforms of the signals observed at the angle of 90 degrees for microbunch trains with separations of 1 ps, 1.33 ps, 1.67 ps, and 2 ps are shown in Figure 2.11. The FFT of signals from VSim simulations (solid black lines) are normalised with the maxima being 1. The bunch form factor is also normalised into 1 at the corresponding microbunch frequency for a clear comparison. As the microbunch spacing changes the spectral peaks of the radiation are located at 1 THz, 0.75 THz, 0.6 THz and 0.5 THz, as expected. The existence of microbunch trains ensures that the radiation spectrum in the near-field region corresponds to the spectrum of microbunch trains. The disappearance of the low frequency components from VSim simulations is mainly due to the fact that signals have been adjusted by the signals observed from a blank target.

By increasing the microbunch separation while keeping the size of every single microbunch constant, more harmonics appear. For example, in the case of microbunch trains with separation of 2 ps, apart from the main peak at 0.5 THz, higher harmonics at 1 THz, 1.5 THz, and 2 THz become clear.

Due to the limitation of computing resources, the simulations in VSim are performed in the near-field region. However in practise the observation and collection of Smith-Purcell radiation are normally carried out at the distance much larger than the dimension of the periodic grating. In order to obtain the radiation properties in the far-field region, PIC simulations have also been carried out using the fully relativistic, self-consistent particle-in-cell solver module (including full space-charge effects) in CST Particle Studio in the next section.

2.4 Numerical studies of cSPr in the far-field region in CST

2.4.1 Introduction of PIC simulation CST

CST Particle Studio is a new package of CST Studio Suite. Simulations of particles and electromagnetic fields in three dimensions can be performed fully consistently using the time domain PIC solver. The PIC solver is embedded in the code and it can be chosen when one selects the workflow of simulation. Unlike VSim, open boundary condition was used instead of PML in the CST simulation. The biggest advantage of the PIC solver in CST Particle Studio over VSim is that the far-field radiation can be recorded by far-field probes, which enables looking at the radiation properties in far-field and comparing with analytical results.

Due to the limitations of computing resources, it is almost impossible to launch PIC simulation in CST to cover the entire calculation domain, especially when it involves with simulations in the far-filed region. The solution is to extrapolate the calculated scattered fields in the near-field region to the far-field region in the time domain at the simulation border [56]. In this case, far-field probes can be used to record the far-field radiation distribution, even when the simulation is performed in the near-field region. Field components, either in Cartesian or spherical coordinate system, can be recorded individually using far-field probes.

2.4.2 Simulation setup

PIC simulations in CST were performed to investigate cSPr in the far-field region. The schematic of the simulation is shown in Figure 2.12. The same beam and grating parameters shown in Table 2.1 were used. In the spherical coordinate system shown in Figure 2.12, $\vec{k}$ is the wave vector of the emission, ϕ is the azimuthal angle of emission, and θ is the angle relative to the beam axis.

In the 3D model, the grating has a finite width of 10 mm. The far-field monitors, which

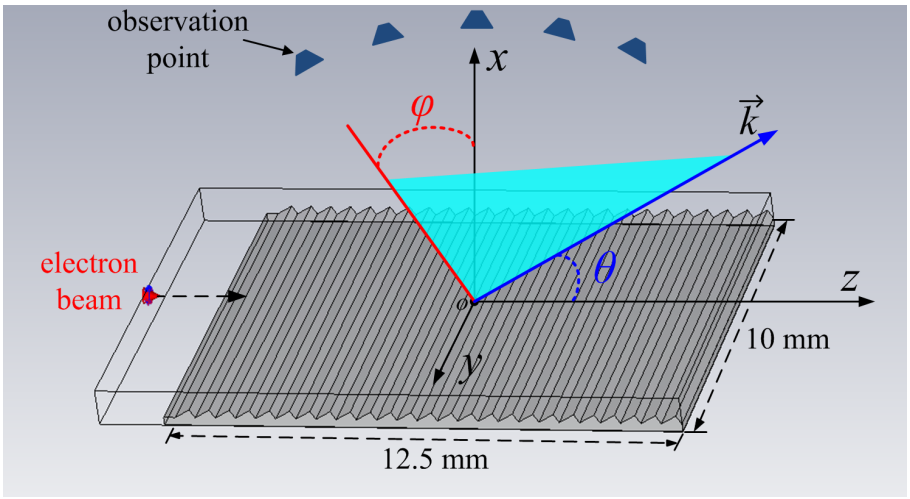


Figure 2.12: A schematic of the CST simulation showing THz radiation generation.

were used to record the magnetic fields in the far-field region, were positioned 1 m away from the centre of the grating (origin 'o') at a number of θ angles from 60° to 150° with an interval of 1° (91 points). All the monitors were in the plane ϕ=0.

Adaptive meshing was used in the model, meaning the mesh size was relatively small at the region where fine structure appears. In this model, the smallest mesh size was 1.7 μm (in x direction) and the largest mesh size was 15 μm (in y direction), which were both much smaller than the radiation wavelengths of interest (from 150 μm to 600 μm).

2.4.3 cSPr from a single bunch

I start with the simulation for a beam consisting of a single electron bunch with the parameters shown in Table 2.1. A typical signal observed at an angle θ of 80° (observation plane at $\phi = 0$) and its corresponding Fourier transform are shown in Figure 2.13.

The signal shown in Figure 2.13(a) includes 4 parts: part 1 is caused by the self-field of the beam, part 2 is the diffraction signal from the edge of the grating, part 3 is the real Smith-Purcell radiation, and part 4 is due to the reflection at the boundaries (not a perfect open structure in the calculation). In Figure 2.13(b), the three peaks noted by 3 are contributed by Smith-Purcell radiation. The central frequency of the first harmonic and the

second harmonic is 0.73 THz and 1.457 THz, which agrees with the frequencies (0.726 THz and 1.452 THz) obtained from dispersion relation in Equation 2.1.

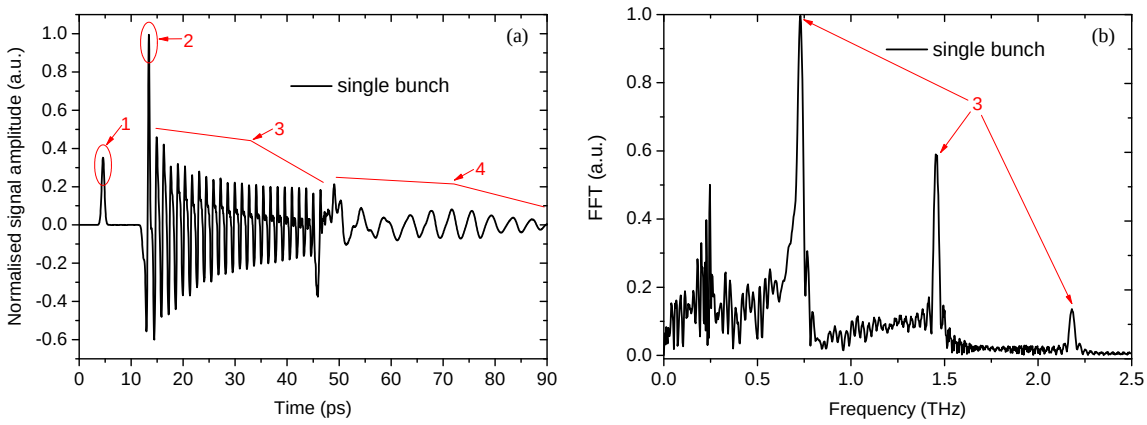


Figure 2.13: Normalised transient waveform of field $B_\phi(t)$ observed at an angle θ of 80° (a) and the corresponding FFT $B_\phi(\nu)$ (b).

In the following, a comparison of the radiation spectral bandwidth from theory and from numerical simulation has been carried out to verify whether the simulations are in the far-field region. The bandwidth of the first harmonic of Smith-Purcell radiation in Figure 2.13(b) is calculated to be 0.028 THz. According to theoretical analysis in Reference [57], in the far-field region, the bandwidth $\Delta\nu$ of Smith-Purcell radiation at a given observation frequency ν for a grating with N periods is given by $\Delta\nu = \nu/N$. The number of periods $N = 25$ in the simulation. The theoretical bandwidth is given by $0.726/25 = 0.029$ THz, which is consistent with the result from simulation. Therefore the bandwidth comparison confirms that simulations are performed in the far-field region.

In order to remove the influence of the beam self-fields and the diffraction radiation at the edge of the grating (part 1 and part 2 in Figure 2.13(a)), the radiation signal were obtained by subtracting the blank signal from the grating signal.

At the observation plane ($\phi = 0$), we have the relation that $\boldsymbol{B} = \boldsymbol{n} \times \boldsymbol{E}/c$, where $\boldsymbol{B} = B_\phi \hat{\boldsymbol{e}}_\phi$ ($B_r = B_\theta = 0$) and $\boldsymbol{E} = E_\theta \hat{\boldsymbol{e}}_\theta$ ($E_r = E_\phi = 0$). By applying Fourier transforms to the electric signals observed at all the 91 angles and using Equation A.3 in Appendix A, the radiation spectrum at the observation plane $\phi = 0$ was obtained and is shown in Figure 2.14.

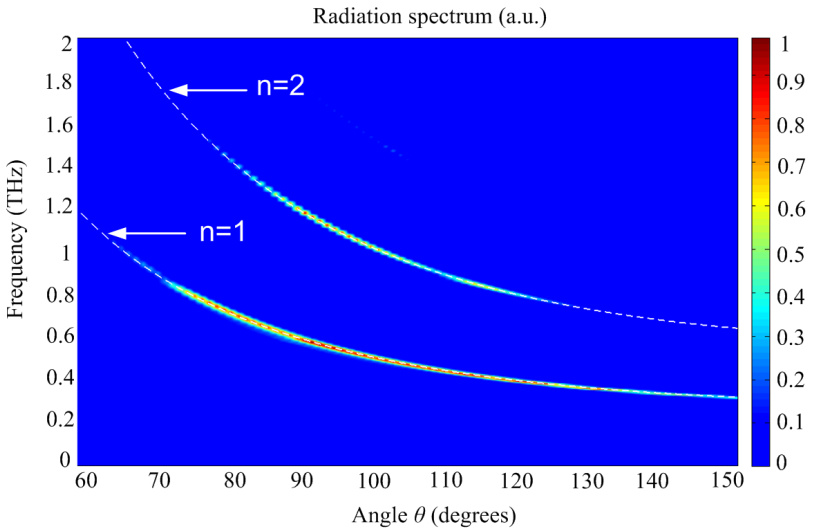


Figure 2.14: Normalised spectrum of the radiation generated by a single bunch as a function of the observation angle θ and the emission frequency (observation distance=1 m, azimuthal angle ϕ=0°).

As the radiation spectrum at the frequency of interest has a finite bandwidth (as shown in Figure 2.13(b)), all the radiation within the bandwidth has been counted as the radiation at that frequency.

The dashed lines are plotted based on the dispersion relation in Equation 2.1. It is clear that the Smith-Purcell radiation spectrum fits excellently well with the dispersion relation in the far-field region. For the first harmonic ($n = 1$), the radiation intensity vanishes for frequency up to around 1 THz. Most of the radiation is concentrated in the range from 0.8 THz to 1.5 THz for the second harmonic ($n = 2$).

2.4.4 cSPr from a train of microbunches

Considering the same beam parameters used for a single bunch while splitting the total charge into 4 equidistant short microbunches, simulations have been performed in CST. Based on the same method, the spectra of Smith-Purcell radiation generated by microbunch trains with separations of 1 ps, 1.33 ps, 1.67 ps, and 2 ps are shown in Figure 2.15.

It can be seen from Figures 2.15(a) - (d) that the dispersion relation of cSPr still fits well in the far-field region. Unlike the broad continuous distribution generated by a single bunch, the

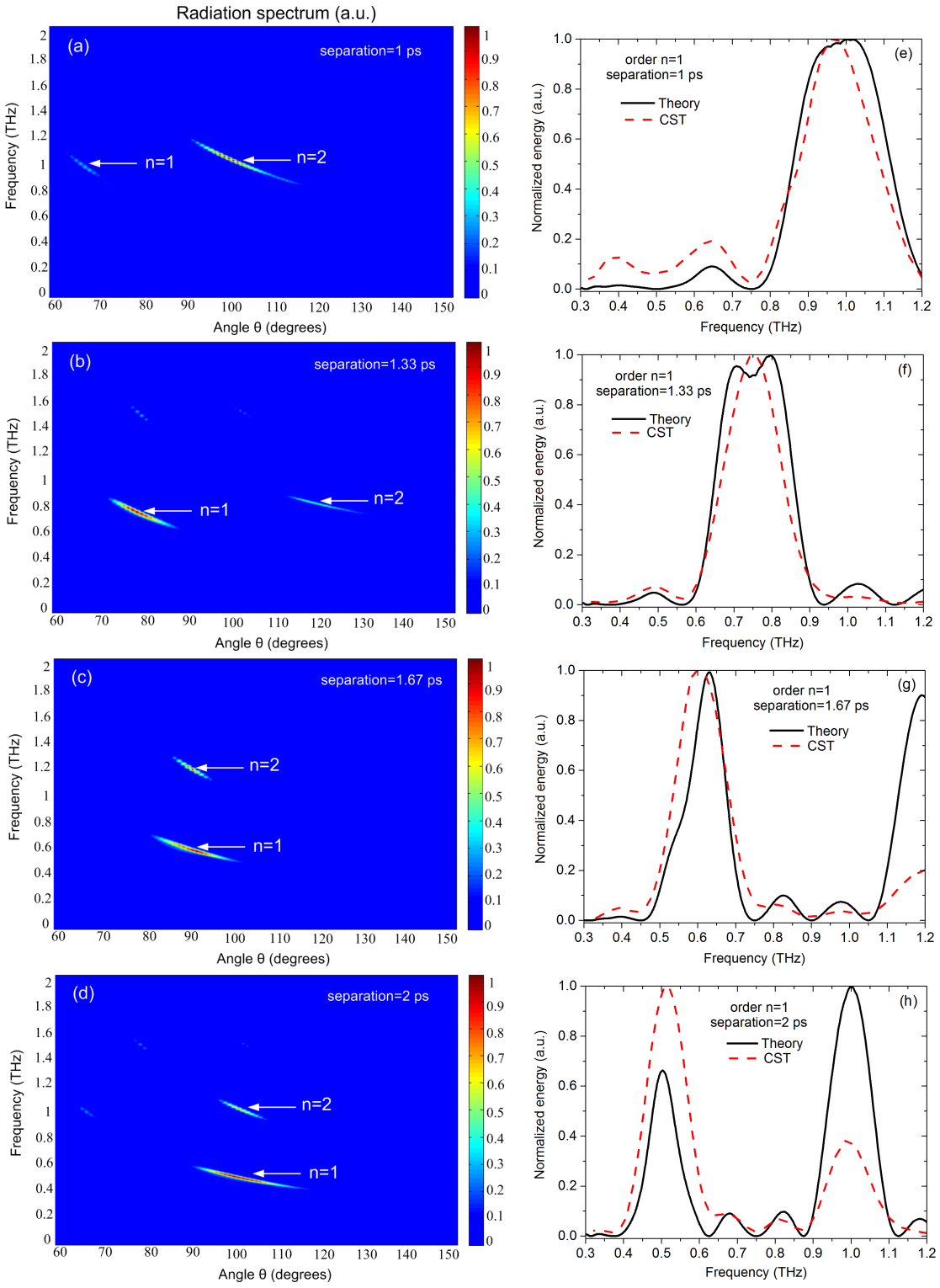


Figure 2.15: Comparison of radiation obtained from the CST simulation and theoretical calculation using a train consisting of 4 identical microbunches with separations of 1 ps, 1.33 ps, 1.67 ps, and 2 ps.

radiation generated by microbunched beams is concentrated at around certain frequencies, which correspond to the microbunch frequency ($n = 1$) and its harmonics ($n = 2$ in this case). As the microbunch separations are chosen to be 1 ps, 1.33 ps, 1.67 ps, and 2 ps, the spectral peaks at 1 THz, 0.75 THz, 0.6 THz, and 0.5 THz are as expected ($n = 1$). There is a clear correlation between the microbunch separation and the radiation concentration in the far-field region. One interesting thing in Figure 2.15(a) is that the radiation is concentrated at the frequency of 1 THz. The radiation at the second harmonic of 0.5 THz ($\theta \approx 102°$, $n = 2$) is much more intense than that of the first order of 1 THz ($\theta \approx 66°$, $n = 1$), which is not seen for other microbunch separations.

By applying the theoretical analysis in Section 2.2 to cSPr, a semi-analytical code named GFW (Grating of Finite Width) was written by Dr G. Doucas [51]. Based on the parameters given in Table 2.1 and the finite grating width of 10 mm, the radiation distribution in space at order $n = 1$ has been calculated using the GFW code.

The comparison of the results from the CST simulation and calculation from the GFW code is shown in Figures 2.15(e) - (h). For all four microbunch separations, both theoretical calculation and the CST simulation predict the peaks of radiation at microbunch frequencies. The agreement is good for microbunch separations of 1 ps and 1.33 ps. While the theoretical calculation for the other two separations predicts a higher radiation energy at the second harmonic than that from the CST simulation. For example, at microbunch separation of 2 ps, both the CST simulation and theoretical calculation show the spectral peaks at 0.5 THz and 1 THz. The CST simulation indicates that radiation energy at 1 THz ($\theta \approx 66°$, $n = 1$) is lower than that of at 0.5 THz ($\theta \approx 102°$, $n = 1$), while the theoretical prediction shows that radiation at 1 THz is slightly higher than that of at 0.5 THz.

As mentioned earlier, the far-field radiation in the CST simulation was obtained by extrapolating the scattered fields in the near-field region at the simulation border, while the scattered fields may not always become propagating waves in the far-field region. The GFW calculation was based on the surface current model where all the EM fields are considered in the far-field region. This may explain the difference between theory and simulation.

2.5 Summary

In this chapter, the effect of the microbunching of electron bunches on the intensity of the cSPr emitted was studied analytically and numerically. The analytical study was carried out by analysing the bunch form factor of the beam. The numerical study was performed by observing the intensity of the radiation generated by electron bunches both in the near-field and the far-field regions, which was carried out using the PIC simulation VSim and CST, respectively. It was found that the microbunching of the electron bunches results in the intensity of the generated cSPr concentrating at the microbunch frequency and its harmonics. Numerical results were compared with theoretical calculations and there is a good agreement between them. This demonstrates the potential tunability of radiation by the variation of the microbunch separation.

Chapter 3

The generation of a train of microbunches in a plasma

In this chapter, I discuss the steps required to observe tunable THz radiation generated by a picosecond-long relativistic electron beam modulated by a plasma channel. I start with the basic principle of the beam modulation in the plasma channel, demonstrating an efficient modulation in the transverse plane and formulating the challenges associated with the utilization of such a modulated beam. In Section 3.1 the influence of different parameters on the beam modulation is investigated analytically. In Section 3.2 the beam-plasma interaction is investigated numerically using the PIC code VSim and the results observed are compared with the theoretical analysis. The beam collimation procedure required to observe efficient longitudinal modulation from originally modulated beam and the propagation of the collimated beam in vacuum drift area are discussed in Section 3.3. In Section 3.4 the generation of coherent THz radiation by the interaction of a train of microbunches with a periodic metal grating is discussed.

3.1 Basic principle and analytical model

3.1.1 Basic principle

A plasma consists of a collection of positive and negative charged particles (for example ions and electrons, respectively) and normally it is electrically neutral in equilibrium. When a strong electromagnetic field is applied (via external laser pulses or charged relativistic particles propagating in a plasma), the plasma electrons are pushed away from the centre while the background ions in the plasma almost remain stationary because of their high mass compared with that of the electrons. The spatial separation of the electrons and ions in the plasma causes an imbalance of charges and thus creates wakefields in both longitudinal and transverse directions.

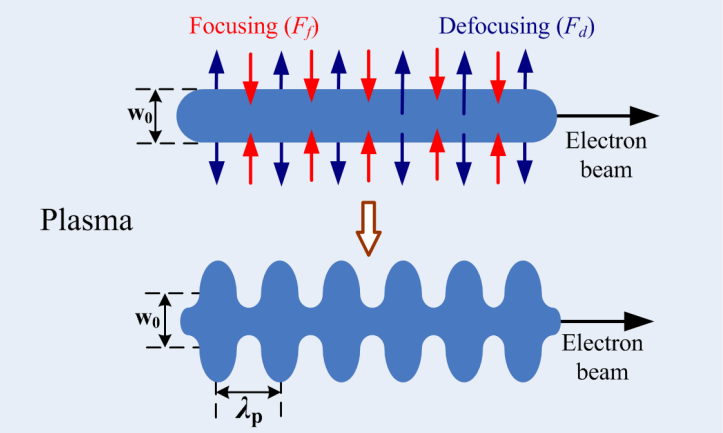


Figure 3.1: Schematic diagram of the evolution of charge distribution showing the self-modulation instability of a long electron bunch in a plasma (w_0 is the beam transverse size, λ_p is the plasma wavelength).

In the case of short (compare with λ_p) external intense laser pulses or charged particles (driver), the high longitudinal wakefield generated (gradients in the range from 10 to 100 GV/m) [58, 59, 60] can be used for the acceleration of charged particles. When the duration of the driver is much longer than the plasma period, the variation of the transverse wakefields along the driver become significant and cannot be neglected. As shown in Figure 3.1, particles at different positions along the long bunch undergo focusing or defocusing due to the periodic transverse forces. This modulation process will grow and it leads to the positive feedback

and unstable modulation of the whole beam along the beam propagation direction with a wavelength of λ_p. This is called beam self-modulation instability (SMI), which has been described and demonstrated in References [41, 42, 61].

In order to alleviate the effects of other instabilities in a plasma, such as hose instability which happens when there is a displacement of the transverse beam centroid from the propagation axis, the seeding of the SMI becomes necessary. The seeding of the SMI can be achieved by a shooting short driver in front of the beam (such as charged beam or laser pulse), or by modifying the beam itself to excite strong transverse wakefield and further to modulate the following particles.

As we are mainly considering moderate energy electron beam (< 100 MeV), it is feasible to manipulate the beam profile to achieve self-seeding of the SMI without using external short drivers. In the following sections, the self-seeding of beam modulation in a plasma is studied using an analytical model and PIC code VSim.

3.1.2 Theoretical analysis

For a beam moving through an initially homogeneous plasma channel while having charge density much less than the electron density of the plasma, the plasma wakefield generated can be described analytically using the linear wakefield theory [62, 63]. Here taking into account that the length of the beam is much larger than the wavelength of the plasma, I consider only the radial forces and their effects on beam dynamics. According to Reference [64], for an axis-symmetric beam, a slow amplitude envelope to describe the evolution of the time-integrated beam transverse size σ_r versus the longitudinal distance z along the beam propagation direction can be written as (see Appendix B for the derivation):

$$\frac{\partial^2 \sigma_r}{\partial z^2} - \frac{\varepsilon^2}{{\sigma_r}^3} - \frac{1}{\gamma m_0 c^2} \frac{\langle r W_r \rangle}{2\sigma_r} = 0 \tag{3.1}$$

where beam transverse size $\sigma_r = \sqrt{\langle r^2/2 \rangle}$, ε is the beam rms emittance, γ is the beam

relativistic factor, W_r is the radial force acting on a single electron.

In the model, the beam is considered to be divided into thin (compare with plasma wavelength) slices, meaning all electrons inside a slice have the same longitudinal velocity and can only move within the transverse plane. This model is reasonable and valid for relatively small energy modulation of electron beam with energy above 10 MeV. In this case, the modulation of the longitudinal velocities of particles induced by longitudinal wakefields can be neglected.

In an axisymmetric cylindrical system, $\langle r^2 \rangle = \int_0^{+\infty} r^2 n_b(r) r dr / \int_0^{+\infty} n_b(r) r dr$, which is the average of all electrons in the transverse direction. The radial force W_r can be written as (see Appendix C for the derivation):

$$\begin{aligned} W_r(\xi, r, z) &= W_{r1}(\xi, r, z) + W_{r2}(\xi, r, z) \\ W_{r1}(\xi, r, z) &= -\frac{e^2}{\epsilon_0 k_{pe}} \int_{+\infty}^{\xi} \sin k_{pe}(\xi - \xi') R(\xi', r, z) d\xi' \\ W_{r2}(\xi, r, z) &= \frac{e^2}{\epsilon_0 k_{pe}^2 \gamma^2} R(\xi, r, z) \end{aligned} \tag{3.2}$$

with

$$\begin{aligned} R(\xi, r, z) = &-k_{pe}^3 K_1(k_{pe} r) \int_0^r r' dr' n_b(\xi, r', z) I_0(k_{pe} r') \\ &+ k_{pe}^3 I_1(k_{pe} r) \int_r^{+\infty} r' dr' n_b(\xi, r', z) K_0(k_{pe} r') \end{aligned} \tag{3.3}$$

where W_{r1} is the focusing force caused by the plasma perturbation, W_{r2} represents the defocusing force due to the electrons' self-repulsion within the beam, $R(\xi, r, z)$ describes the dependence of wakefield on the bunch radial profile, k_{pe} is the plasma wave number, $\xi = -v_b t + z$ is a co-moving variable, which indicates the relative position in the beam, $n_b(\xi, r, z)$ is beam charge density distribution and $I_{0,1}$ and $K_{0,1}$ are the modified Bessel functions of the zeroth and first order.

3.1.3 Dependence of modulation on the parameters of beam and plasma

To evaluate the radial forces acting upon the beam and the beam dynamics, the initial beam transverse profile is assumed to be Gaussian with the transverse size σ_r changing with the propagation distance in the plasma, while the longitudinal profile can be of an arbitrary geometry. In this case, the average of rW_r can be written as:

$$\langle rW_r \rangle = \frac{1}{\sigma_r^2(z,\xi)} \int_0^{+\infty} rW_r(\xi, r, z) e^{-r^2/2\sigma_r^2(z,\xi)} r dr \tag{3.4}$$

The solution of $\sigma_r(z,\xi)$ as a function of z and ξ in Equation 3.1 can be found numerically. It is clear that the structure of the bunch will affect the forces acting on it. Two possible beam longitudinal profiles are discussed in the following sections, which include a trapezoidal profile and a Gaussian profile as shown in Figure 3.2. The trapezoidal profile means the beam has an uniform charge distribution in the middle part and rise and decay slopes (with the corresponding rise/decay times), which are defined from zero to maximum charge density; if the rise and decay times are considered equal to zero, the longitudinal profile is square (bunch with square profile has been considered in References [39, 65]). According to the previous definition of the relative position of the beam ξ, it has a unit of length. In order to analyse the periodicity of the beam modulation in the unit of time, all the axes in the figures in this chapter which involve with the relative position of the beam ξ are shown in the time unit.

Beam with trapezoidal profile

Starting with a beam of square profile with the parameters listed in the Table 3.1, the beam density can be written as $n_b(r) = n_{b0} \exp(-r^2/2\sigma_r^2)$ with $n_{b0} = Q/2\pi e L \sigma_{r0}^2 = 2.3 \times 10^{13}/\mathrm{cm}^3$. To obtain plasma period of 1 ps (λ_p=300 μm), the plasma density n_p should be $1.24 \times 10^{16}/\mathrm{cm}^3$ (plasma frequency $\omega_p = \sqrt{n_p e^2/m_0\epsilon_0}$) and $n_{b0}/n_p \approx 0.2\%$, meaning that

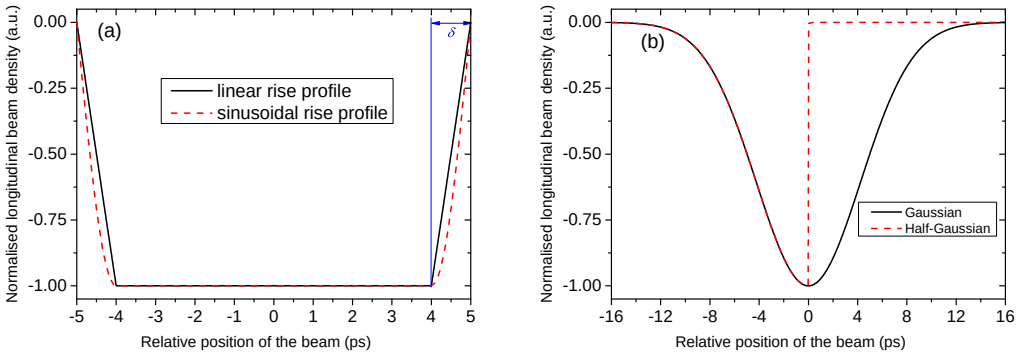


Figure 3.2: Normalised longitudinal charge density distributions of beams with trapezoidal profile (a) and Gaussian profile (b).

one can consider the beam-plasma interaction to be in the linear regime.

Table 3.1: Beam and plasma parameters

Description	Parameters	Value
Beam energy	E	50 MeV
Beam charge	Q	1 nC
Beam length	L	3000 μm (10 ps)
Beam transverse size	σ_{r0}	120 μm
Beam emittance	ε	1 mm mrad
Plasma period	T_p	0.5 ps, 0.67 ps, 1 ps
Beam rise profile	-	linear, sinusoidal
Beam rise time	δ	0, $0.5T_p$, T_p, $1.5T_p$

The goal of the studies carried out here is to maximise the beam modulation and a number of parameters can be varied to achieve it. Considering the beam parameters listed in the Table 3.1 and using the beam envelope model described above, the evolution of the bunch transverse size $\sigma_r(z, \xi)$ can be investigated. The results of the semi-analytical studies of the beam modulation for different plasma densities are shown in Figure 3.3(a). It shows that a long bunch with a length of 10 ps has been modulated into a train of microbunches after propagating through a 3.6 cm long plasma channel. The microbunches observed are equidistant, with periodicities of 1 ps, 0.67 ps, and 0.5 ps corresponding to the specific plasma period defined by the plasma density. For a given length of the plasma channel, increasing the plasma density meaning reducing the plasma period. It results in a decrease in the modulation periodicity as well as the amplitude of the modulations. The reason is that, the perturbation induced by electron beam decreases when increasing the plasma density,

which means smaller transverse focusing and defocusing forces acting upon the beam and thus leads to smaller modulation rate.

Looking at the evolution of the beam modulation (Figure 3.3(b)), we see that a longer propagation distance L_p results in a higher beam modulation amplitude for fixed beam parameters. An initial unmodulated beam after a short propagation distance ($< 15\lambda_p$, λ_p=300 μm) (solid green line) still has no clear modulation. With the increase in the propagation distance, a periodic modulation occurs along the beam which can clearly be seen in the range from $45\lambda_p$ to $90\lambda_p$. At longer propagation distances ($> 90\lambda_p$), the amplitude of the modulation starts to vary. The modulation is stronger at the tail and weaker at the head (non-uniform modulation). The interaction between the beam and the wakefield becomes non-linear and more accurate numerical modelling is required to describe the beam-plasma interaction.

To further improve the beam modulation in a plasma channel, it is worth noting that the initial bunch profile also has a significant impact on the beam modulation. Previous studies [66] have shown that the beam modulation depends on the longitudinal rise time and the strong self-modulation instability happens if the rise profile is sharp ($\delta \ll T_p$), with a general rule that a shorter rise time leads to a larger modulation rate. Nevertheless, this instability can also be observed for electron beams with a relatively long rise time ($\delta \sim T_p$) which simplifies the beam profiling. The dependence of the modulation on the initial rise profile of the beam is shown in Figure 3.3(c) and Figure 3.3(d). In particular, two initial rise time profiles were considered: linear and sinusoidal. In the case of the linear rise time profile, if the rise time is equal to a multiple of the plasma period ($\delta = nT_p$), only beam compression (focusing) takes place. However, if the rise time is not linear, some weak periodic modulations are still visible even if the rise time $\delta = nT_p$.

The analysis of the dependence of the transverse wakefield on the initial bunch profiles, especially on its rise time and on the shape of the leading edges, is in the following. Assuming the initial particle distributions in the longitudinal and transverse directions are uncorrelated,

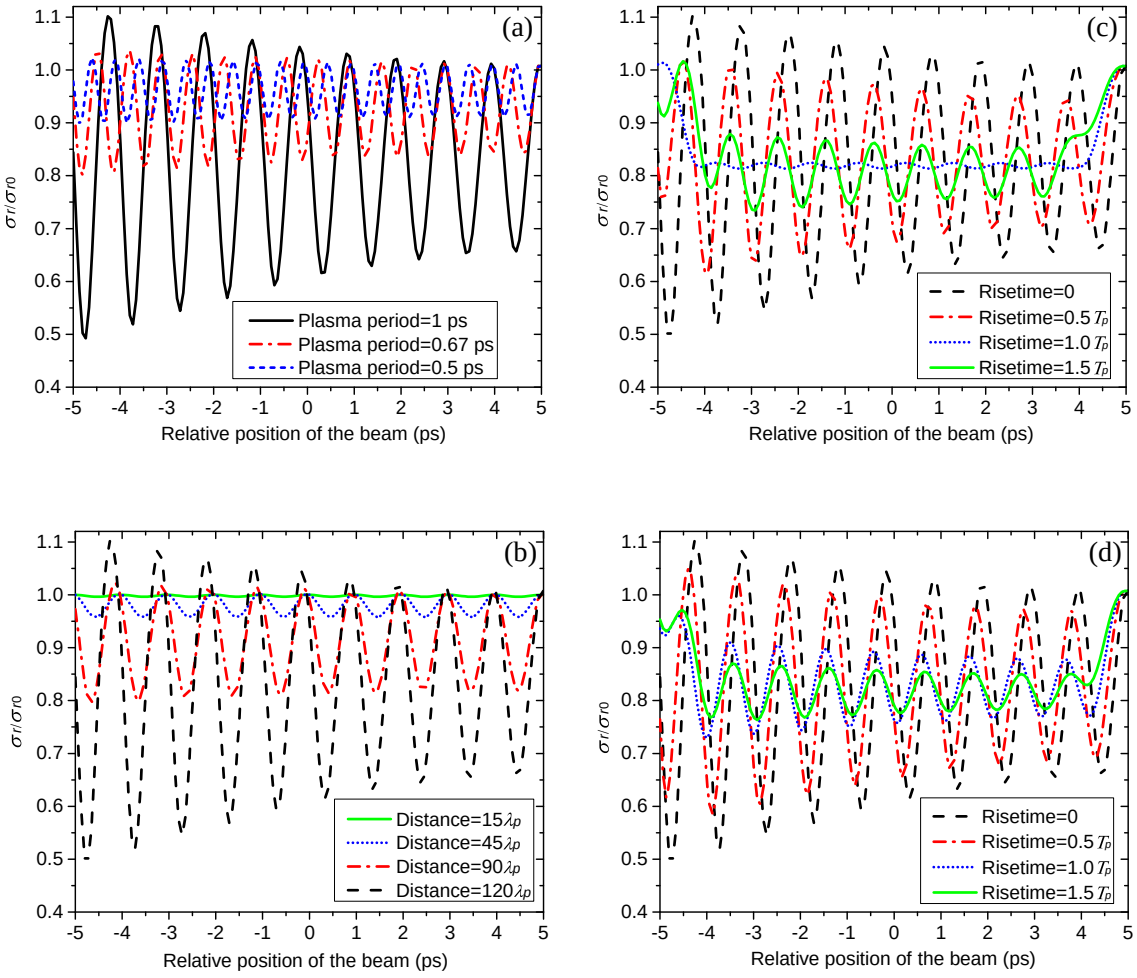


Figure 3.3: The beam modulation parameter σ_r/σ_{r0} plotted as a function of the position along the plasma channel for: (a) different plasma periods (L_p=3.6 cm); (b) different propagation distances (plasma period T_p=1 ps); (c) various linear rise times (T_p=1 ps, λ_p=300 μm, L_p=120λ_p); (d) various sinusoidal rise times (T_p=1 ps, L_p=120λ_p). Other beam parameters were E=50 MeV, Q=1 nC.

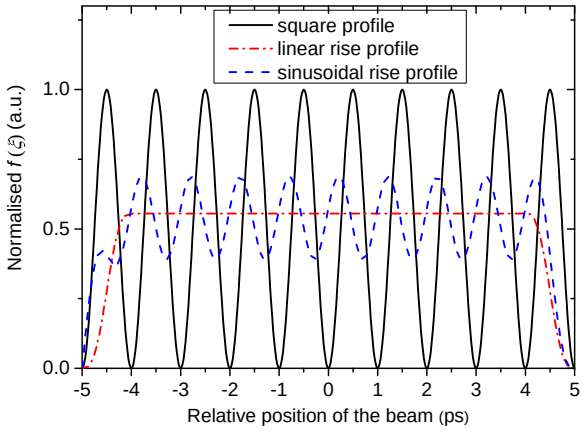


Figure 3.4: Dependence of function $f(\xi)$ on different bunch profiles (plasma period T_p=1 ps): square profile (solid black line); trapezoidal profile with a linear rise time of T_p (red dash-dotted line); trapezoidal profile with a sinusoidal rise time of T_p (blue dashed line).

the beam density can be written as:

$$n_b(\xi, r) = n_{b_\parallel}(\xi) n_{b_\perp}(r) \tag{3.5}$$

The transverse force W_{r1} can be written as $W_{r1} = f(\xi)g(r)$ and we have:

$$\begin{aligned} f(\xi) &= -\frac{e^2}{\epsilon_0 k_{pe}} \int_{+\infty}^{\xi} n_{b_\parallel}(\xi') \sin k_{pe}(\xi - \xi') d\xi' \\ g(r) &= -k_{pe}^3 K_1(k_{pe} r) \int_0^r r' dr' n_{b_\perp}(r') I_0(k_{pe} r') \\ &\quad + k_{pe}^3 I_1(k_{pe} r) \int_r^{+\infty} r' dr' n_{b_\perp}(r') K_0(k_{pe} r') \end{aligned} \tag{3.6}$$

where $f(\xi)$ depends on the longitudinal profile $n_{b_\parallel}(\xi)$ and $g(r)$ depends on the transverse profile $n_{b_\perp}(r)$.

The dependence of $f(\xi)$ on the longitudinal profile is shown in Figure 3.4. For the beam with linear rise time equal to the plasma period, there is no oscillation of the wakefield component $f(\xi)$, while the oscillating component does not become zero for sinusoidal rise beam or square beam. Therefore, in the case of the beam with linear rise time equal to the plasma period there is only spatially constant force acting on the beam and the beam is not

modulated, while a beam with sinusoidal rise time also equal to the plasma period can still be modulated. Also, one can see that the oscillation amplitude of $f(\xi)$ for the square profile is larger than that of the rise time of λ_p, which means a larger modulation force. As a result, to observe strong beam modulation one has to condition the beam rise time to make it as short as possible (see Appendix C for detailed analysis).

Beam with Gaussian profile

Here the modulation of the beams with Gaussian profile and half-Gaussian profile in the longitudinal direction are discussed. For the Gaussian profile, the beam parameters are the same as the listed parameters in the Table 3.1, except that the longitudinal full width at half maximum (FWHM) equals to 10 ps. For the half-Gaussian profile, it is assumed that the front half part of the beam is removed (only half of the total charge is left).

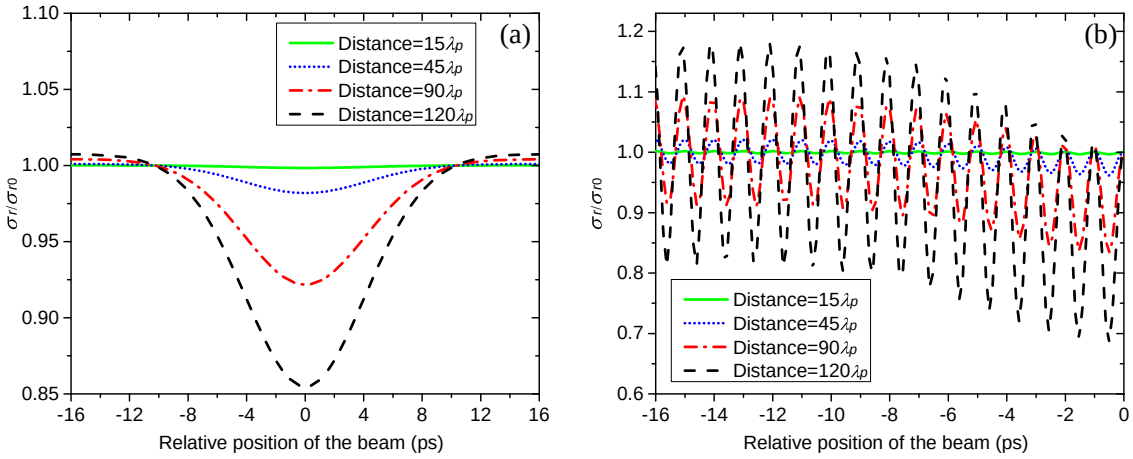


Figure 3.5: The beam modulation parameter σ_r/σ_{r0} plotted as a function of the position along the plasma channel for (a) full Gaussian and (b) half-Gaussian profile at the propagation distances L_p=15λ_p (solid green line), 45λ_p (blue dotted line), 90λ_p (red dash-dotted line) and 120λ_p (black dashed line). Other parameters were: E=50 MeV, Q=1 nC (Gaussian), 0.5 nC (half-Gaussian), and λ_p=300 μm.

It can be seen in Figure 3.5 that, most of the full Gaussian beam is compressed in the transverse plane without periodic modulation and the charge density on the axis becomes larger. While the periodic modulation is clear for a beam with half-Gaussian profile. The explanation is that a half-Gaussian profile can cause oscillating transverse wakefield along

the beam and modulate the beam in the transverse plane. The key point of seeding self-modulation is to create an oscillating wakefield and the sudden change of beam density is one method. Other ways include letting another seeding particle beam or laser pulse propagate in the plasma channel in front of the beam and the wakefield generated by the driver can be used to modulate the following particle beam.

3.2 Numerical studies of beam modulation

There are a number of PIC codes capable of beam-plasma simulations and here the VSim code is considered to investigate the beam modulation in a plasma channel. The simulations were carried out using a frame co-moving with the electron beam. In this case I assume that the EM radiation outside the numerical box cannot affect the beam and the plasma dynamics inside the box. This is a reasonable approximation, taking into account that the beam travels with a speed close to the speed of light (ultra-relativistic beam) and allows a significant reduction of the calculation time. The initial plasma density is set to be uniform in the whole simulation area. Also it is assumed that the ions in the plasma are stationary. In the following, the investigation of beam modulation in a plasma has been carried out for different beam profiles.

3.2.1 Dependence of modulation on bunch profiles

Beam with trapezoidal profile

The dimensions of the simulation box were 3300 μm (longitudinal direction) by 600 μm (transverse direction) and it was divided into 660 cells by 318 cells, respectively. Figure 3.6 shows the modulated profile of a trapezoidal beam with various rise and decay times as listed in Table 3.1.

Figures 3.6 (b), 3.6(c), and 3.6(d) illustrate the results of the numerical studies and show the influence of the plasma density on a square beam. It can be seen that, after propagating

a distance of 2.1 cm, the beams have different periodicities and amplitudes of modulation. The beam in Figure 3.6(b) is fully modulated with a periodicity of 1 ps, while the beams in Figures 3.6(c) and 3.6(d) are partially modulated with the respective periodicities of 0.67 ps and 0.5 ps, confirming the results observed in Section 3.1.

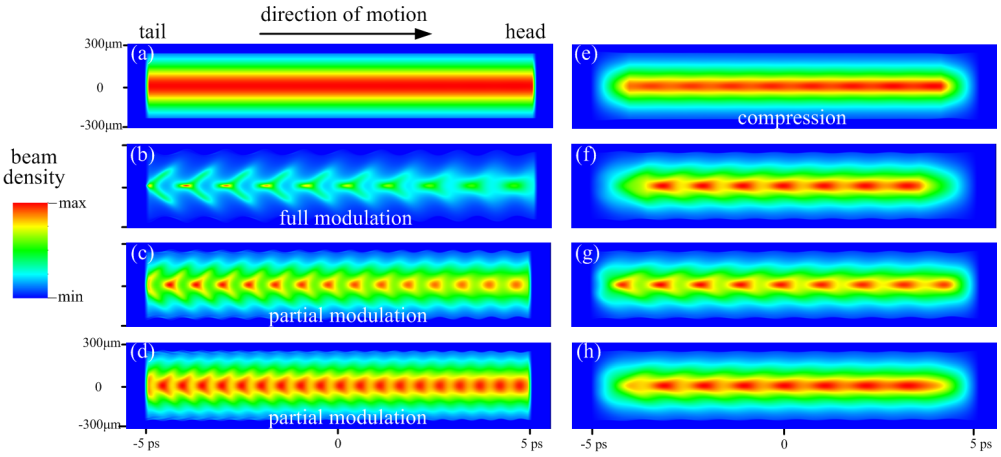


Figure 3.6: Numerical simulations of the bunch modulation after propagating a distance of 2.1 cm, for different plasma densities and bunch profiles: (a) initial charge distribution with square profile; (b)-(d) square beam profile with plasma periods T_p of 1 ps (b), 0.67 ps (c), and 0.5 ps (d), respectively; (e)-(h) plasma period T_p of 1 ps, trapezoidal profile with linear rise time of T_p (e) and $1.5T_p$ (f), trapezoidal profile with sinusoidal rise time of T_p (g) and $1.5T_p$ (h). Other beam parameters: E=50 MeV, Q=1 nC.

For Figures 3.6(e) to 3.6(h), the plasma density $n_p = 1.24 \times 10^{16}/\text{cm}^3$ was fixed (T_p=1 ps) and a trapezoidal bunch profile has been assumed. The bunch rise time has been varied as shown in the figure caption. The comparison of Figure 3.6(b) with Figures 3.6(e) - 3.6(h) shows that the modulation rate is largest for a square beam.

As observed before (Figure 3.3), Figure 3.6(e) shows that for a beam with a linear rise time equal to the plasma period, beam compression without periodic modulation is predicted. While for the same rise time, the modulation of the beam with a sinusoidal rise profile is clearly shown in Figure 3.6(g). Additionally, Figures 3.6(b) - 3.6(d) show that the modulation for the trailing edge of the beam (left) is larger than that of the leading edge (right), which is in good agreement with the beam envelope model.

Beam with Gaussian profile

Similar simulations have been carried out in VSim to investigate the modulation of beams with full Gaussian profile and half-Gaussian profile. The beam and plasma parameters are the same as the ones in the above analysis. In Figure 3.7, we can see the half-Gaussian beam is divided into a train of microbunches after propagating 3 cm in the plasma, while the full Gaussian beam is only compressed, without a clear periodic modulation. The VSim PIC simulation results are consistent with the theoretical analysis.

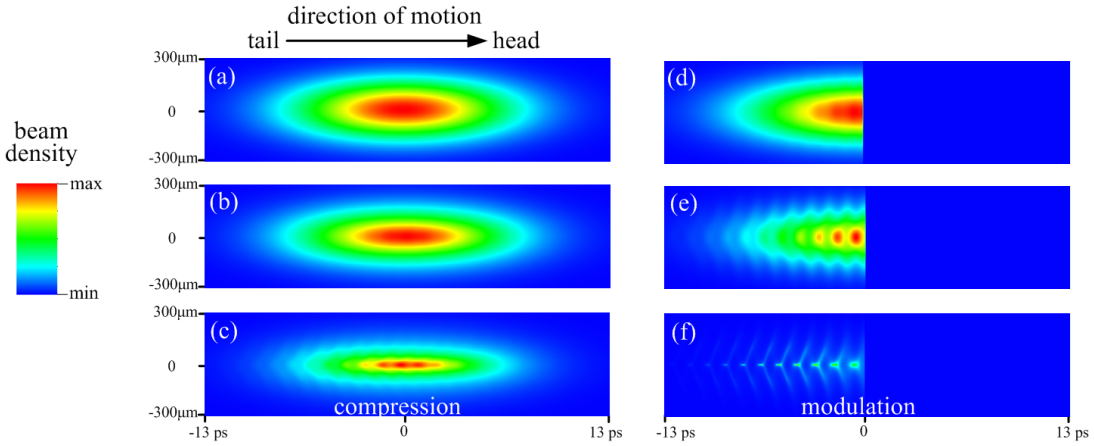


Figure 3.7: Numerical simulations of the beam modulation for Gaussian profile (left) and haf-Gaussian profile (right) after propagating the distance of 1 cm (a, d), 2 cm (b, e) and 3 cm (c, f) in a plasma with a period T_p of 1 ps (λ_p=300 μm).

We notice that, for the full Gaussian beam, the plasma can be used as a lens to compress the beam. This may find application in the area of beam dynamics. By appropriate design, the beam can be focused into a much smaller size in a very short distance in the plasma.

All of these simulations are consistent with the analytical results obtained from the beam envelope model in the previous section. This also underlines the importance of initial beam conditioning, for example, profiling of the beam rise time, to observe strong modulation within the shortest distance.

3.2.2 Comparison of theoretical analysis with numerical predictions

In the following, the comparison between analytical calculation and PIC simulation for the modulation of trapezoidal beam in plasma channel will be discussed. The beam parameters are listed in the Table 3.1 (square beam is used) and the plasma period is set to be 1 ps (λ_p=300 μm). The charge densities on axis obtained from the analytical calculation and the PIC simulation are shown in Figure 3.8. The charge densities are very similar when the propagation distance is less than $45\lambda_p$. However, the difference can be significant after the propagation distance of $75\lambda_p$.

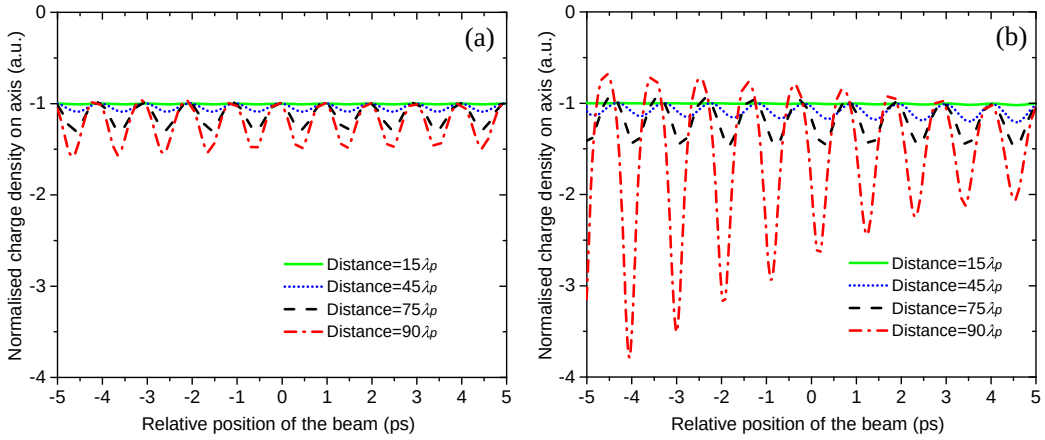


Figure 3.8: Comparison of the charge density distributions on axis obtained from theoretical analysis (a) and VSim simulation (b). The plasma wavelength λ_p is 300 μm.

One possible explanation for the difference can be as follows, In the theoretical calculation, the Gaussian profile in the transverse plane is assumed to be fulfilled. But in reality, this assumption is not always appropriate, especially at the late stage of the beam-plasma interaction. Another reason could be that the wakefield is calculated based on the assumption of a linear interaction between the beam and the plasma. At the late stage of interaction, the beam density on axis is many times larger than the initial density and it could be comparable with the plasma density. As a result, the theoretical model described is only applicable to the description of small perturbations (at the start of the interaction). Nevertheless, it gives

us an important insight into the physics allowing us to limit the range of the parameters used at the next stage of the investigations, which uses numerical models.

There are some limitations of the above PIC simulation in VSim as well. The beam is assumed to be axial-symmetric in the 2D cylindrical coordinate, without considering any off-centring. In order to simulate the beam modulation more accurately, full 3D simulations are necessary. This requires computing cluster with hundreds of cores.

3.3 Numerical studies of beam collimation and propagation in vacuum area

In order to study the THz radiation generated by the plasma modulated beam, the following steps should be considered: importing the beam from the plasma channel to the vacuum area, transforming the transverse modulation of the initial plasma modulated beam into longitudinal modulation, and transporting the longitudinally modulated beam to the interaction region. In this section, the beam collimation and the transport of the modulated beam are investigated and discussed, using numerical methods based on VSim.

3.3.1 Beam collimation from plasma channel to vacuum region

The beam modulation discussed above is caused by the self-modulation instability in plasma. The focusing and defocusing forces acting on the beam make the transverse charge distribution vary. Nevertheless, the total current of the beam or total charge across a given cross section does not change. This means that there is no modulation of the beam current or of the number of electrons across each transverse plane, in spite of the fact that the transverse size of the defocused part of the beam is different from that of the focused part. In order to generate THz radiation one may try positioning the target close to the focused part of the beam. However, to avoid directly striking the target with defocused electrons, the target has to be moved outside the beam trajectory, which would have a strong effect on the generation

of EM radiation. To resolve this issue, one solution would be to remove the defocused part of the modulated beam, for example, using a suitable collimator. The collimator can be a block of metal or magnet dipoles to divert the defocused electrons from the main orbit.

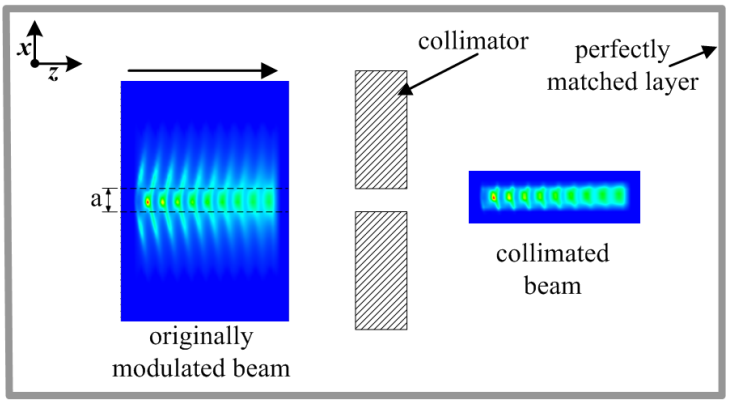


Figure 3.9: A schematic of the VSim simulation showing the beam propagation through a collimator.

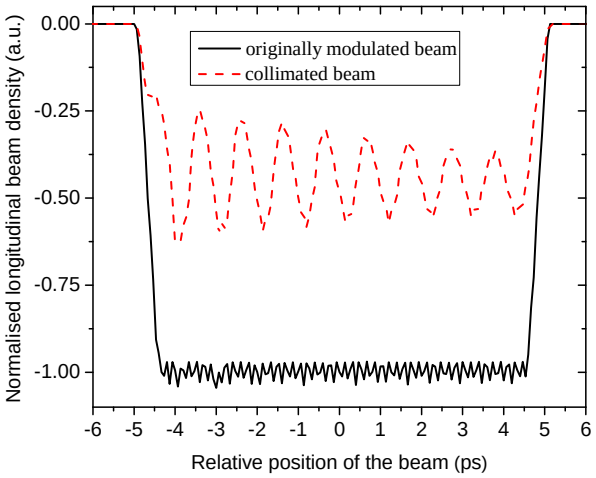


Figure 3.10: Normalised longitudinal charge distribution along the beam propagation direction for originally modulated beam and collimated beam.

The first step is to bring the initial modulated beam from the plasma channel into the vacuum area. This was achieved by transferring all the beam parameters and self-fields into a new simulation database. These parameters were then used as initial conditions at the start of the beam transport. The schematic of the numerical box is shown in Figure 3.9. The modulated beam (Figure 3.6(b), modulation periodicity of 1 ps), was brought into the vacuum simulation area and collimated using an aperture with a diameter of a=100 μm.

After the collimator, the train of microbunches was only made up of radially compressed electrons. The comparison of the longitudinal beam profiles $n(z)$ before (solid black line) and after the collimator (red dashed line) are shown in Figure 3.10. By removing the defocused part of the beam, a clear longitudinal modulation with a periodicity of 1 ps was observed. Charge loss due to beam collimation is inevitable for this method. About half of the total charge is lost during the collimation procedure described above.

3.3.2 Beam propagation in vacuum drift area

In the vacuum there is no possibility of charged background, such as plasma neutralising the space charge fields of the beam. The modulated beam experiences defocusing forces due to this field and therefore it is important to investigate beam dispersion and consider conditions when the microbunched beam can propagate to the THz target while maintaining the required periodicity. In order to understand the stability of the beam modulation, beams of different energies have been considered.

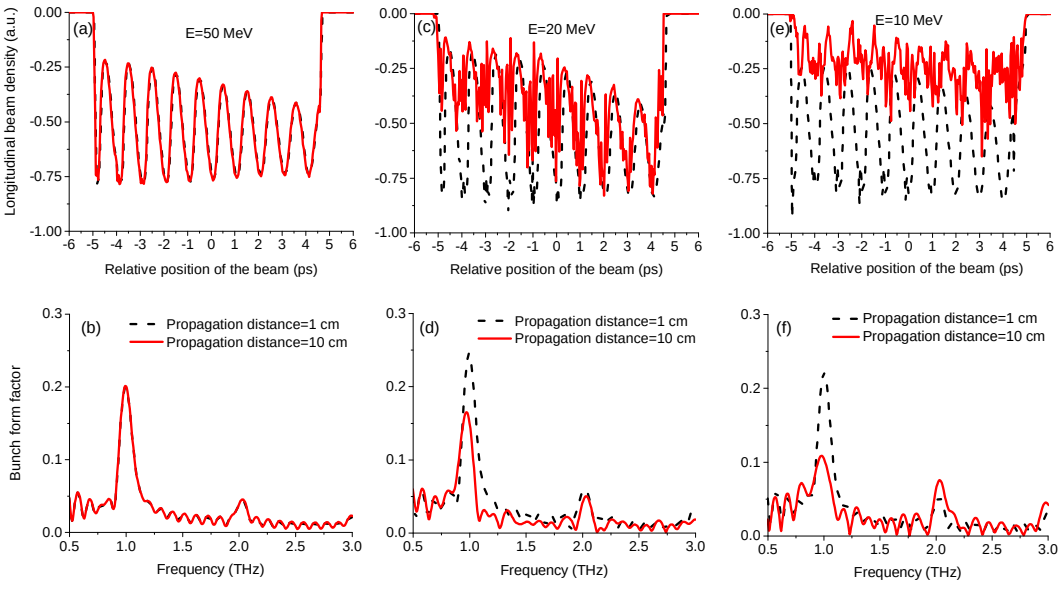


Figure 3.11: Comparison of the bunch profiles (top) and the corresponding form factors (bottom) after propagating 1 cm (black dashed line) and 10 cm (solid red line) in vacuum when the beam energy is 50 MeV (a, b), 20 MeV (c, d), and 10 MeV (e, f).

Using the beam parameters listed in Table 3.1 (but varying beam energy) and assuming the plasma period is 1 ps, the propagation of plasma modulated beams after collimation with energies of 10 MeV, 20 MeV, and 50 MeV were studied numerically. Higher beam energy leads to smaller amplitude of beam density modulation (for a given length of the plasma channel). In order to get the same modulation for beams of different energies, plasma channels of different lengths 1 cm (10 MeV), 1.5 cm (20 MeV), and 2.2 cm (50 MeV) were used in the simulations. The comparison of the collimated beam profiles after propagating over a distance of 1 cm (black dashed line) and 10 cm (solid red line) in vacuum is shown in Figure 3.11. In this case, the longitudinal beam density is the integration of all the particles within a 200 μm diameter around the beam axis. The electrons outside the region were considered as lost. The diameter of 200 μm was assumed here because smaller bunch size helps to reduce the separation between grating and the beam, which in turn increases the efficiency of generation of Smith-Purcell radiation.

With the decreasing in beam energy, the number of electrons reaching the end of the simulation range becomes smaller and longitudinal modulation becomes less clear due to both longitudinal and transverse dispersion becoming stronger. This can be seen by the comparison of Figures 3.11(b) and 3.11(f). For beams with energies above 20 MeV, the longitudinal modulation of the microbunched beam can be preserved well over the simulation distance of 10 cm. However, the preservation of the beam modulation for energies below 20 MeV is not as good. The bunch form factor becomes much smaller after the propagation and the same is true for the total bunch charge, as many electrons were lost from the defined region. For example, the total charge for a 10 MeV beam within the area is around half of the initial total charge.

In practice, this means that an increase in the beam energy would increase the distance over which modulation can be maintained, illustrating a clear advantage of high energy beams for THz radiation generation.

3.3.3 Dependence of beam modulation depth on plasma parameters

Considering a beam with an energy of 50 MeV, the beam modulation can be kept almost unchanged during the propagation in vacuum for a long enough distance to interact with the target. Assuming a trapezoidal beam with the parameters listed in the Table 3.1 and the linear rise time of $0.1T_p$ (T_p=1 ps), numerical studies have been carried out to investigate the modulation depth of the beam propagating through a plasma channel of different lengths.

The charge distributions of the collimated beams (following the same collimation procedure as above) for several values of the plasma channel length are shown in Figures 3.12 - 3.14. The corresponding normalised longitudinal beam charge densities and the bunch form factors are shown in Figures 3.15 - 3.17.

We can see that, by changing the plasma density, the bunch form factors of the microbunched beam peak at frequencies of 1 THz, 1.5 THz, and 2 THz, which correspond to the plasma frequencies. The beam modulation increases as the length of plasma channel increases. However, this is correct if the transverse size of the bunch is not over-compressed, as over-compression will lead to the space charge force exceeding the focusing force of the plasma.

It can be seen that the maximum bunch form factor of the collimated beam in Figure 3.12 is around 0.4 at the frequency of 1 THz. For the same beam parameters, the optimal modulation distance is different for different plasma densities. The optimal distance can be up to 3.7 cm for a plasma with a period of 0.5 ps while the optimal distance is around 3 cm for a plasma with a period of 1 ps.

One also needs to be careful with the tail of the beam. As shown previously, at the late stage of beam-plasma interaction, the tail experiences a larger modulation than the head. Using longer plasma channels to observe stronger modulation of the head leads to defocusing of the tail and it results in a further loss of total charge.

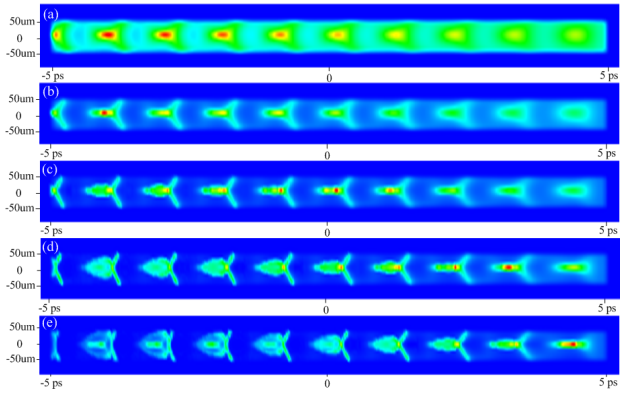


Figure 3.12: Charge distributions of a collimated beam with propagation distances of 2.1 cm (a), 2.3 cm (b), 2.6 cm (c), 2.8 cm (d), and 3.0 cm (e) in a plasma with a plasma period of 1 ps.

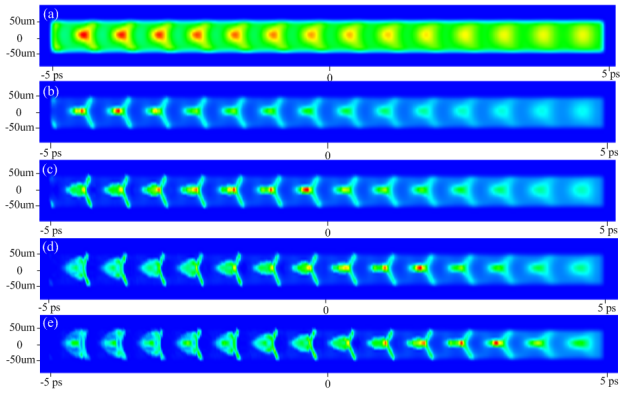


Figure 3.13: Charge distributions of a collimated beam with propagation distances of 2.3 cm (a), 2.8 cm (b), 3.0 cm (c), 3.3 cm (d), and 3.5 cm (e) in a plasma with a plasma period of 0.67 ps.

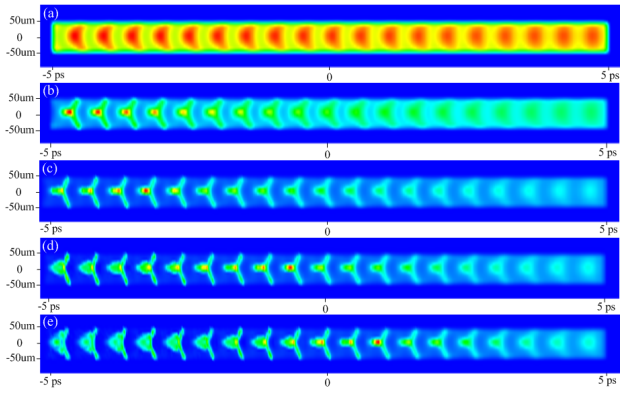


Figure 3.14: Charge distributions of a collimated beam with propagation distances of 2.3 cm (a), 3.0 cm (b), 3.2 cm (c), 3.5 cm (d), and 3.7 cm (e) in a plasma with a plasma period of 0.5 ps.

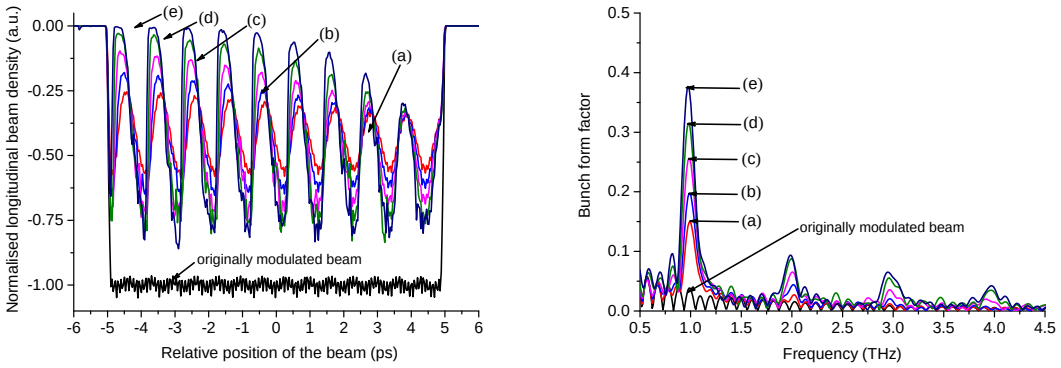


Figure 3.15: Comparison of the charge density distributions (left) and their corresponding bunch form factors (right) for beams shown in Figure 3.12.

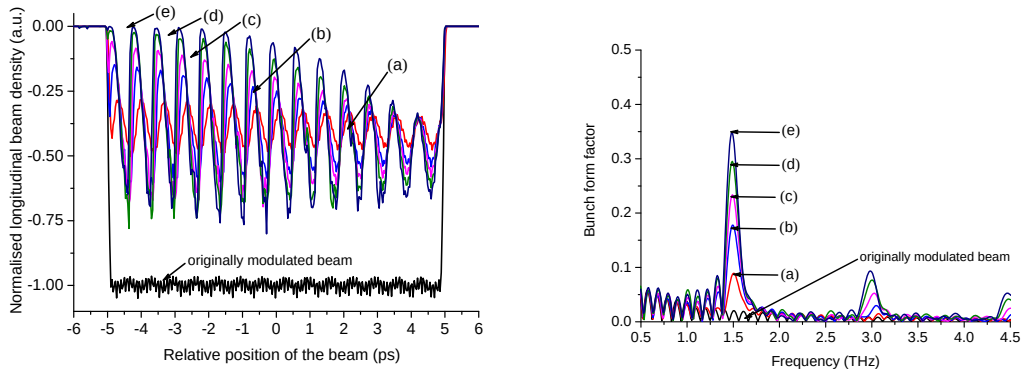


Figure 3.16: Comparison of the charge density distributions (left) and their corresponding bunch form factors (right) for beams shown in Figure 3.13.

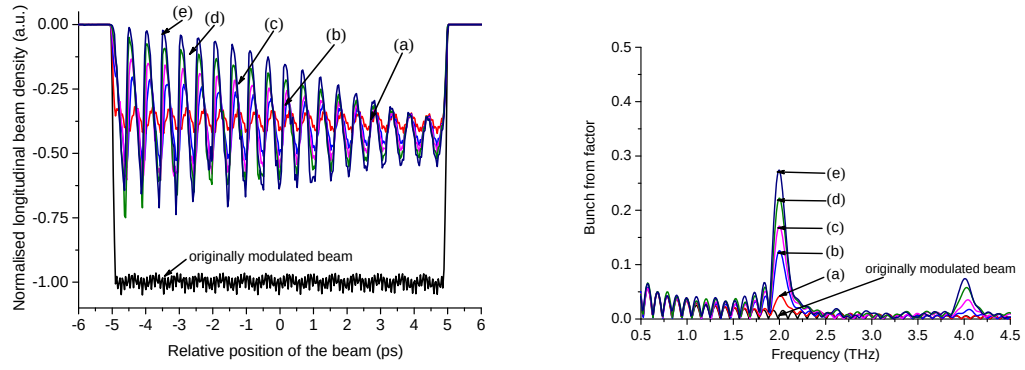


Figure 3.17: Comparison of the charge density distributions (left) and their corresponding bunch form factors (right) for beams shown in Figure 3.14.

3.4 THz radiation generated by plasma modulated microbunches

The THz radiation generated by the microbunched beams has been investigated using VSim. In general, Smith-Purcell, Cherenkov, transition or diffraction radiation mechanisms can be used for THz radiation generation. As mentioned before, there are a number of advantages of Smith-Purcell radiation compared with others and only the Smith-Purcell mechanism will be considered.

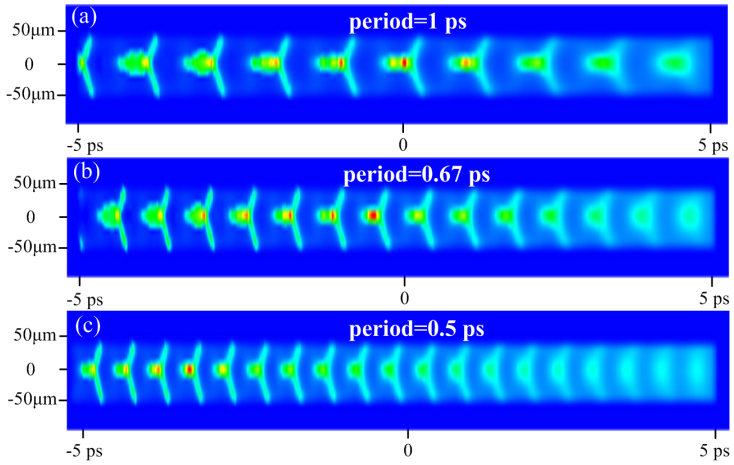


Figure 3.18: Contour plots of the charge distributions of microbunch trains after beam collimation with microbunch periodicities of (a) 1 ps, (b) 0.67 ps, and (c) 0.5 ps. Beam energy=50 MeV.

Simulations were carried out in the near-field region. The simulation schematic is similar to that shown in Figure 2.7 and a grating with the same parameters were used. The distance between the beam centre and the grating was maintained 0.5 mm.

Figure 3.18 shows the microbunched beams with periodicities of 1 ps, 0.67 ps, and 0.5 ps used in the numerical simulations. Fourier transforms of the radiation signal B_y generated by these microbunches are shown in Figure 3.19. There are clear peaks at 1 THz, 1.5 THz, and 2 THz and they correspond to the microbunch periodicities.

The microbunching effect of the beam ensures that its radiation spectrum in the near-field region corresponds to the spectrum of the microbunch trains. The tunability of the

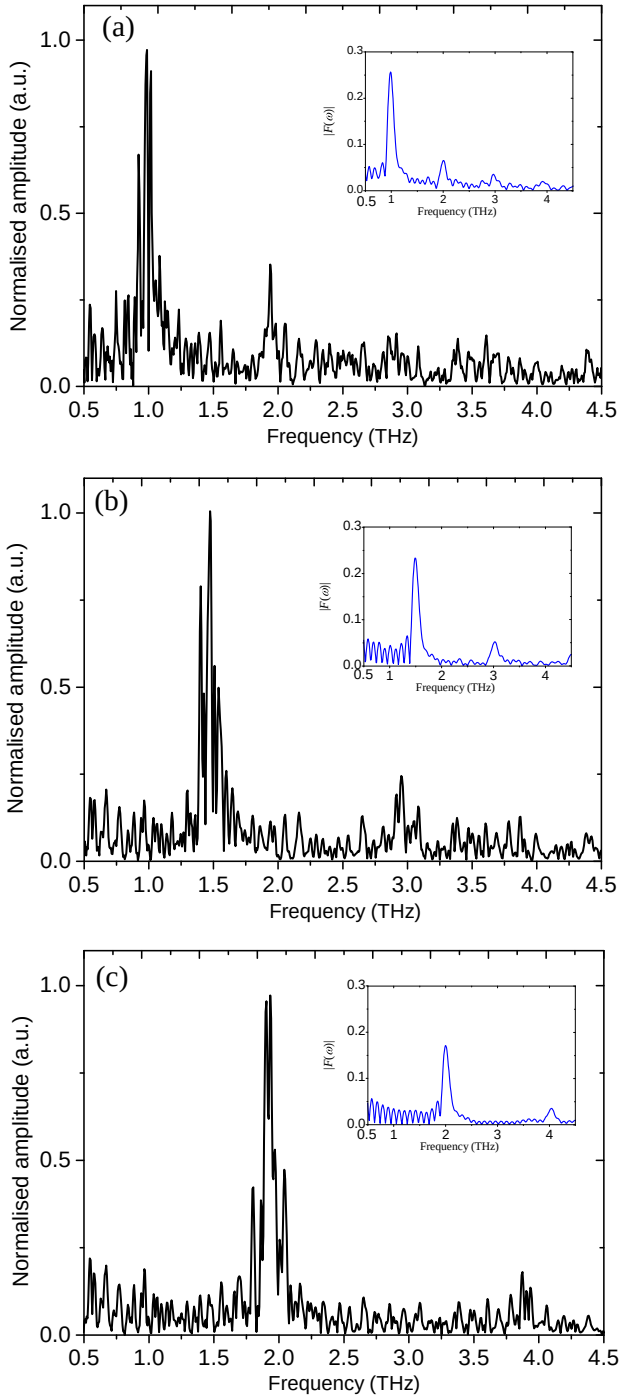


Figure 3.19: Normalised spectra of the radiation generated by microbunch trains after beam collimation with microbunch periodicities of 1 ps, 0.67 ps, and 0.5 ps (insets are the form factors of the corresponding modulated beams in Figure 3.18).

radiation is achieved by varying the periodicity of microbunch trains which, in turn, can be controlled by the plasma density. In this case, a change of the grating period is not required. Assuming plasma density in the range of $10^{15}/\text{cm}^3$ to $10^{17}/\text{cm}^3$, the frequency tunability would be between 0.3 THz and 3 THz. Also, no external cavity is required and the interaction region defined by the grating is rather compact (a few hundreds of periods in THz range). This proposed method could potentially be less complex and costly than a THz Free Electron Laser for the same frequency ranges.

3.5 Summary

I have discussed the modulation of a picosecond-long relativistic electron beam into a train of microbunches. The interaction between the long electron bunch and a plasma channel was studied using both analytical theory and numerical simulations. Based on the analytical beam envelope model, the parameters which affect the beam modulation have been analysed, including the plasma density, the beam propagation distance inside the plasma, and the longitudinal profile of the original, unmodulated bunch. Good agreement between PIC simulations and the analytical model was observed. The beam collimation required to observe efficient transfer of the beam energy into THz radiation was also studied. Our simulations show that the interaction of a plasma modulated and collimated beam with a metallic grating would result in the emission of coherent THz radiation with a spectrum determined by the microbunch spacing in the near-field region. Hence, it would be possible to consider a tunable THz radiation source where the tunability is achieved by changing the microbunch periodicity, which is in turn controlled by the plasma density.

Chapter 4

Generation of microbunch trains in photocathode RF gun and the monitoring of microbunch separation

In this chapter, the experiments carried out at the KEK-LUCX facility are presented. The goals of the experiments are to demonstrate the possibility of generating and controlling a train of electron microbunches using a photocathode RF gun and to develop a technique which enables the monitoring of the separation between microbunches. First, the generation of microbunches from a photocathode RF gun is discussed and the factors affecting the microbunch separation are investigated analytically. Based on the analysis of the spectrum of coherent Smith-Purcell radiation (cSPr) generated by microbunches, a diagnostic method capable of monitoring the microbunch separation is suggested. Microbunch separations are determined using experimental data obtained for a number of cases. By comparing the experimental results with the predictions from an analytical model, the diagnostic method is evaluated. Potential applications and possible challenges are also discussed.

4.1 Generation of microbunch trains at KEK-LUCX

4.1.1 An introduction to the KEK-LUCX facility

The Laser Undulator Compact X-ray source facility (LUCX), KEK (High Energy Accelerator Research Organization) is an experimental facility which has been used to investigate various mechanisms of EM radiation at THz frequencies and in the X-ray range, such as Smith-Purcell radiation, Cherenkov radiation, undulator radiation and Compton scattering. A schematic layout of the KEK-LUCX facility is shown in Figure 4.1.

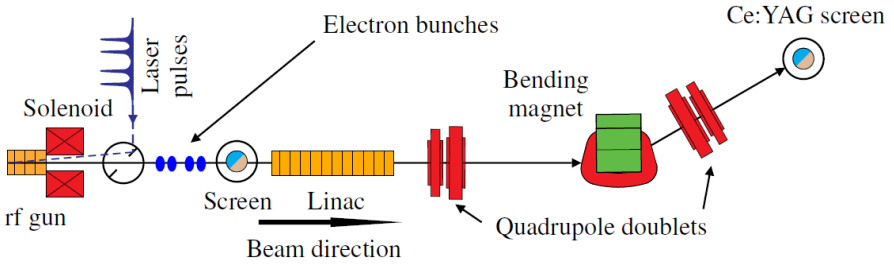


Figure 4.1: Schematic layout of the KEK-LUCX facility [36].

By illuminating a photocathode embedded in 3.6-cell RF cavity with a series of femtosecond laser pulses, electron microbunches are emitted sequentially. The photocathode is made of cesium telluride (Cs_2Te), which is a p-type semiconductor with a bandgap of 3.2 eV. It can be illuminated with UV lasers to generate electron bunches. In the experiments, a Titanium-Sapphire laser (Ti:Sa, third harmonic at 266 nm) was used [35]. Cs_2Te can withstand high field strengths (up to 100 MV/m) and has ps response time. The quantum efficiency is up to 10%. A interaction vacuum chamber (not noted in Figure 4.1), with a rotating platform inside, is positioned just downstream of the solenoid (1.3 m away from the photocathode), where targets can be installed for the investigation of different radiation mechanisms. There are no beam dispersive or compressive elements between the RF gun and the interaction chamber.

The parameters of the KEK-LUCX accelerator relevant to the experiments are given in Table 4.1.

Table 4.1: KEK-LUCX parameters

Parameter	**Expected values**
Beam energy (typ)	8 MeV
Microbunch charge	30 pC
RMS* length	100 fs
Normalised emittance ($\epsilon_x \times \epsilon_y$)	$4.7 \times 6.5\,\pi$mm mrad
Repetition rate (max)	12.5 bunch trains/s

* RMS: root mean square

A train of laser pulses was generated using the optical system described in Reference [35]. At the start, a short laser pulse with a few tens of femtoseconds length was stretched to the picosecond level. As shown in Figure 4.2, the stretched pulse was split and recombined, and a sequence of spectrally chirped ps pulses with variable time separations were generated by pulse divider.

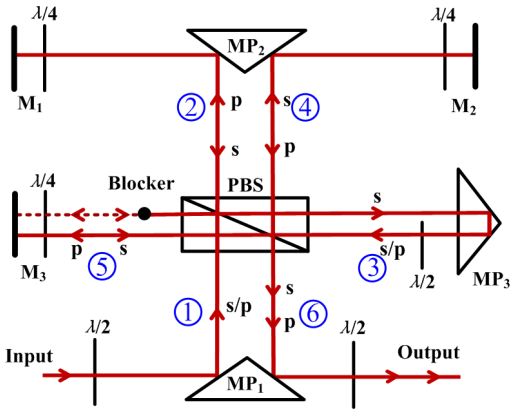


Figure 4.2: Schematic diagram of the laser splitting system which includes polarised beam splitter (PBS), prism mirrors MP_1, MP_2 and MP_3, motorised mirrors M_1 and M_2, fixed mirror M_3 and half-wave ($\lambda/2$) and quarter-wave ($\lambda/4$) retardation plates. The polarization state of laser is denoted as s and p, and s/p represents a mixed polarization [35].

The principle of the laser splitting system follows. In Figure 4.2, two linear polarizations defined in respect of E-field direction oriented perpendicular or parallel to the plane of paper are denoted as s or p, and s/p represents a mixed polarization state. The function of polarised beam splitter (PBS) is to transmit p-polarized light and reflect s-polarized light.

In the beginning, a pulse with s/p polarization state was produced (①). After passing the PBS, p-polarized light was transmitted and s-polarized light was reflected which was further absorbed by the Blocker. p-polarized light became s-polarized light after a quarter-

wave plate (②). Then the s-polarized light was reflected to prism mirrors MP_3 and its polarization state became s/p after a half-wave plate (③). Afterwards, p-polarized light was transmitted and s-polarized light was reflected after the PBS. Then s-polarized light became p-polarized light after a quarter-wave plate (④) and p-polarized light became s-polarized light after a quarter-wave plate (⑤). After this, the two micro-pulses combined into one pulse with a separation (⑥).

Afterwards, they were amplified up to 2 mJ per micro-pulse by the multi-pass Ti:Sa amplifier (Chirped Pulse Amplification technique) and recompressed to a few tens of femtoseconds. Finally the laser pulses were transported to the photocathode for the generation of an electron beam. In the experiments, a beam blocker was positioned in the path of laser shown in Figure 4.2. In this case only two laser pulses (instead of four) were generated. The relative time offset of the two pulses can be adjusted by the moving mirror M_2, which is two times the movable mirror displacement.

4.1.2 Variation of the microbunch separation

As shown in Figure 4.3, a train of electron microbunches can be emitted from a photocathode sequentially. The initial microbunch separation is determined by the time interval between the laser pulses Δt_0. This time interval leads to the injection of microbunches at different RF accelerating phases ($\phi_{01,2}$), which results in energy spread and variation of the microbunch separation Δt_1 from its initial value.

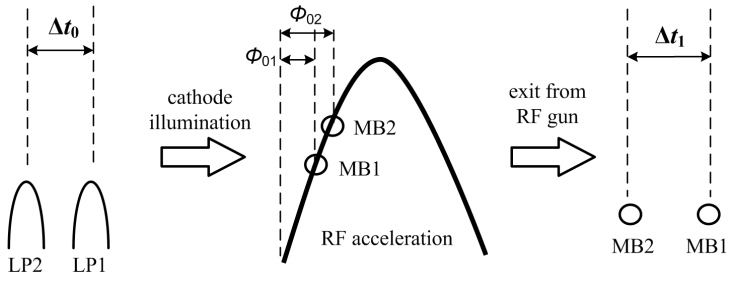


Figure 4.3: Schematic diagram of the generation and acceleration of two microbunches (MB1 and MB2) by illuminating the photocathode with two fs-long laser pulses (LP1 and LP2, with time interval Δt_0) in the presence of an external RF accelerating potential (not to scale).

To illustrate the dependence of final microbunch separation on the initial RF phases, an analytical model developed in Reference [67] was used. In the model, the microbunches were assumed to be point charges and the distance between two charges is defined as the microbunch separation. Assuming that the RF gun operates at a single mode, the accelerating field is a standing wave and omitting the transverse fields, the accelerating field E_z on the axis of the RF gun can be written as:

$$E_z(z, \phi_0) = E_0 \cos(kz) \sin(\omega t + \phi_0) \tag{4.1}$$

where E_0 is the accelerating field amplitude, z is the propagation distance of the point charge in the RF gun, ω is the operating angular frequency, $k = \omega/c$ is the wavenumber and ϕ_0 is the initial accelerating phase of the charge (in Figure 4.3) at the entrance of the RF gun. The dependence of the single electron energy on the coordinate z and the initial phase ϕ_0 is given by:

$$\frac{d\gamma}{dz} = \frac{eE_z(z, \phi_0)}{m_0 c^2} \tag{4.2}$$

where γ is the Lorentz factor of the electron.

The point charge is moving in the RF gun, the accelerating RF phase ϕ of the charge at a given time t and position z in the gun can be written as:

$$\phi = \omega t - kz + \phi_0 = k \int_0^z \left(\frac{\gamma(z', \phi_0)}{\sqrt{\gamma^2(z', \phi_0) - 1}} - 1\right) dz' + \phi_0 \tag{4.3}$$

The operating frequency of the RF gun at the KEK-LUCX facility is 2.856 GHz and the accelerating electric field amplitude E_0 is 80 MV/m. Based on the above analytical model, using the parameters given and conditions, such as Δt_0 and $\phi_{01,2}$, the Lorentz factor γ can be calculated at the exit of the accelerating region and its dependence on the initial RF phase ϕ_0 is shown in Figure 4.4.

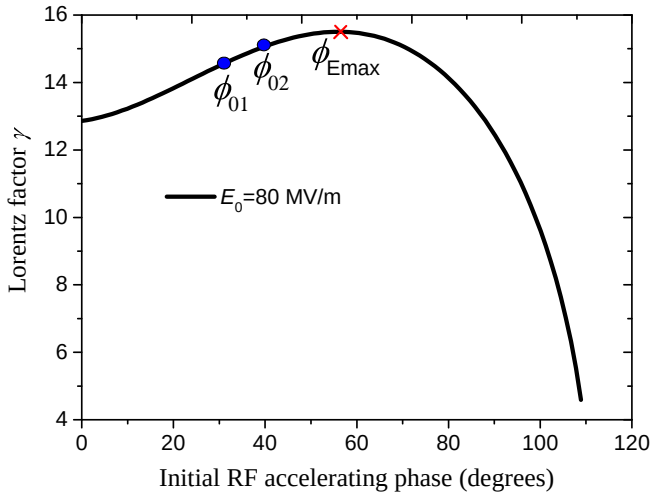


Figure 4.4: Lorentz factor γ of an electron at the exit of the accelerating region as a function of the initial RF phase ϕ_0 of the electron at the cathode surface.

It is assumed that the initial RF phases are ϕ_{01} and ϕ_{02} for the first and the second microbunch respectively ($\Delta\phi_0 = \phi_{02} - \phi_{01} > 0$). For an RF phase of ϕ_{02} smaller than the phase ϕ_{Emax}, where the beam energy reaches the maximum (Figure 4.4), the second microbunch experiences a larger accelerating potential, meaning that the transit time of the second microbunch through the accelerating region is shorter than that of the first microbunch. Therefore, the microbunch separation at the end of the accelerating region becomes smaller than the initial separation.

In Figure 4.5, the solid curve shows the final RF phase ϕ at the exit of the RF gun as a function of the initial phase ϕ_0 at the entrance. The figure indicates that the final phase ϕ doesn't have a linear dependence on the initial phase. The slope of the tangent line of the curve is one when the initial phase is equal to ϕ_{Emax}, meaning that the phase difference $\Delta\phi$ after acceleration is almost equal to the initial phase difference $\Delta\phi_0$ if the two microbunches are injected at ϕ_0 around ϕ_{Emax}. The relation between the microbunch separation Δt and the difference of the RF phase $\Delta\phi$ is given by $\Delta t = \Delta\phi/\omega$. Therefore, the microbunch separation is reduced (or increased) when the initial phase is less (or greater) than ϕ_{Emax}.

Considering these results, it is clear that there are several phenomena that could affect the microbunch separation, such as space charge effects, compression, or velocity bunching

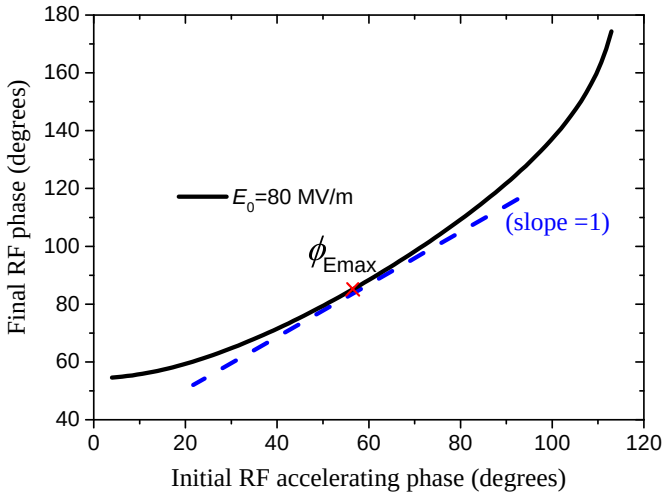


Figure 4.5: Final RF phase ϕ of an electron at the end of the accelerating region as a function of the initial RF phase ϕ_0 of the electron at the cathode surface. The dashed line indicates the tangent of the curve at initial RF phase of ϕ_{Emax}.

due to different initial RF phases of the microbunches, and the time jitter between laser pulses and RF accelerating potential. Any variation of the time interval between laser pulses and the RF phase (phase jitter) will lead to the acceleration of microbunches at different potentials and thus to the deviation of the microbunch separation from its initial value. In the following sections, a method to measure the microbunch separation is proposed and discussed.

4.1.3 Basis of the measurement of the microbunch separation

As discussed in Chapter 2, for a train of microbunches consisting of M identical microbunches with equal separation of Δt, the intensity of coherent radiation $I(\nu)$ generated at frequency ν can be given by:

$$\begin{aligned} I(\nu) &= M^2 I_1(\nu) G_M(\nu, \Delta t) \\ G_M(\nu, \Delta t) &= \frac{1}{M^2} \frac{\sin^2(M\pi\nu\Delta t)}{\sin^2(\pi\nu\Delta t)} \end{aligned} \tag{4.4}$$

where $I_1(\nu)$ is the radiation generated by a single microbunch, $G_M(\nu, \Delta t)$ is a normalised

function depending on the observation frequency ν and the separation of microbunches Δt. If the observation frequency is fixed at ν_0, $G_M(\nu_0, \Delta t)$ depends only on the separation of microbunches. In this case, any changes in the interval Δt between microbunches will lead to the variation of G_M and therefore the variation of the total radiation intensity. The function G_M will be referred as multi-bunch signal modulation (MBSM) function.

It will be shown in the following discussion that, the measurement was carried out at a wavelength significantly larger than the dimensions of a single microbunch. In this case, one can ignore the variation of the profile of the microbunch. Assuming that there are two identical microbunches, the MBSM function $G_M = G_2$ can be written as:

$$G_2(\nu_0, \Delta t) = \frac{1 + \cos(2\pi\nu_0\Delta t)}{2} \tag{4.5}$$

As shown in Figure 4.6, the variation of the separation between microbunches leads to variation of the intensity of the monochromatic signal. $G_2(\nu_0, \Delta t)$ has maxima and minima at the positions where $\nu_0\Delta t = n/2$ and n is an integer. By varying the microbunch separation, constructive and destructive interference of the signals from two microbunches appear, leading to the multi-bunch signal modulation.

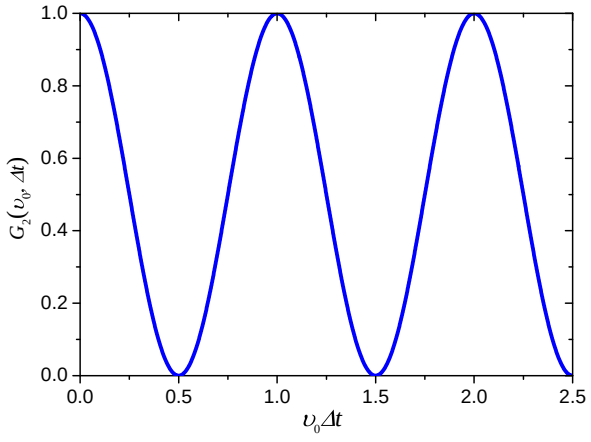


Figure 4.6: Dependence of $G_2(\nu_0, \Delta t)$ on the microbunch separation Δt between two microbunches at an observation frequency ν_0.

4.2 Experiments with two microbunches

4.2.1 Experimental setup

In the following, experiments carried out to measure the microbunch separation are presented. A schematic of the experimental setup is shown in Figure 4.7. Smith-Purcell radiation was generated when the electron beam passes above the aluminium grating positioned on a 5-axis mount in the chamber. The radiation was transmitted through the sapphire window and then collected by pair of off-axis parabolic mirrors, which were positioned to collect the radiation at 90 degrees (normal to the grating). A photograph of the Michelson interferometer system (the path that the radiation takes through is shown by red arrows) is shown in Figure 4.8. A Zero Bias Diode (ZBD) detector was positioned at the focus of a parabolic mirror to measure the radiation spectrum through the interferometric autocorrelation method.

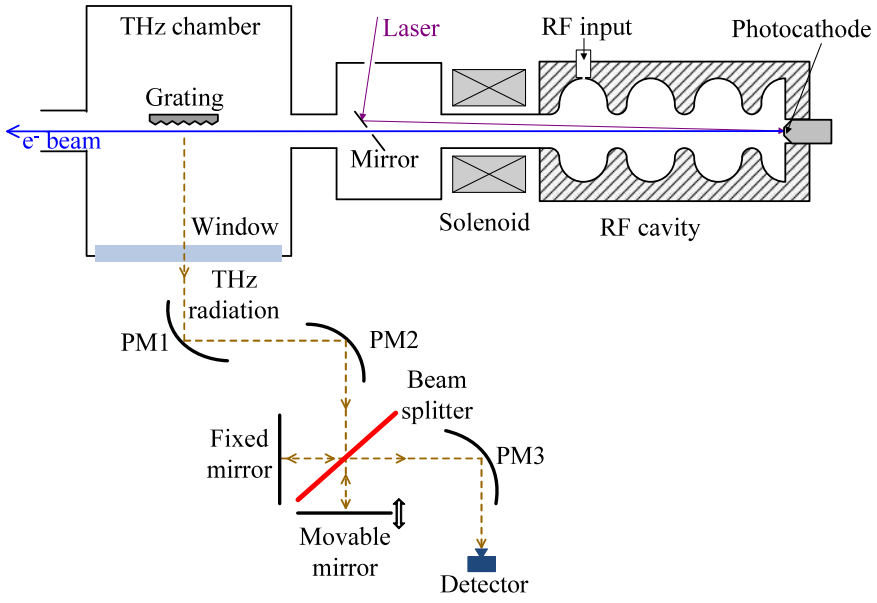


Figure 4.7: A schematic of experimental setup which includes the photocathode gun, 3.6-cell RF cavity, grating, sapphire window, Michelson interferometer, and detector.

The principle of the interferometric autocorrelation method follows. THz signal was split by a beam splitter in the interferometer (Figures 4.7 and 4.8) and then combined again to produce interference. By changing the position of the movable mirror, the radiation intensity

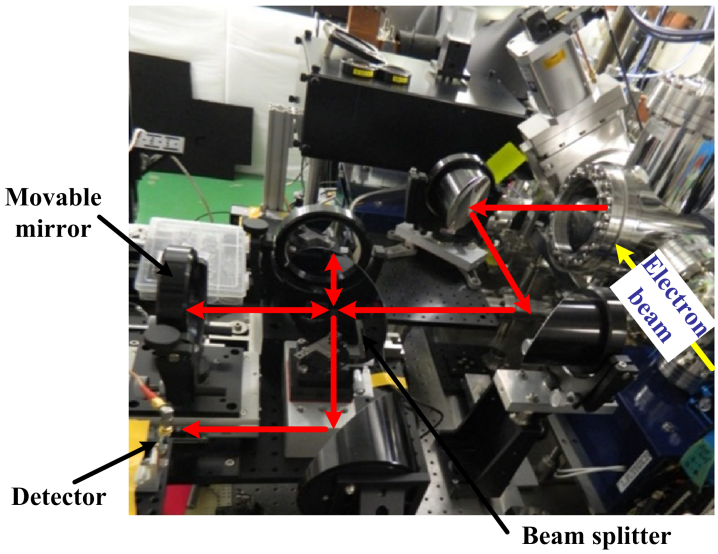


Figure 4.8: Photograph of the Michelson interferometer system (the path that the radiation takes through the Michelson interferometer is shown by red arrows).

collected by the detector varied. Recording the intensity variation versus optical path length gives us an interferogram. The radiation spectrum can be obtained by performing a Fourier transform of the measured interferogram. The following interferograms and spectra for cTR and cSPr were obtained by the same method.

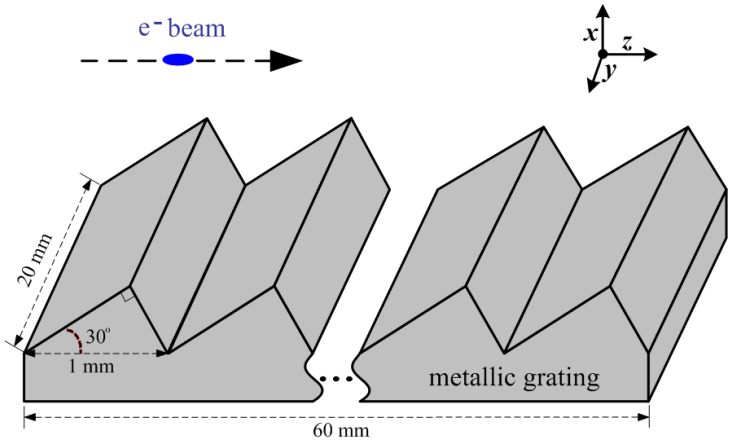


Figure 4.9: Schematic diagram of the grating with a sawtooth profile used at KEK-LUCX.

The grating was machined on one of the surfaces of an aluminium plate. The diagram of the grating used in the experiments is shown in Figure 4.9. The width of the grating was 20 mm, the length was 60 mm, and the period was 1 mm. The grating facet profile was sawtooth with a forward angle of 30 degrees. The direction of grating grooves was along the y coordinate and perpendicular to the motion direction of the bunch (in z direction). The

other side of the plate was kept smooth intentionally so that it could be used for the studies of coherent transition radiation generation. The grating position was controlled remotely from the control room. First, the plate was positioned on the rotating platform inside of the vacuum chamber. To generate coherent transition radiation, the electron beam intersected with the smooth side of the plate which was angled at 45 degrees. To generate cSPr, the plate was rotated so that the grating could face the electron beam (Figure 4.9).

4.2.2 Spectrum of cSPr

In order to calibrate the detectors, the transition radiation was measured first. Its use is conventional for the calibration of detectors as it has a broad spectrum and the measured spectrum is mainly determined by the properties of the detectors (given the beam parameters are fixed).

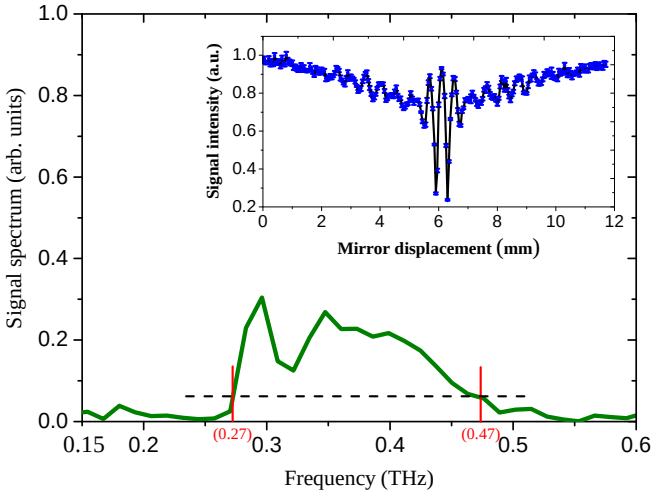


Figure 4.10: Normalised spectrum of the transition radiation signal generated by a single bunch (inset is a plot of the interferogram measured).

In the experiments, a Zero Bias Diode (ZBD) detector with a detection frequency range from 325 GHz to 500 GHz [68, 69] was used (the details of the detector can be found in Appendix D). The detector had a waveguide WR-2.2 (cut-off frequency of 268 GHz) acting as a low frequency filter and guiding the radiation to the metal-semiconductor junction region. The spectrum of the transition radiation generated by a single bunch is shown in

Figure 4.10. The insert is the interferogram measured. It is clear in Figure 4.10 that the detector can operate in the frequency ranges from 270 GHz to 470 GHz with a sharp rise in response at around 265 GHz.

When the metallic grating was moved close enough to the beam, cSPr was generated. The measurement of the radiation spectrum was taken to confirm the cSPr generated by a single bunch using the interferometer. As shown in Figure 4.11, cSPr was detected at a frequency of 300 GHz (λ=1 mm). Considering the grating period was 1 mm and the detector was positioned to collect the radiation at 90 degrees (normal to the grating), the measured frequency in Figure 4.11 is in excellent agreement with the dispersion relation of Smith-Purcell radiation in the far-field region.

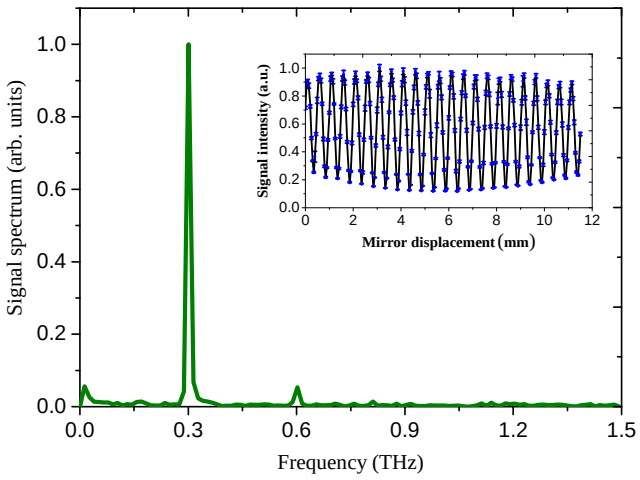


Figure 4.11: Normalised spectrum of the cSPr signal generated by a single bunch and measured at a detection angle of 90 degrees (inset is a plot of the interferogram measured).

Without changing the experimental setup, the experiments with two electron microbunches were carried out. The measurement of the spectrum was taken to confirm the cSPr generated by two microbunches. Same with the previous single bunch experiments, the spectrum had a peak at the frequency of 300 GHz when the mirrors were positioned to collect the signals at 90 degrees.

These preliminary set of experiments using the measurement of the radiation spectrum validated the performance of the ZBD detector, the generation of cSPr generated by a single

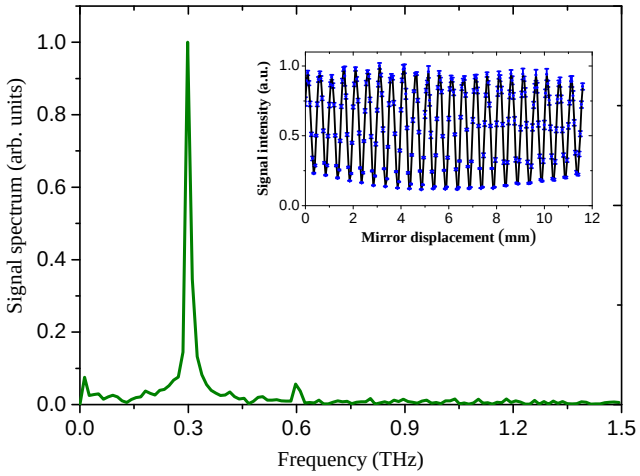


Figure 4.12: Normalised spectrum of the cSPr signal generated by two microbunches and measured at a detection angle of 90 degrees (inset is a plot of the interferogram measured).

and two microbunches, as well as confirming the operation and control of the Linac and the experimental setup.

4.2.3 Tuning the microbunch separation

After confirming the radiation frequency, the arms of the interferometer were kept fixed. The measurement of radiation intensity was carried out for different separations between laser pulses at a set of initial RF phases. At the same time, the laser pulses generated by the laser system were kept identical. The important feature of the laser system was that the relative separation of two laser pulses (output) could be varied from negative to positive continuously. This was achieved by varying the position of the mirror M_2 (Figure 4.2), which in turn varied the time delay between the pulses. When the separation was equal to zero, the two laser pulses merged into one pulse and a single bunch at the photocathode was generated.

An integrating current transformer (ICT) was used as a beam charge monitor at the KEK-LUCX beamline. The total charge of the two microbunches versus the position of the mirror M_2 for different initial RF phases was measured and is shown in Figure 4.13. It can

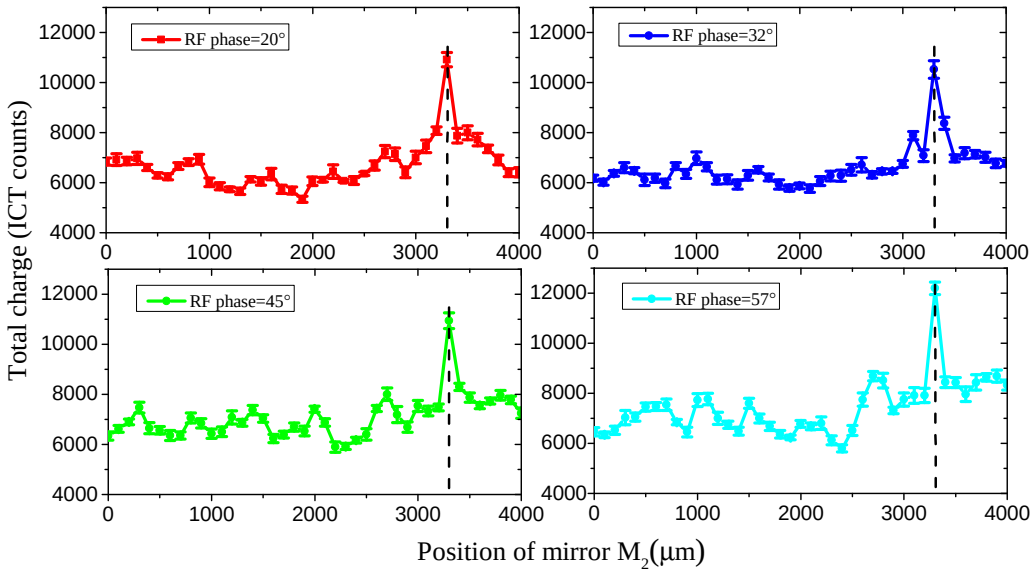


Figure 4.13: Total charge of the two microbunches measured (ICT count) for different RF phases ϕ_{RF}=[20°, 32°, 45°, 57°] as a function of the position of mirror M_2 shown in Figure 4.2.

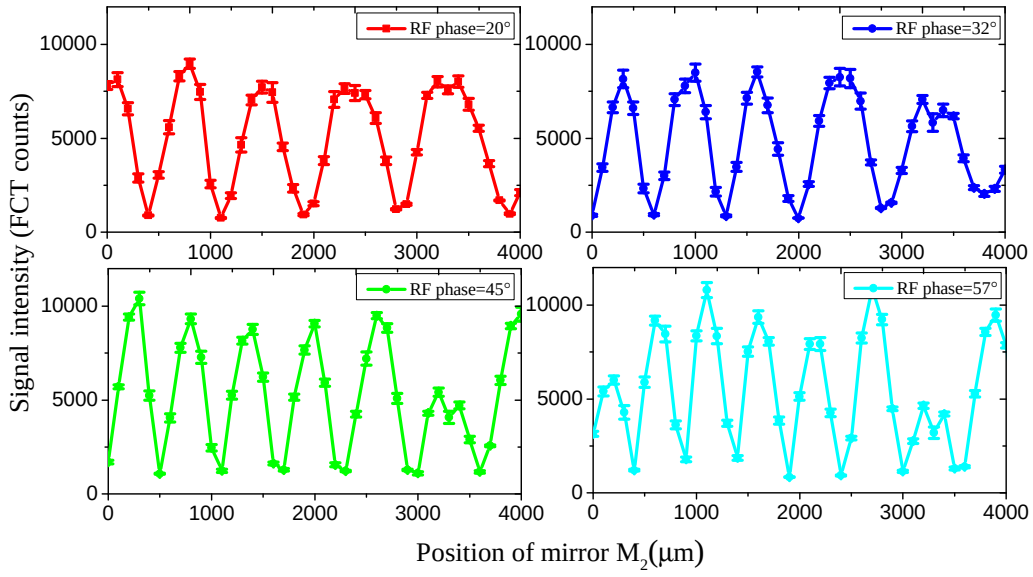


Figure 4.14: Smith-Purcell radiation intensity measured (FCT counts) at 90 degrees for different RF phases ϕ_{RF}=[20°, 32°, 45°, 57°] as a function of the position of mirror M_2 (each dot in the lines was averaged over 10 shoots).

be seen that the charge is almost constant over the scan range except at the position around 3300 μm (black dashed lines), which is the same for all four RF phases. It indicates that the separation of the two laser pulses becomes zero at this position (referred hereafter as 'reference position') and the two laser pulses overlap with each other after passing through the laser splitting system. Due to the nonlinear operating characteristic of the Ti:Sa amplifier, the output laser pulse became more intense, meaning that more charges were generated after the pulse illuminated the photocathode. This explains the peak of the total charge measured.

On the other hand, the large charge of the electron bunch (in case of the overlap) can cause stronger dispersion of the bunch due to the space charge effects and results in the increase in the energy spread of the bunch. This causes a slight variation of the transverse size due to solenoid focusing, which in turn affects the radiation intensity generated (see Figure 4.14). This reference position is used to calculate the laser pulse separation at the photocathode, which is also noted as the initial electron microbunch separation. For example, at the zero position of mirror M_2 as shown in Figure 4.13, the separation of the laser pulses was calculated to be 2×(3300-0) μm=6600 μm (22 ps in the unit of time).

Changing the time interval between two laser pulses, the separation between microbunches was varied and studies of MBSM function were carried out. As shown in Figure 4.14, the radiation intensity measured by the ZBD detector was indicated by the Fast Current Transformer (FCT) counts. It shows that the radiation intensity oscillates as a non-periodic function for all of the initial RF phases. The distances between two adjacent minima of the intensity measurement are also different for different initial RF phases. Taking an RF phase of 20° for example, the distances gradually increase from 700 μm to 900 μm during the scan, while the distances between minima are almost constant (500 μm) in case of the RF phase of 57°.

4.3 Microbunch separation measurement

In this section, based on the experimental data shown in Figures 4.13 and 4.14, a method of estimating the separation between two microbunches at the region of interest (in our case THz chamber) is discussed and the results are compared with analytical predictions.

4.3.1 Measurement of the separation based on experimental data

In the experiments, due to various reasons including sporadic laser intensity variation, the total charge may vary. To remove the influence of the charge variation, the radiation intensity of the Smith-Purcell signal (FCT counts) was normalised to the square of measured total charge (ICT counts). The normalised radiation intensity as a function of the initial microbunch separation (laser pulses separation defined at the cathode) is shown in Figure 4.15.

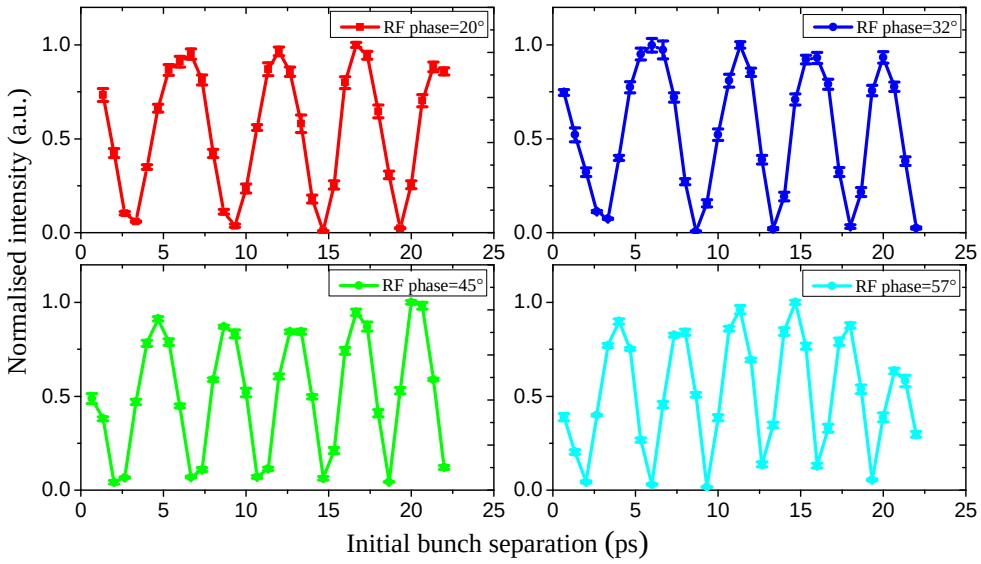


Figure 4.15: MBSM intensity measured at 90 degrees for a set of RF phases $\phi_{\mathrm{RF}} = [20°, 32°, 45°, 57°]$ and as a function of the initial microbunch separation varying from 0 to 22 ps (maximum intensity is normalised to one, bunch separation in the unit of time).

To demonstrate the principle of the measurement of microbunch separation and the validity of the method suggested, it was initially assumed (wrongly) that the microbunch

separation is conserved during the propagation, meaning that the microbunch separation at the target is the same as the initial microbunch separation at the photocathode. Using the oscillating function for two microbunches in Equation 4.5, the variation of the radiation intensity versus the initial microbunch separation can be calculated and the results are shown by the black dashed line in Figure 4.16. The solid line with error bars indicates the normalised intensity of the Smith-Purcell radiation measured at an RF phase of 20°. The difference between the dashed and solid lines shows that the microbunch separation at the point of measurement had changed during the propagation of the microbunches and that the initial assumption must be wrong.

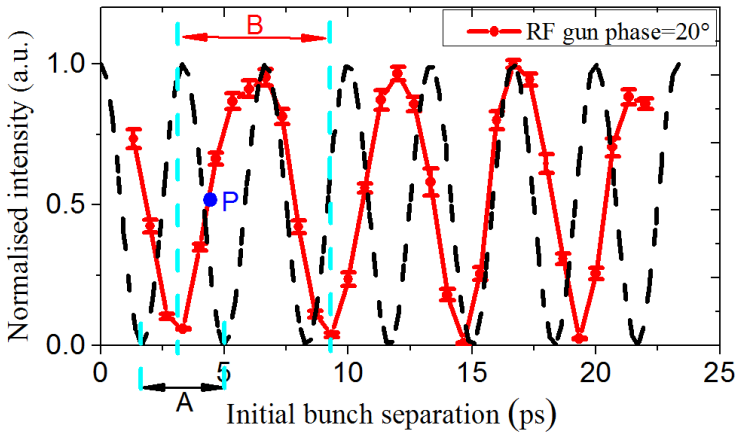


Figure 4.16: Intensity of the cSPr signal measured (solid line) and predicted (dashed line) showing the dependence of the radiation on the separation between the two microbunches for the initial RF phase $\phi_0 = 20°$.

To determine the microbunch separation using the measurement shown in Figure 4.15, recall that the radiation intensity is only determined by the microbunch separation Δt when the observation frequency is fixed. In the experiments the radiation frequency f_0 is 300 GHz. For each point on the solid curve in Figure 4.16 with normalised intensity I, the real microbunch separation Δt was obtained by solving the equation below:

$$G_2(f_0, \Delta t) - I = 0 \tag{4.6}$$

As G_2 is a periodic function, the value of Δt can only be defined if calibration is carried out. For example, in the region B in Figure 4.16, the first oscillation period can be seen (red line). At point P in region B, the value of the normalised intensity I is 0.5. Letting $G_2(f_0, \Delta t)$=0.5, we can get Δt=$0.25T_0$, $0.75T_0$, $1.25T_0$, ..., $(n/2 - 0.25)T_0$ ($T_0 = 1/f_0$, n is positive integer). In this case we know that point P is in the first half cycle of the first oscillation period and the corresponding microbunch separation is between $0.5T_0$ and T_0. Therefore, we can get the real microbunch separation for point P, which is $0.75T_0$.

Using the same method, the microbunch separations at other regions along the solid line could be obtained. Careful calibration and identification of the zero point (microbunch separation is 0) is required in order to obtain the order of the oscillation period (n) and the position of the measurement point within a period, such as in the first or the second half cycle. For the n_{th} oscillation period, the corresponding microbunch separation Δt is between $(n - 0.5)T_0$ and nT_0 for the first half cycle, and between nT_0 and $(n + 0.5)T_0$ for the second half cycle.

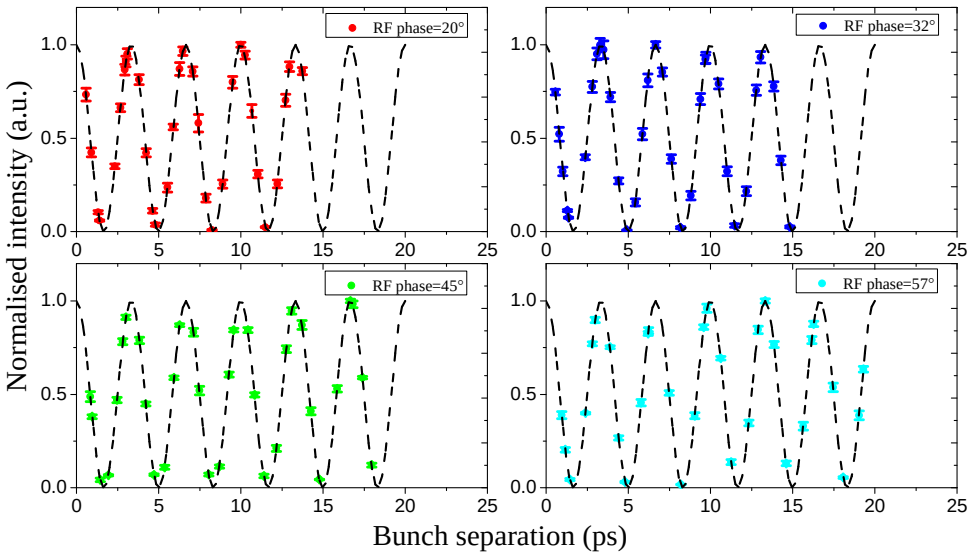


Figure 4.17: Microbunch separations calculated from measurement (dots with error bars). The dashed line indicates the normalised intensity from two identical microbunches calculated under the assumption that the separation between microbunches is constant and only defined by the time interval between laser pulses.

The measured radiation intensity as a function of the real microbunch separation is shown

in Figure 4.17 for four different RF phases. The dashed lines are the predicted results. At this stage, no assumption was made about how the microbunches were generated and their dynamics prior to the measurement. In the following section, the separation between microbunches will be further studied and the comparison between analytical predictions and experimental measurement will be made.

4.3.2 Comparison of measurement with analytical predictions

Taking into account Equations 4.1 - 4.3, the separation between microbunches at the exit of RF gun can be calculated as $\Delta t_{\mathrm{RF}} = \Delta\phi/\omega_{\mathrm{RF}}$ where ω_{RF} is the operating frequency of the RF gun. There are no other accelerating sections operating in the beamline at the KEK-LUCX facility during the experiments. The transit time of the bunch through the distance L along the beamline is $t_{\mathrm{pipe}} = \frac{L}{c}\frac{\gamma(z,\phi_0)}{\sqrt{\gamma^2(z,\phi_0)-1}}$. Thus, the microbunch separation at a distance L away from RF gun exit is $\Delta t = \Delta t_{\mathrm{RF}} + \Delta t_{\mathrm{pipe}}$.

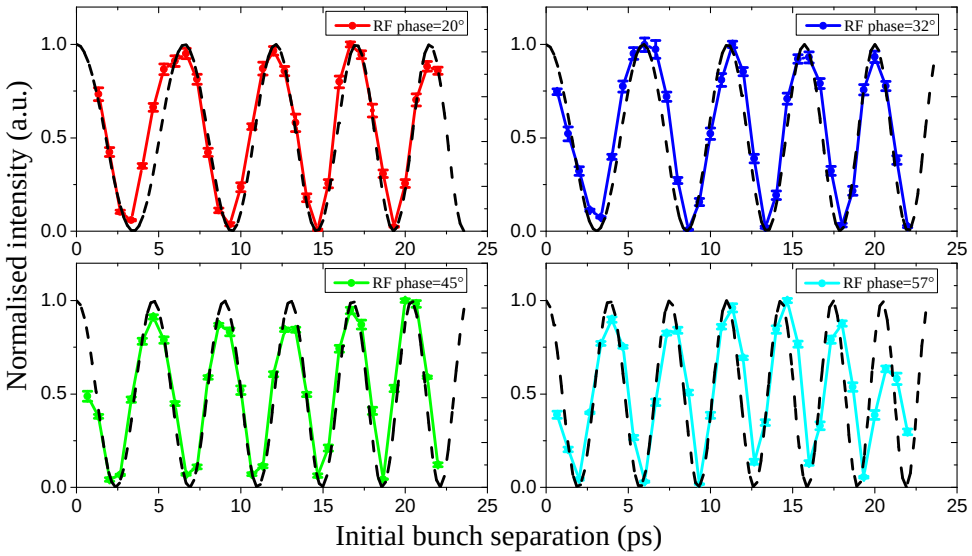


Figure 4.18: Comparison of the normalised intensity of the cSPr signal measured and predicted after the corrections of the microbunch separation. Solid lines with error bars: measurement; dashed lines: predictions from analytical model using corrected value of the microbunch separation.

Using the microbunch separation Δt predicted by the model, the radiation intensity can

be obtained. It should be noted that the real microbunch separation has already been evaluated based on the experimental data via the analysis of the variation of coherent radiation intensity. The comparison of the normalised intensity from measurement and analytical predictions at different RF phases is shown in Figure 4.18.

The RF phase for the first microbunch ϕ_1 was set at 20°, 32°, 45°, and 57°. In all graphs good agreement between experimental measurement and analytical predictions is observed. The agreement also illustrates the validity of this method of monitoring the microbunch separation.

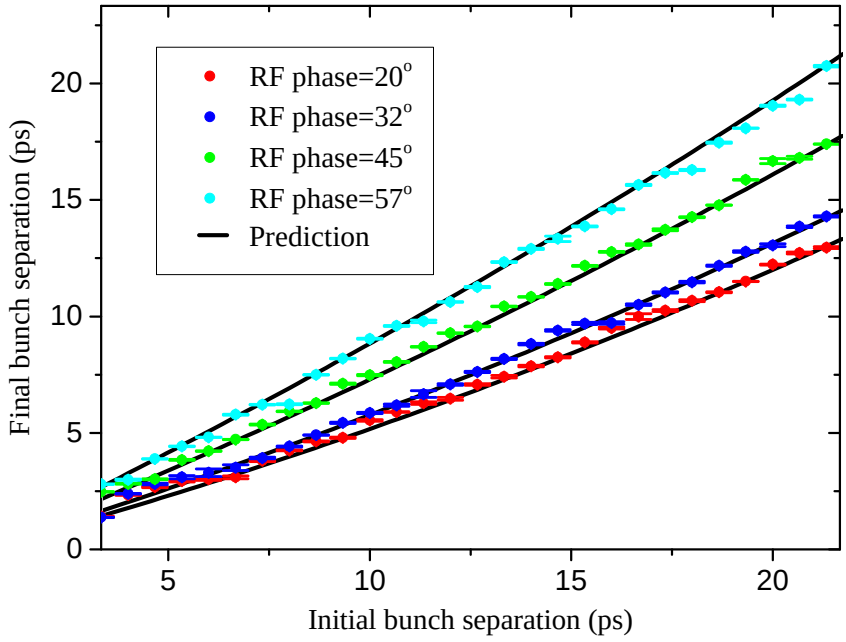


Figure 4.19: Dependence of the final microbunch separation on the initial separation between microbunches for $\phi_{\mathrm{RF}} = [20°, 32°, 45°, 57°]$. Dots with the error bars correspond to the microbunch separations from measurement and solid black lines correspond to the predicted separations.

The direct comparison of the microbunch separation from analytical predictions and experimental measurement is shown in Figure 4.19, which illustrates the dependence of the microbunch separation on the initial separation between the microbunches for the set of RF phases. Each solid line in Figure 4.19 corresponds to a specific ϕ_{RF} of the accelerating field, as indicated on the graph. The error of the measured microbunch separation comes from

the variation of collected intensity from shot to shot in the experiments. The average error of the normalised measured intensity is 6% with the maximum error of 11.4%. The average error for the measured microbunch separation is less than 1% with the maximum error of 4.9%.

To simplify the analysis, the space charge effects were not considered. The assumption is reasonable for this set of experiments. This effect should be taken into account if we want to make the model more accurate. However, the space charge effects will not affect the experimental measurement of the separation as long as it doesn't result in a significant variation of the bunch dimensions and bunch-bunch separation while the bunches are passing over the grating.

4.4 Discussion

At present, there are many techniques to study the longitudinal bunch profile (the information of the microbunch separation is included in the case of trains), including the use of diffraction radiation and transverse deflecting cavities. The first requires extra spectrometers while the latter, although single-shot, is a destructive method. The measurement of the autocorrelation function of the transition radiation generated by a beam [24, 38, 70] is also used to identify the microbunch separation. This method is destructive and requires multi-shot measurements. The diagnostic method proposed and developed here is based on the analysis of cSPr and has the potential to provide non-destructive single-shot monitoring of the separation between microbunches. This method is independent of the way the microbunches are generated. It could be potentially useful for providing feedback to control the separation between fs-long microbunches in such applications as: stabilisation of the generation of THz radiation generated by a train of microbunches and control of the relative position of the witness bunch to the driver bunch in the wakefield acceleration process.

There are, however, many problems and challenges to be solved, which include the uncertainty of a single frequency measurement, different charge distributions, and the extension

of the diagnostic method to a train of microbunches with more than two microbunches.

4.4.1 Multiple-frequency measurements

It is worth noting that if a single-frequency measurement is applied as described above, there is a limitation associated with the non-uniqueness of the oscillating MBSM function G_M which arises from the fact that a single value of this function corresponds to many values of the interval between the microbunches. In our experimental system, we know the reference point of zero microbunch separation due to our ability to adjust the time interval between laser pulses continuously. But in the general case, this information may not be always available.

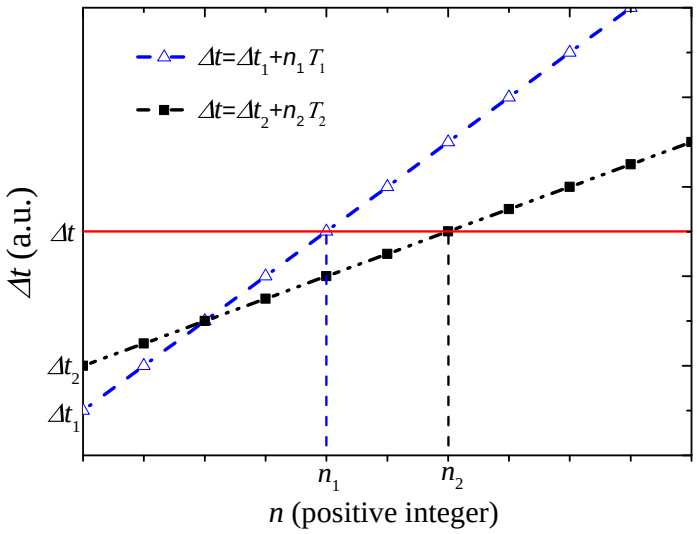


Figure 4.20: Multi-frequency measurements to identify the microbunch separation.

The problem of the non-uniqueness of the oscillating MBSM function is a well-known problem and it can be resolved by measuring G_M at two frequencies [71, 72]. The basic principle is as follows. For a two-bunch system with the microbunch separation Δt, assuming the normalised radiation intensity is I_1 at an observation frequency f_1 and is I_2 at an observation frequency f_2. Using Equation 4.6, we have:

$$\begin{aligned} G_2(f_1, \Delta t) - I_1 = 0 \\ G_2(f_2, \Delta t) - I_2 = 0 \end{aligned} \tag{4.7}$$

The microbunch separation Δt can be obtained at two frequencies as follows:

$$\begin{aligned} \Delta t = \Delta t_1 + n_1 T_1 \\ \Delta t = \Delta t_2 + n_2 T_2 \end{aligned} \tag{4.8}$$

where n_1 and n_2 are both positive integer, $T_1 = 1/f_1$, and $T_2 = 1/f_2$. As shown in Figure 4.20, the integer property of n_1 and n_2 ensures the unique solution of the microbunch separation Δt. Otherwise, there is no solution if either of them is not a positive integer.

Such a measurement at a second frequency can be performed using the same grating but with a second detector positioned at a different observation angle [29, 30]. The second measurement will provide a second intensity measurement, allowing the determination of the absolute microbunch separation over a larger unambiguous range.

4.4.2 Analysis for two different bunches

In a real experiment, the two microbunches may not be identical. For example, the shape of microbunches may be different or the charge distribution is non-equal. For coherent radiation generation, the observation wavelength can be selected to be much longer than the dimensions of a single microbunch and one can ignore the difference in the bunch shape. However, the difference of the charge in the two microbunches can significantly change the measurement. The effect of the non-uniformity of the bunch charge distribution on the measurement of the intensity is discussed below.

To simplify the analysis, it is assumed that the charge distribution of the beam within the two microbunches is given by:

$$n(t) = n_0 \left[\exp(-\frac{t^2}{2\sigma^2}) + \eta \exp(-\frac{(t-\Delta t)^2}{2\sigma^2}) \right] \tag{4.9}$$

where n_0 is the normalised density, σ is the longitudinal length of each Gaussian microbunch, η is the charge ratio between the first and the second microbunch, and Δt is the microbunch separation.

In this case, the expression for $|F(\nu)|^2$ can be written as:

$$|F(\nu)|^2 = \exp[-(2\pi\nu\sigma)^2] \frac{1+\eta^2+2\eta\cos(2\pi\nu\Delta t)}{(\eta+1)^2} \tag{4.10}$$

and the MBSM function G_2 becomes:

$$G_2(\nu, \Delta t) = \frac{1+\eta^2+2\eta\cos(2\pi\nu\Delta t)}{(\eta+1)^2} \tag{4.11}$$

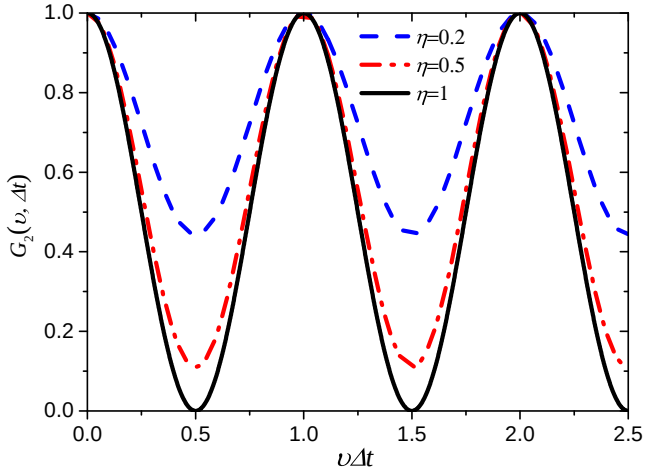


Figure 4.21: Dependence of $G_2(\nu, \Delta t)$ on the microbunch separation Δt between two microbunches having different distributions of charges, at a given frequency ν.

It is shown in Figure 4.21 that G_2 as a function of the microbunch separation and observation frequency. It is clear from the figure that, for uniform charge distribution ($\eta = 1$), the minimum of the radiation intensity from two microbunches is zero (G_2=0), meaning the interference of the radiation signals from each microbunch can be totally destructive for

certain microbunch separations. For two different charge distribution, the interference will never become totally destructive and the minimum of G_2 is no longer zero, which means the minimum radiation intensity is not zero.

A visibility function $\Gamma = (I_{\max} - I_{\min})/(I_{\max} + I_{\min})$ can be introduced to monitor the charge distribution, where $I_{\max}$ and $I_{\min}$ are the maximal and minimal values of the radiation intensity respectively. At a fixed frequency, $I_{\max} = \frac{1+\eta^2+2\eta}{(\eta+1)^2} = 1$, $I_{\min} = \frac{(\eta-1)^2}{(\eta+1)^2}$. The visibility function becomes:

$$\Gamma = \frac{2\eta}{1+\eta^2} \tag{4.12}$$

Once Γ ($0 \leq \Gamma \leq 1$) is obtained from the experiment, the charge ratio η can be calculated from Equation 4.12, which is $\eta = (1 - \sqrt{1-\Gamma^2})/\Gamma$. If $\Gamma = 1$, the microbunches have equal charges with the charge ratio $\eta = 1$. Otherwise, the ratio of the charges of microbunches is not one. For small $\Gamma \ll 1$, $\eta \approx \Gamma$.

4.4.3 Possibilities for trains with more microbunches

Although the results presented above were demonstrated for the case of two microbunches, this approach is applicable to monitor the periodicity of charged microbunch trains with microbunch number over two. As discussed before, the radiation spectrum becomes narrower at around the microbunch frequency when increasing the number of microbunches. Another limiting factor is that the separations between microbunches may not be uniform in the train. In this case, only the average microbunch periodicity can be measured.

4.5 Summary

To conclude, the generation of a train of microbunches using the laser illumination of a photocathode was discussed. Based on the experiments carried out at the KEK-LUCX facility,

I developed a diagnostic method to determine the microbunch separation by analysing the cSPr generated by microbunch trains. I proved that, by measuring the variation of the radiation intensity, one can determine the separation between microbunches. Comparing with analytical predictions, the averaged error for the measured microbunch separation was less than 1% with the maximum error of 4.9%. The measured results agree well with theoretical predictions. Further improvements in the measurement of the two-bunch system were discussed. The challenges of applying this method to trains with more than two microbunches were also discussed.

Chapter 5

THz radiation generated by microbunch trains with tunable periodicities

This chapter describes experiments carried out at the TTX facility to investigate the THz radiation generated by a single electron bunch and a train of microbunches. Coherent Smith-Purcell radiation (cSPr) generated by a single bunch is investigated and properties including the degree of polarization and the beam-grating coupling efficiency are studied. The widths of the spectral lines of coherent transition radiation (cTR) and cSPr generated by microbunch trains with variable periodicities are measured and compared. The effect of the microbunching of electron bunches on the distribution of the radiation intensity is studied. Some suggestions for future experiments are discussed.

5.1 An introduction to the TTX facility

The Tsinghua Thomson Scattering X-ray Source (TTX) is an accelerator facility dedicated to the investigation of different radiation generation mechanisms using electron beams. The spectrum of radiation ranges from X-ray to THz. A schematic layout of the TTX facility is

shown in Figure 5.1.

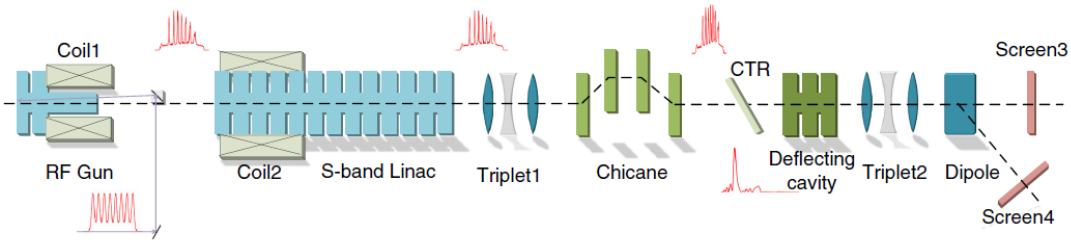


Figure 5.1: Schematic layout of the beamline for the generation of microbunch trains at the TTX facility [25].

By illuminating a 1.6-cell photocathode RF gun with a single UV laser pulse or a series of modulated pulses (energy up to mJ), a single bunch or a train of electron microbunches with energy of around 5 MeV and charge from a few pC up to l nC are emitted from RF gun respectively. The electron beam is then accelerated up to 45 MeV after a 3 m S-band travelling wave linear accelerating section. The beam energy can be adjusted by changing the accelerating phase. Bunch lengths varying from a few tens of femtosecond to a few picosecond can be achieved through the compression process in the electromagnetic chicane. Along the beamline there are two sets of solenoids, these are positioned at the photocathode and in the accelerating section. Additionally, two sets of triplets are used for the beam transverse focusing. A magnetic dipole is used to measure the energy of beam.

Unlike the laser splitting system used at the KEK-LUCX facility, birefringence in a crystal has been used to generate a train of modulated laser pulses at TTX. The basic principle follows. A linearly polarised light is normally incident on the surface of a birefringent alpha barium borate (α-BBO) crystal. The angle between the polarization direction of the incoming light and the optic axis of the crystal is 45°. The incident light can be resolved into two linearly polarised waves with polarization directions along the optic axis (extraordinary ray) and perpendicular to the optic axis (ordinary ray). After propagating a length of Δl in the crystal, the relative retardation Δt between the two orthogonal rays is given by $\Delta t = (n_{\mathrm{o}} - n_{\mathrm{e}})\Delta l/c$ where n_{o} and n_{e} are the refractive index of the ordinary and extraordinary ray, respectively and c is the speed of light in vacuum.

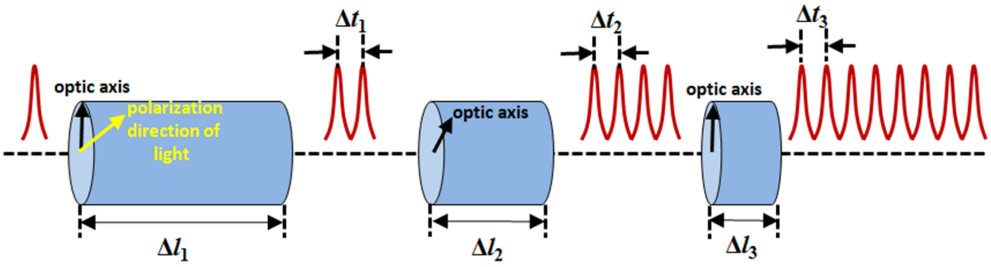


Figure 5.2: A schematic of the laser bunching system at the TTX facility.

Instead of one piece of crystal, a series of crystals can be positioned in the path of light to generate a train of pulses with a uniform separation. To achieve this, it is required that the relative angle between the optic axis of two adjacent crystals is 45° and the thickness of the previous crystal is two times that of the next one. By stacking three α-BBO crystals, a train of eight pulses with a uniform separation can be produced from one long pulse. A schematic of this process is shown in Figure 5.2, where $\Delta l_1 = 2\Delta l_1 = 4\Delta l_3$.

As mentioned in the introduction, the initial modulated electron beam emitted from the surface of the photocathode undergoes evolution due to the longitudinal space charge force. A train of microbunches (up to 7 microbunches) with tunable microbunch periodicities range from 0.68 ps to 1.41 ps were generated at TTX for this experiment.

5.2 Experiments with a single bunch

5.2.1 Experimental setup

A schematic of the experimental setup at TTX is shown in Figure 5.3. There are two sections in the beamline where THz radiation was generated. One is for the production of cTR and the other is for the generation of cSPr in the THz chamber. A movable aluminium target was positioned just after the magnetic chicane in the beamline. cTR was generated at TTX when the electron beam collided with the aluminium target positioned in the beamline. A Michelson interferometer system, shown in Figure 5.4, was used to measure the radiation

spectrum of the emitted cTR. The aluminium target can be retracted remotely, so the beam can be delivered downstream for other purposes while the accelerator is operational.

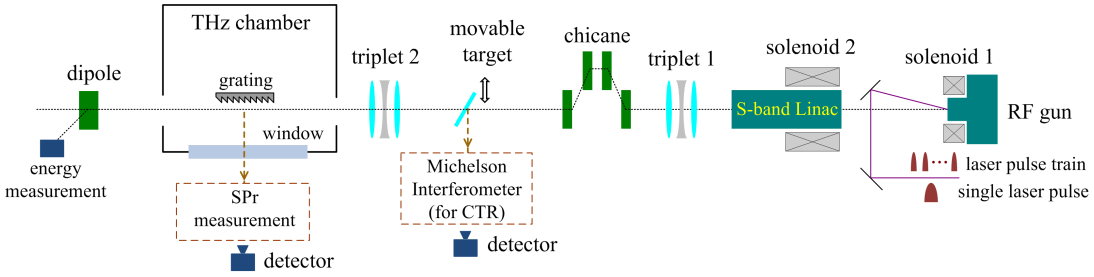


Figure 5.3: A schematic of experimental setup at TTX (not to scale).

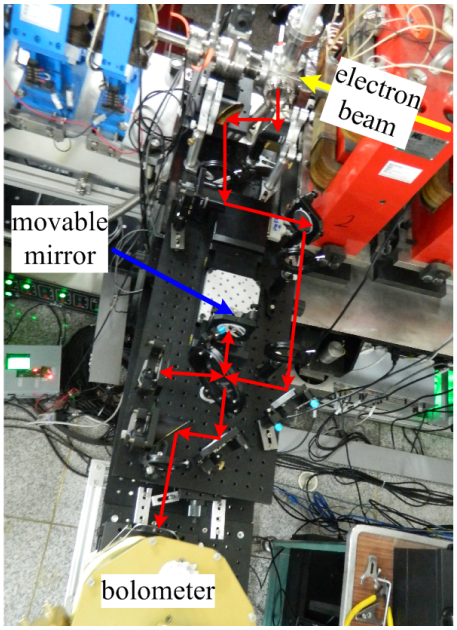


Figure 5.4: Photograph of the Michelson interferometer system (the path that the radiation takes through the Michelson interferometer is shown by red arrows).

As shown in Figure 5.5, a copper grating was mounted on a motion stage and positioned inside of the THz chamber (as shown in the experimental schematic in Figure 5.3). This THz chamber has a quartz vacuum window and was newly installed for the experiments carried out in August 2018. The diameter of the quartz window was 100 mm. The distance between the THz chamber and the cTR target was around 2 m. The length and width of the grating were 110 mm and 10 mm, respectively. The distance from the centre of the beam and the quartz window was around 50 mm. When the grating was moved close enough to the beam, cSPr was generated when the electron beam passed above the grating. The radiation was transmitted through the quartz window for measurement. For both measurements (cTR

and cSPr), a cryogenic bolometer (model No: LN-6/C) made by Infrared laboratories [73] was used as detector. The bolometer was housed in a liquid helium dewar with a liquid nitrogen cooled radiation shield. The radiation was collected by a Winston cone [74] with a vacuum-sealed wedged window in front of it. The operating frequency of the bolometer is from 150 GHz to 20 THz.

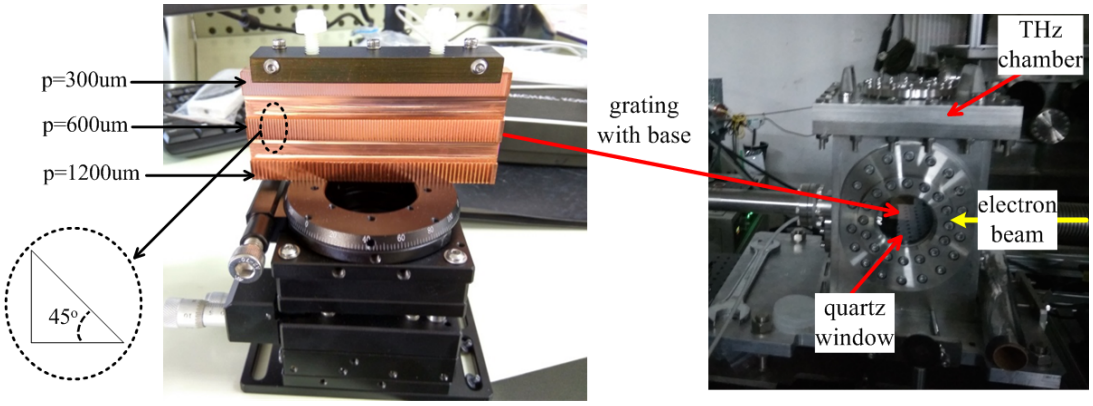


Figure 5.5: Photograph of the THz chamber and the sawtooth grating.

In the experiments, only the sawtooth grating with a period of 600 μm (Figure 5.5) was used, due to the limited experimental time. Therefore, all the measurements from the experiments carried out in August 2018 were based on this grating.

5.2.2 Confirming cSPr from a single bunch

Initially, experiments were carried out in order to observe cSPr from a single electron bunch. The average energy of the single bunch generated at TTX was around 30 MeV. The average charge of the beam was almost 400 pC. As during the experiments at KEK-LUCX, a Michelson interferometer was used to measure the spectrum of cSPr through the interferometric autocorrelation method.

As shown in Figure 5.6, the main peak of the spectrum, observed at a detector angular position of 90 degrees, is at 0.507 THz, with clear harmonics at 1.01 THz and 1.52 THz. Considering the uncertainty in the position of the detector, the frequencies measured agree well with values calculated using the dispersion relation (Equation 2.1) which calculates the first harmonic to be at 0.5 THz. The main reason for the measurement of the second

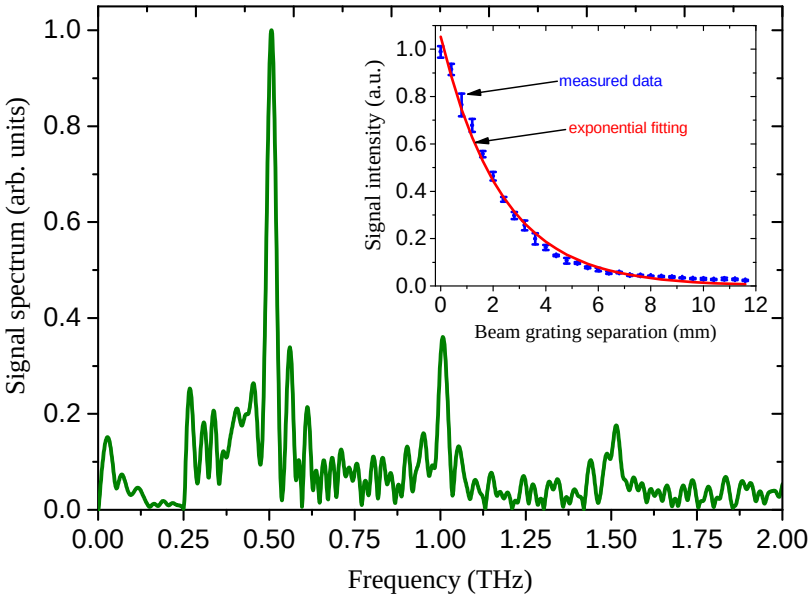


Figure 5.6: Normalised spectrum of the cSPr signal generated by a single bunch and measured at a detector angular position of 90 degrees (inset shows the dependence of intensity on the beam grating separation).

and the third harmonics in the experimental data is that the single bunch was compressed longitudinally by the chicane to around several hundred fs. The bunch form factor is not negligible in this case even at high frequencies, though the measured intensity of the high harmonics was much smaller than that of the first harmonic.

Moving the grating towards the beam, the dependence of the radiation intensity on the beam grating separation x_0 was obtained. As shown in the inset (Figure 5.6), the dotted line with error bars shows the measurement, while the solid line is the exponential fit, obtained by the function $\exp(-\alpha x_0)$ with coefficient $\alpha = 0.43 \pm 0.021$ (with 95% confidence bounds). According to Equation 2.3 and using the experimental parameters: an observation frequency of 0.5 THz, a beam energy of 30 MeV, and a detector position θ of 90 degrees and ϕ of 0, the coefficient should be 0.35, which is consistent with the measured value.

Recently it was proposed to perform single-shot measurement of beam profile using cSPr. As cSPr is highly polarised from theoretical calculations, it is possible to eliminate background radiation (normally not or low polarised) from the interested cSPr signal [75]. In the

following, experiments have been done to study the polarization of cSPr.

The polarization of cSPr was measured at the angular position of 90 degrees. A wire grid polariser manufactured by the PureWavePolarizers [76], shown in Figure 5.7, was mounted on a rotating stage and positioned in front of the bolometer (without the Michelson interferometer in the optical path). The polariser consists of a parallel array of fine tungsten wires that are placed in a plane. The incident radiation with polarisation direction parallel to the wire grid array is reflected and perpendicular to it is transmitted. The polariser was initially positioned with its wires parallel to the direction of electron bunch. A Waveguide Array Plate (WAP) filter (Figure 5.7) was also used in this experiment to remove the low frequency and any additional radiation not due to the cSPr signal. In general, WAP filters are made from a metal plate perforated with a periodic arrangement of holes. WAP filters are high pass filters and their cut-off frequencies can be adjusted by changing the size or the arrangement of holes. The cut-off frequency of the WAP filter used in our experiment was at around 300 GHz [77].

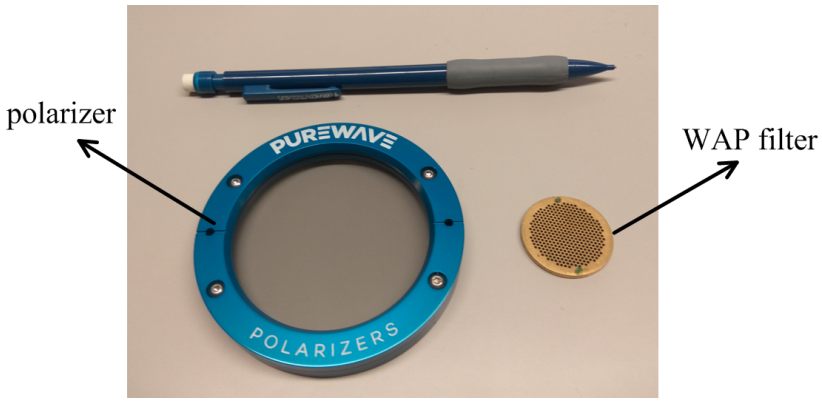


Figure 5.7: Photograph of the wire grid polariser (left) and the WAP filter (right) used in the experiment.

Rotating the polariser through 360 degrees and measuring every 5 degrees, the dependence of the radiation intensity on the rotation angle was obtained and is shown in Figure 5.8. The solid line was measured without any filter in the optical path and the dashed line was obtained by placing the WAP filter in front of the bolometer. The variation of the intensity of the radiation generated is clear when changing the rotation angle. The degree of polarization of the radiation was obtained by calculating $(I_{\max} - I_{\min})/(I_{\max} + I_{\min})$ where

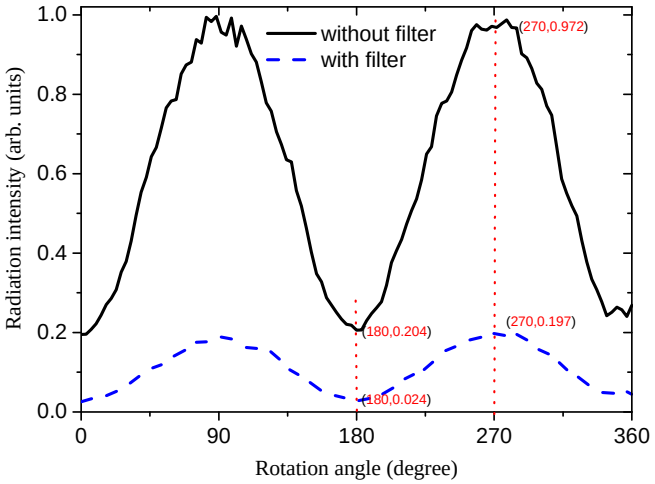


Figure 5.8: Radiation intensity versus the angle of the rotation of the polariser with and without a WAP filter in front of the detector.

$I_{\max}$ and $I_{\min}$ are the maximum and the minimum radiation intensity measured during the rotation of the polariser. The degree of polarization is calculated to be 65.3% without filter and 78.3% with the WAP filter. Hence the cSPr at 90 degrees is highly polarised. According to the surface current model (described in Chapter 2), the polarization degree could be up to 90%. The experimental result is reasonable agreed with theoretical calculation.

5.3 Experiments with microbunch trains

5.3.1 cTR from microbunch trains

Experiments have also been carried out using a train of microbunches. By shining a modulated laser pulse train on the photocathode, a long electron beam (with charge approximately of 400 pC) with intensity modulation was produced. Changing the phase of the RF gun leads to the compression or stretching of the overall bunch due to the velocity bunching, which means that the periodicity of microbunches at the exit of the RF gun can be varied [25]. This modulation can be 'frozen' by applying acceleration in the downstream Linac, where the beam energy was increased from 5 MeV to up around 45 MeV. A typical temporal profile

of the microbunch trains after the Linac is shown in Figure 5.9. The transverse beam size was around 200 μm. The number of microbunches was reduced from 8 to 7 due to the strong non-linear longitudinal space charge effects which caused the first two microbunches in the train to merge into one.

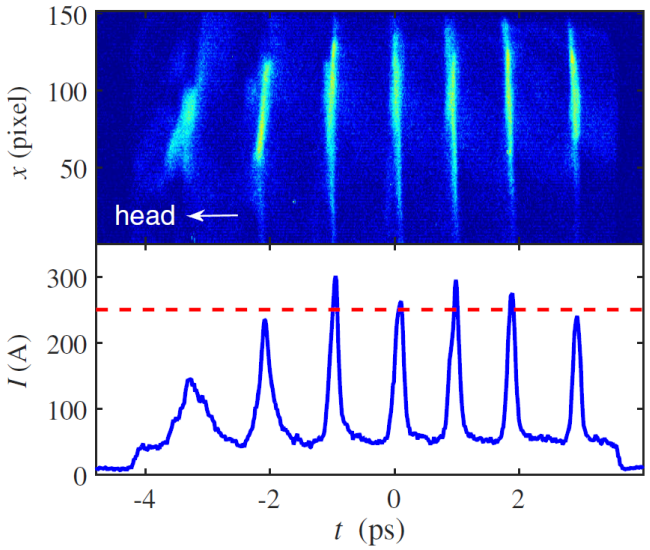


Figure 5.9: Typical temporal profile of the microbunched beam at the TTX facility (top: measured longitudinal distribution, bottom: projected density profile) [25].

The periodicity of microbunches was measured using cTR. The principle follows. The spectrum of the cTR generated by a single short electron bunch is broadband (up to few THz). Increasing the number of microbunches leads to the narrowing of the bandwidth of radiation and most of the signals localise at the frequency of microbunch trains. By positioning the target in the beamline, cTR was generated and was used to measure the average microbunch periodicity through the Michelson interferometer system shown in Figure 5.4. A typical interferogram and the spectrum of the cTR produced by microbunch trains at an RF gun phase of 40° are shown in Figure 5.10. The central frequency of the spectrum is 0.95 THz, which corresponds to the microbunch periodicity of 1.05 ps.

Changing the RF gun phase from 55° to 20°, the periodicity of the resulting train of microbunches was varied. The normalised spectra of the cTR signal generated by these microbunches are shown in Figure 5.11. It is clear that microbunch trains with tunable

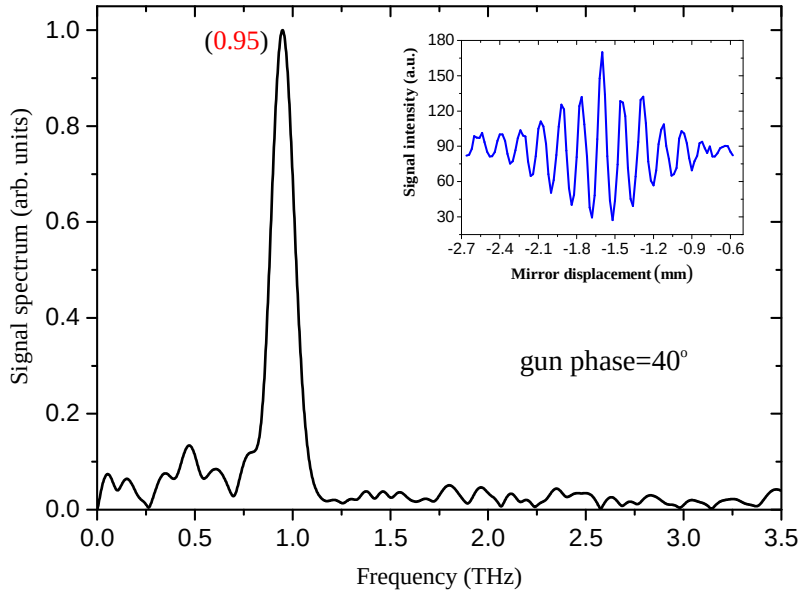


Figure 5.10: Typical spectrum of the cTR signal generated by a train of microbunches at an RF gun phase of 40° and measured using the Michelson interferometer (inset is a plot of the interferogram measured).

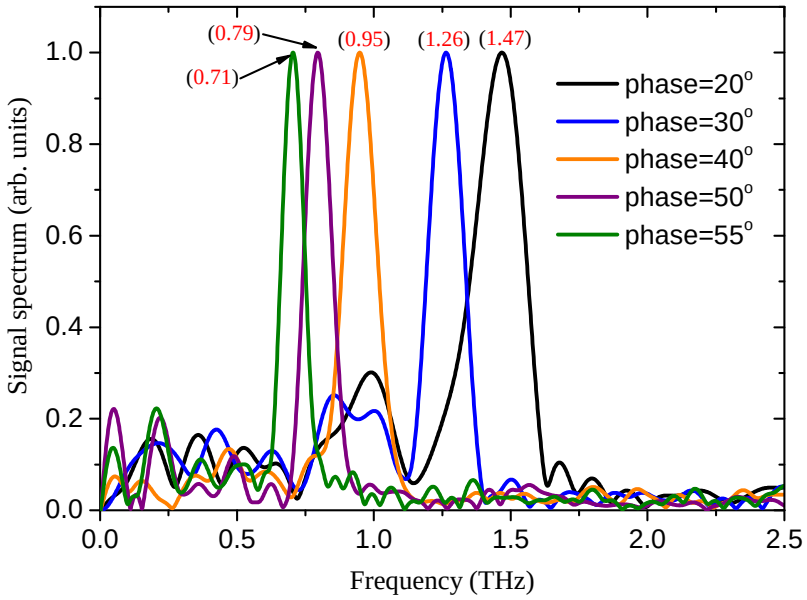


Figure 5.11: Normalised spectra of the cTR signal generated by a train of microbunches at RF gun phases of 20°, 30°, 40°, 50°, and 55°.

periodicities in the range of 0.68 ps to 1.41 ps (frequency from 1.47 to 0.71 THz) were obtained.

Table 5.1: Comparison of the line width of cTR generated by microbunch trains

Central frequency (THz)	FWHM† in theory (THz)	FWHM measured (THz)	Relative difference*
0.71	0.09	0.093 THz	0.42%
0.79	0.10	0.115 THz	1.9%
0.95	0.121	0.136 THz	1.58%
1.26	0.16	0.154 THz	−0.48%
1.47	0.187	0.207 THz	1.36%

† FWHM: Full width at half maximum
* Relative difference calculated as: (measured-theory)/Central frequency

The spectral line width $\Delta\nu$ at frequency ν can be defined by the full width at half maximum (FWHM). Using the Equation 2.8 in Chapter 2, the spectral line width has been calculated as $\Delta\nu = 0.89\nu/M$ [78], where M is the number of microbunches ($M = 7$ in our experiments). It indicates that, for a fixed number of microbunches, the line width of the spectrum becomes larger as the central frequency increases. The result of measurement and the comparison with theoretical predictions are shown in Table 5.1. It shows that the measured line widths agree very well with theoretical predictions.

5.3.2 cSPr from microbunch trains

cSPr at different angles

This section describes the measurement of the cSPr, generated using microbunch trains, at different observation angles. A schematic of the experiment is shown in Figure 5.12. The Michelson interferometer system was not used for these measurements, one reason being that the interferometer system was aligned for a detection angle of θ=90 degrees, for the measurements at other angles, the system has to be realigned. Another reason is that the transmission efficiency of the interferometer system was around 10% (with the loss mainly due to absorption in air - exacerbated by the high humidity at TTX - over the approximately 2 m optical path of the interferometer). The bolometer in front of the window, without the

interferometer system, was able to detect a signal (at the oscilloscope) of around 40 mV with a noise level around 5 mV. Placing the interferometer in the optical path resulted in a measured signal which was of the same order of magnitude as the noise level.

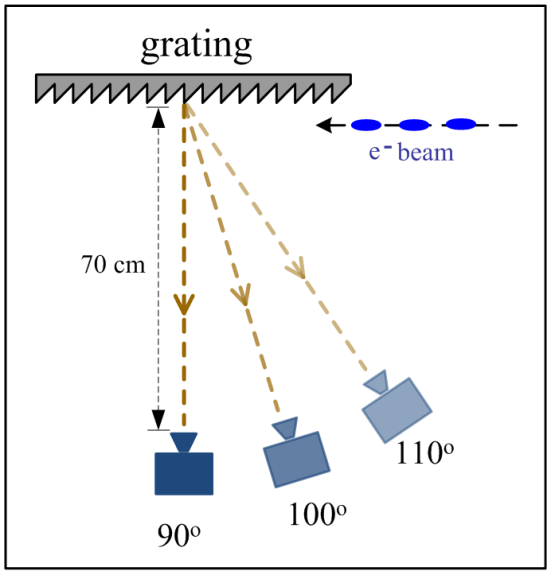


Figure 5.12: A schematic of the setup for the measurement of cSPr at different detection angles.

In this experiment the separation between the metal grating and the bolometer was around 70 cm. Positioning the bolometer at detection angles of 90, 100 and 110 degrees, the dependence of the radiation intensity of cSPr on the RF gun phase could be measured and the results of this are shown in Figure 5.13. As mentioned before, the microbunch periodicity can be tuned by changing the RF gun phase. The microbunch frequencies at RF gun phases of 30°, 40°, 50°, and 55° were obtained from the experiment (Figure 5.11). The microbunch frequencies, shown in the parenthesis in Figure 5.13, were obtained using the Astra program package [79] (a Space Charge Tracking Algorithm) for the RF gun phases of 35°, 45°, and 60°, respectively.

It can be seen from Figure 5.13 that, although an overall decrease in intensity is observed when the microbunch frequency is lowered from 1.26 THz to 0.64 THz (at the detection angle of 90 degrees), the measured intensity increases at microbunch frequencies of around 0.86 THz (angle=100 degrees) and 0.82 THz (angle=110 degrees). The two microbunch frequencies coincide with the frequencies of the second harmonics of cSPr at these two

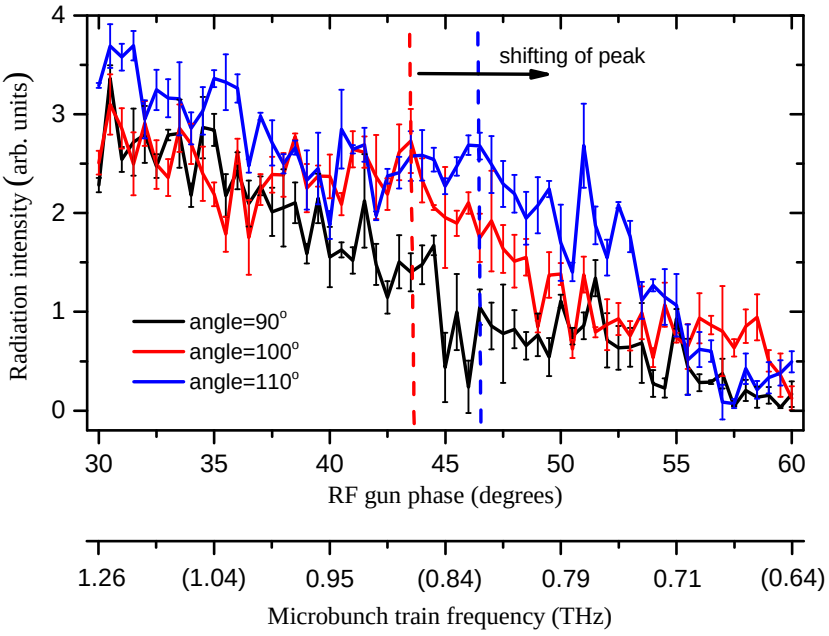


Figure 5.13: Radiation intensity of cSPr versus RF gun phase (the microbunch frequencies shown in the parenthesis were obtained using Astra simulations and the other frequencies were from the experiment).

detection angles. This indicates that the existence of periodic microbunches makes the emitted cSPr concentrate at around the microbunch frequency.

We can also see there should be a peak of the radiation intensity at around 1 THz at the detection angle of 90 degrees, there are a number of possible reasons for the missing of it. It should be noted that, during the scan of the RF gun phase, the current in the solenoid was fixed. However, since the optimised focusing depending on the phase of the RF gun, the microbunched beam may not have remained well focused in the transverse direction. It was estimated that the transverse size of microbunch trains at the metal grating was around 2 mm. The larger transverse size means that the beam had to be moved further away from the grating to avoid the intersection of electrons with the grating. Otherwise, bremsstrahlung and X-rays will be produced and they will affect the measurement. As a result the beam-grating separation was estimated at around 3 mm. The large beam transverse size and the large beam-grating separation reduced the generation of cSPr significantly. Additionally, the efficiency of the excitation of the second harmonic of cSPr is much lower than that of the

first harmonic, which also decreases the intensity of the cSPr generated by microbunch trains in the experiment. Assuming a train of microbunches was formed initially in good condition (well focused and stable), the enhancement of the radiation intensity at the microbunch frequency should be achieved.

Line width comparison of cSPr based on previous experiment

The metal grating used for this experiment (August 2018) has a period of 600 μm. Due to the limited experimental time, gratings with different periods and profiles were not used. To compare the line width of cSPr, the results from a previous experiment (carried out at TTX in May 2017) were also analysed. The previous experiment used the same grating setup (Figure 5.5), but they were installed in a larger chamber with a small vacuum window (Figure 5.14). The gratings with periods of 300 μm and 600 μm were both used in the experiment.

The diameter of the vacuum window was 4 cm and the distance between beam and window was 50 cm. Therefore, the measurement of cSPr was restricted to the detection angle of 90 degrees. The same Michelson interferometer system together with the bolometer were used.

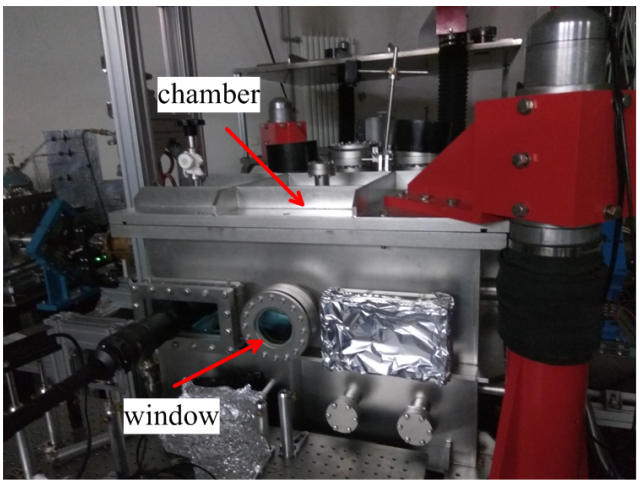


Figure 5.14: Photograph of the chamber where grating was positioned inside at previous experiment (May 2017).

As the microbunch trains were well focused in the transverse direction (transverse size

of around 400 μm) in this experiment, which was much smaller than the beam size in the experiment carried out in August 2018. The radiation signal at the oscilloscope was around 30 mV (much higher than the noise level of around 5 mV). Therefore, the spectrum of the cSPr generated using microbunch trains can be measured.

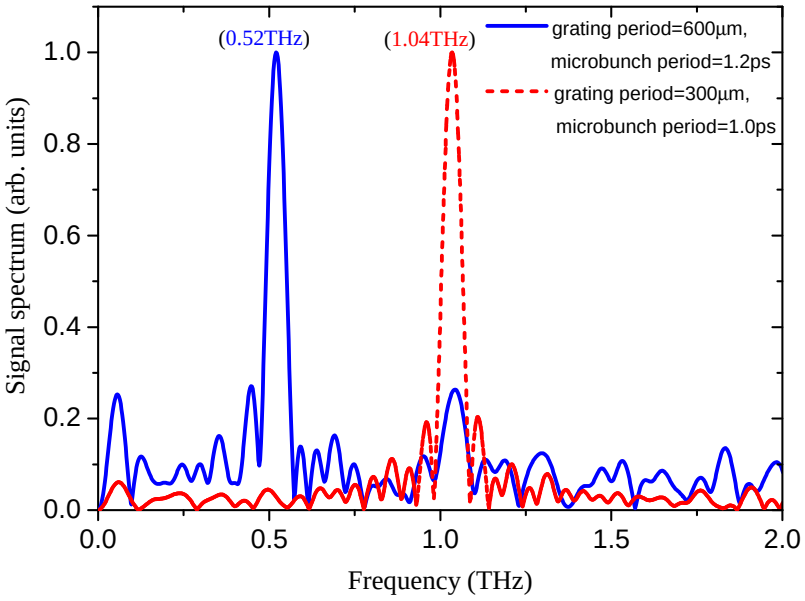


Figure 5.15: Normalised spectrum of the cSPr signal generated by microbunch trains at the detection angle of 90 degrees (solid line: microbunch trains with a periodicity of 1.2 ps and a grating with a period of 600 μm, dashed line: microbunch trains with a periodicity of 1 ps and a grating with a period of 300 μm).

The normalised spectrum of the cSPr signal generated by microbunch trains at the detection angle of 90 degrees is shown in Figure 5.15. The solid line indicates the spectrum of the radiation generated by the microbunch train with a periodicity of 1.2 ps travelling above the grating with a period of 600 μm. The dashed line refers to the microbunch train with a periodicity of 1.0 ps interacting with the grating with a period of 300 μm. The central frequencies of the spectrum for these two cases are measured to be around 0.52 THz and 1.04 THz, respectively, which is as expected from theory (see Equation 2.1).

It should be noted that the spectral resolution of the Michelson interferometer system used in the experiment is determined by its maximum scanning distance. The relationship is $\Delta f = c/(2x_l)$ [80], where Δf is the spectral resolution, c is the speed of light and x_l is

the absolute travelling distance of the movable mirror of the interferometer. The travelling distances are both around 3 mm for the two measurements. The spectral resolution is calculated to be 0.05 THz.

The line widths of the cSPr generated by microbunch trains are compared in Table 5.2. The line width of the spectrum centred at 0.52 THz is 0.062 THz and the line width is 0.063 THz for the spectrum with central frequency of 1.04 THz. The line width of cSPr from measurement is close to the spectral resolution of the interferometer system. Even in this case it was found that the line width of cSPr is much narrower than that of cTR presented in previous section.

Table 5.2: Comparison of the line width of cSPr generated by microbunch trains[†].

Central frequency (THz)	FWHM measured (THz)
0.52	0.062 $\pm$0.05*
1.04	0.063 $\pm$0.05*

[†] Data taken from the experiment carried out in May 2017.
[†] The uncertainty is mainly due to the spectral resolution of interferometer system.

For a detector in the far-field region, the theoretical line width of cSPr can be estimated using ν/nN, where ν is the observation frequency, n is the order of radiation and N is the number of facets of the metal grating. The line width from theory is calculated to be around 0.003 THz, which is much less than measurement. Therefore, in order to increase the accuracy of measurement, the spectral resolution of the interferometer should be increased by increasing the scanning distance of the movable mirror in future experiments.

5.4 Summary and Discussion

Experiments have been carried out at the TTX facility to investigate the THz radiation generated via the cSPr mechanism from a single electron bunch and a train of microbunches. The measurement of the spectrum of radiation generated by a single bunch at 90 degrees confirmed the generation of cSPr. The degree of polarization of cSPr at 90 degrees was measured to be around 80%. A train of microbunches with tunable periodicities were generated

in this experiment. The spectral line widths of the cTR and cSPr generated by microbunch trains were measured and analysed. It was found that the spectral line widths of the cSPr generated by microbunch trains were measured to be around 0.06 THz and narrower than those from cTR. Measurements were performed to study the variation of the radiation intensity, at different detection angles, when changing the periodicity of microbunch trains. It indicates that the microbunching of the electron bunches results in the intensity of the generated cSPr concentrating at the microbunch frequency.

In order to estimate the energy of the radiation generated by the beam from facilities like TTX, the following calculation has been performed. The calculation uses the following beam parameters: the beam energy is 45 MeV, the total charge is 1 nC, and the longitudinal bunch form factor is around 0.3 with a microbunch periodicity of 1 ps. In addition, the grating parameters selected follows: the facet angle of the sawtooth grating is 30°, the period is 300 μm, total length is 100 mm, and grating width is 10 mm. The distance between beam and grating is set to be 0.5 mm. Using the GFW code (discussed in detail in Chapter 2), the radiation energy from the microbunch train is estimated to be around 10 μJ at the radiation frequency of 1 THz in the far-field region. The peak radiation power is on the order of tens of kW.

A potential way to increase the radiation energy is to increase the number of microbunch trains. This can be achieved by increasing the repetition rate of the UV laser system which drives the photocathode RF gun. Increasing the repetition rate of the UV laser system from a few Hz to tens of kHz (commercially available [81]) could result in an increase in the radiation energy from a few μJ to the level of mJ.

Chapter 6

Summary and suggestions for future work

This thesis describes the numerical and experimental studies of the properties of coherent terahertz (THz) Smith-Purcell radiation generated by a train of electron microbunches. I suggest using a train of microbunches, instead of a single bunch, because the splitting of the beam charge into a number of microbunches is an effective method to suppress the strong dispersion forces in a bunch caused by space charge effects when the beam charge is high (above 1 nC).

Several ways of generating microbunched electron beams were considered. These include the modulation of a long electron bunch in a plasma channel, direct generation of microbunches from a photocathode (at the KEK-LUCX facility), and the modulation of a long bunch (with an initial density modulation) using the longitudinal space charge forces during its propagation in the beamline (at the TTX facility). The interaction between a long bunch and a plasma channel was studied in detail using both analytical theory and numerical simulations. It was demonstrated that the microbunch periodicities can be controlled by changing the plasma density. Our simulations show that a train with microbunch frequencies of 1, 1.5, and 2 THz can be generated and propagated over a distance of 10 cm in vacuum. Although the beam modulation was only investigated analytically and numerically (without

experiments), there is no theoretical obstacle to electron microbunches being created in this way and to their application in the generation of THz generation. Recent experiments at AWAKE [61] have been successful in generating proton microbunches and in using them for the acceleration of electron beams. The principle of the modulation of an electron beam in a plasma is the same, but a much shorter plasma channel (several cm) is required as the mass of an electron is much smaller than that of a proton. Assuming a plasma density in the range of $10^{15}/\text{cm}^3$ to $10^{17}/\text{cm}^3$, the frequency tunability would be between 0.3 THz and 3 THz.

The generation of coherent THz Smith-Purcell radiation using microbunch trains with tunable microbunch periodicities was investigated. Numerical studies were carried out to investigate the THz radiation generated by a train of microbunches in the near-field (in VSim) and the far-field region (in CST). It was demonstrated that the microbunching effect enables the cSPr intensity to be localised around the microbunch frequency and its harmonics. Subsequent experiments were carried out at the TTX facility to conduct comparative studies of the THz radiation generated by a single electron bunch and a train of microbunches. The degree of polarization of the cSPr generated by a single bunch was measured to be around 80% at the detection angle of 90 degrees. This is reasonable agreement with theoretical expectations. The spectral line widths of the cSPr generated by microbunch trains were measured to be around 0.06 THz and narrower than those from coherent transition radiation. Measurements were also performed to study the variation of the radiation intensity, at different detection angles, when changing the periodicity of microbunch trains. It indicates that the microbunching of electron bunches results in the intensity of the generated cSPr concentrating at around the microbunch frequency. This provides an alternative method for the realisation of tunable THz radiation.

However, the experiments at the TTX facility were not fully optimised. The transverse focusing of the microbunch trains was not good enough, which resulted in the low radiation intensity. Also, the TTX facility could not provide microbunch trains with frequencies corresponding to the first harmonic of Smith-Purcell radiation at the observation angles and

this further reduced the radiation efficiency. These issues could be addressed by improving the transverse focusing of the microbunch trains through fine tuning and by appropriate modifications to the beamline in a future experiment. The optimization of grating structures could also increase the radiation intensity. Our numerical simulations indicate a well-focused microbunch train, generated from facilities like TTX, could yield radiation energies around 10 μJ at the radiation frequency of 1 THz in the far-field region. The peak radiation power would be of the order of tens kW. Improving the high repetition rate of the driving laser system for the photocathode RF gun is also a promising way to further increase the THz radiation intensity for practical applications.

In separate but related experiments, a new method was investigated to monitor the separation between microbunches. The method is based on the analysis of coherent Smith-Purcell radiation and experiments were carried out with two microbunches at the KEK-LUCX facility to confirm its validity. It was found that the variation of separation between microbunches leads to the variation of the intensity of the monochromatic signal from coherent Smith-Purcell radiation, which was then used to monitor the separation of microbunch trains. Comparing with analytical predictions, the averaged error for the measured microbunch separation was less than 1% with the maximum error of 4.9%. The measured results agree well with theoretical predictions. The proposed method to monitor the microbunch separation requires additional information from the accelerator to ensure the accuracy of a single-frequency measurement. Another measurement at a different frequency would be able to solve the problem and would allow the unambiguous determination of the absolute microbunch separation over a larger range. Also, it is possible to apply this method to monitor microbunch trains with different charge distribution and more microbunches (i.e. more than 2). All of these require detailed analysis in the future.

The work in this thesis is of direct relevance to the realisation of a tunable THz source based on coherent Smith-Purcell radiation. These proof of concept studies illustrate the feasibility of the approach for the generation of high power, tunable THz radiation using microbunched electron beams.

Appendix A

Radiation from a bunch of charged particles

Assuming a beam consisting of a bunch of N charged particles and ignoring the Coulomb forces between individual particles, the electric field in the time domain produced by the N particles at an observation point P in the far-field region can be seen as the superposition of the fields generated from individual particles:

$$\boldsymbol{E}(t) = \sum_{i=1}^{N} \boldsymbol{E}_i(t) \tag{A.1}$$

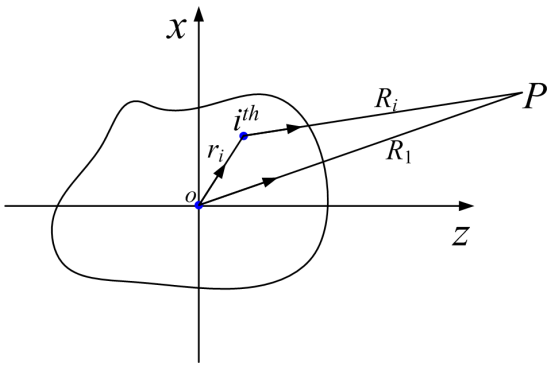


Figure A.1: A schematic of radiation from a bunch of particles.

In Figure A.1, it is assumed that there is a reference particle at the origin radiating a

field $\boldsymbol{E}_1(t)$. The field $\boldsymbol{E}_i(t)$ produced by the i^{th} particle has a time delay Δt_i relative to the reference particle and can be written as $\boldsymbol{E}_1(t + \Delta t_i)$ with $\Delta t_i = (R_i - R_1)/c$. In this case the total electric field in the frequency domain is given by:

$$\boldsymbol{E}(\nu) = \boldsymbol{E}_1(\nu) \sum_{i=1}^{N} \exp(j2\pi\nu\Delta t_i) \tag{A.2}$$

where ν is the observation frequency. As the observation point P is in the far-field region, $R_1 - R_i \approx \boldsymbol{n} \cdot \boldsymbol{r_i}$ where $\boldsymbol{n}$ is unit vector from the reference particle to point P, and $\boldsymbol{r}_i$ is the distance vector from the i^{th} particle to the reference particle.

The radiation energy spectrum at a given position in the far-field region in free space is given by [82]:

$$\frac{dU}{d\nu} = 2\epsilon_0 c|\boldsymbol{E}(\nu)|^2 \tag{A.3}$$

Then the radiation spectrum at point P becomes:

$$\frac{dU}{d\nu} = \frac{dU_1}{d\nu} \left| \sum_{i=1}^{N} \exp(-j\boldsymbol{k} \cdot \boldsymbol{r}_i) \right|^2 \tag{A.4}$$

where $\frac{dU_1}{d\nu}$ is the radiation spectrum of the reference particle and $\boldsymbol{k} = \frac{2\pi\nu}{c}\boldsymbol{n}$ is the wave vector. If particle distribution ρ is uncorrelated in the transverse and longitudinal directions, it can be written as $\rho(r, z) = \rho(r)\rho(z)$. Therefore:

$$\begin{aligned} \left| \sum_{i=1}^{N} \exp(-j\boldsymbol{k} \cdot \boldsymbol{r}_i) \right|^2 &= N + N(N-1)|F_r(\nu)|^2|F_z(\nu)|^2 \\ F_r(\nu) &= \int_{-\infty}^{+\infty} \rho(r) \exp(-j\boldsymbol{k} \cdot \boldsymbol{r}) dr \\ F_z(\nu) &= \int_{-\infty}^{+\infty} \rho(z) \exp(-j\boldsymbol{k} \cdot \boldsymbol{z}) dz \end{aligned} \tag{A.5}$$

Appendix B

Beam envelope model

The following analysis is based on References [83, 84]. Consider a beam propagating in the z direction, in the transverse phase space (x, y, x', y'), a four dimensional particle distribution can be written as $f(x, y, x', y')$. The second moment of x in the particle coordinates is defined by:

$$\langle x^2 \rangle = \frac{\int\int\int\int x^2 f(x, y, x', y') dx dy dx' dy'}{\int\int\int\int f(x, y, x', y') dx dy dx' dy'} \tag{B.1}$$

In an axisymmetric cylindrical system, the average of function $g(r)$ for all electrons in the transverse plane is given by:

$$\langle g(r) \rangle = \frac{\int_0^{+\infty} g(r) n_b(r) r dr}{\int_0^{+\infty} n_b(r) r dr} \tag{B.2}$$

Consider a channel with an external force (due to external magnetic field) and space charge force (generally nonlinear) acting on a charged beam. In Cartesian coordinates, the transverse motion of a charged particle in such a channel can be written in the form:

$$\begin{aligned} x'' + k_{x0} x - F_x = 0 \\ y'' + k_{y0} y - F_y = 0 \end{aligned} \tag{B.3}$$

where $x'' = \frac{\partial^2 x}{\partial z^2}$, z is the propagation distance, function F_x and F_y are the forces due to the electric and magnetic self-fields of the beam defined by:

$$F_{x(y)} = \frac{qE_{x(y)}(1-\beta^2)}{\gamma mc^2\beta^2} = \frac{qE_{x(y)}}{mc^2\gamma^3\beta^2} \tag{B.4}$$

For an axisymmetric beam without external magnetic field, $k_{x0} = k_{y0} = k_0 = 0$. If the distribution $n_b = n_{b0}e^{-(x^2+y^2)/2\sigma_r^2}$, we can get:

$$\frac{\partial^2\sigma_r}{\partial z^2} - \frac{\varepsilon_x^2}{{\sigma_r}^3} - \frac{\langle xW_x\rangle}{\gamma mc^2\sigma_r} = 0 \tag{B.5}$$

where $\sigma_r = \sqrt{\langle x^2\rangle} = \sqrt{\langle y^2\rangle} = \sqrt{\langle r^2/2\rangle}$ is the root mean square (rms) beam size, $\varepsilon_x = [\langle x^2\rangle\langle x'^2\rangle - \langle xx'\rangle^2]^{1/2}$ is the beam rms emittance in x direction, γ is the beam relativistic factor and W_x is the force in x direction. Assuming the beam profile is azimuthally symmetric, we have $x = r\cos\theta$, $y = r\sin\theta$, $W_x = W_r\cos\theta$, $W_y = W_r\sin\theta$. Then

$$\begin{aligned}\langle xW_x\rangle = \langle yW_y\rangle &= \frac{\int\int\int\int xW_x n(x,y,x',y')dxdydx'dy'}{\int\int\int\int n(x,y,x',y')dxdydx'dy'} = \frac{\int\int xW_x n(x,y)dxdy}{\int\int n(x,y)dxdy} \\ &= \frac{\int\int rW_r\cos^2(\theta)n(r)rdrd\theta}{\int\int n(r)rdrd\theta} \\ &= \frac{\int_0^{2\pi}\cos^2(\theta)d\theta}{\int_0^{2\pi}d\theta}\frac{\int rW_r n(r)rdr}{\int n(r)rdr} = \frac{1}{2}\langle rW_r\rangle\end{aligned} \tag{B.6}$$

The envelope equation for the azimuthally symmetric beam becomes [64]:

$$\frac{\partial^2\sigma_r}{\partial z^2} - \frac{\varepsilon^2}{{\sigma_r}^3} - \frac{1}{\gamma mc^2}\frac{\langle rW_r\rangle}{2\sigma_r} = 0 \tag{B.7}$$

where $\varepsilon = [\langle x^2\rangle\langle x'^2\rangle - \langle xx'\rangle^2]^{1/2} = [\langle r^2\rangle\langle r'^2\rangle - \langle rr'\rangle^2]^{1/2}/2$ ($x' = dx/dz$, $r' = dr/dz$) is the beam transverse rms emittance.

Appendix C

Linear wakefield theory

The following analysis is based on Reference [62]. Consider an electron beam propagating through an initially homogeneous plasma channel while having charge density much less than the electron density of the plasma. The response of the plasma can be found from the linearized equations of motion, continuity, and Maxwell's equations (SI Unit):

$$\frac{d\vec{v}_1}{dt} = \frac{-e\vec{E}}{m} \tag{C.1}$$

$$\frac{\partial n_1}{\partial t} + n_0 \nabla \cdot \vec{v}_1 = 0 \tag{C.2}$$

$$\nabla \cdot \vec{E} = \frac{\rho_0 - e n_1}{\epsilon_0} \tag{C.3}$$

$$\nabla \times \vec{E} = -\frac{\partial \vec{B}}{\partial t} \tag{C.4}$$

$$\nabla \times \vec{B} = \mu_0 \vec{J} + \frac{1}{c^2}\frac{\partial \vec{E}}{\partial t} \tag{C.5}$$

where n_0, n_1 are the background and perturbed plasma density, $\rho_0 = -en_0$, $\vec{v}_1$ is the perturbed velocity, $\vec{v}_0 = 0$ (the background plasma is static), $\vec{E}$ is the electric field of the plasma, and c is the speed of light.

Combing Equations C.1 - C.3, the wave equation for the response of the plasma density

can be obtained:

$$\frac{\partial^2 n_1}{\partial t^2} + \omega_{pe}^2 n_1 = -\omega_{pe}^2 n_b \tag{C.6}$$

where $\omega_{pe} = \sqrt{e^2 n_0 / m_0 \epsilon_0}$ is the plasma electron angular frequency, n_0 is the plasma density, m_0 is the rest mass of electron, ϵ_0 is the vacuum dielectric constant, $n_b(\xi, r)$ is the bunch distribution, $\xi = -ct + z$ is a co-moving variable, which indicates the relative distance from the centre of beam. Then we can get $\frac{\partial}{\partial z} = \frac{\partial}{\partial \xi}$, $\frac{\partial^2}{\partial t^2} = c^2 \frac{\partial^2}{\partial^2 \xi}$. From Equation C.6, we have:

$$\frac{\partial^2 n_1}{\partial \xi^2} + k_{pe}^2 n_1 = -k_{pe}^2 n_b \tag{C.7}$$

where $k_{pe} = \omega_{pe}/c$ is the plasma wave number. For a symmetric bunch, if the transverse and the longitudinal profile are uncorrelated, the initial particle density can be written as $n_b(\xi, r) = n_{b_\parallel}(\xi) \cdot n_{b_\perp}(r)$. The solution to Equation C.7 can be written as:

$$\begin{aligned} n_1 &= -k_{pe} \int_{+\infty}^{\xi} n_b(\xi', r) \sin k_{pe}(\xi - \xi') d\xi' \\ &= -k_{pe} n_{b_\perp}(r) \int_{+\infty}^{\xi} n_{b_\parallel}(\xi') \sin k_{pe}(\xi - \xi') d\xi' \end{aligned} \tag{C.8}$$

Taking the rotation of Equation C.4 and substituting from Equation C.5 gives:

$$(\nabla_\perp^2 - k_{pe}^2)\vec{E} = \frac{-e}{\epsilon_0} \nabla n_1 \tag{C.9}$$

In a cylindrical coordinate, $\nabla_\perp^2 = \frac{1}{r}\frac{\partial}{\partial r}(r\frac{\partial}{\partial r})$. If considering the z direction, we can get:

$$(\nabla_\perp^2 - k_{pe}^2) E_z(\xi, r) = \frac{-e}{\epsilon_0} \frac{\partial n_1}{\partial z} \tag{C.10}$$

If we set $E_z(\xi, r) = \frac{dZ(\xi)}{d\xi} \cdot R(r)$, then

$$\frac{dZ(\xi)}{d\xi} = \frac{-e}{\epsilon_0 k_{pe}^2} \frac{\partial n_1}{\partial z} \frac{1}{n_{b_\perp}(r)} = \frac{e}{\epsilon_0} \int_{+\infty}^{\xi} n_{b_\parallel}(\xi') \cos k_{pe}(\xi - \xi') d\xi' \tag{C.11}$$

For $R(r)$, we can get:

$$(\nabla_\perp^2 - k_{pe}^2)R(r) = k_{pe}^2 n_{b_\perp}(r) \tag{C.12}$$

We know that for modified Bessel functions, $d[K_0(x)]/dx = -K_1(x)$, $d[I_0(x)]/dx = I_1(x)$, $d[xK_1(x)]/dx = -xK_0(x)$, $d[xI_1(x)]/dx = xI_0(x)$. For Equation $(\nabla_\perp^2 - k_{pe}^2)R(r) = 0$, the solution $R(r) \propto c_1 I_0(k_{pe}r) + c_2 K_0(k_{pe}r)$. For Equation C.12, the solution becomes:

$$\begin{aligned} R(r) &= k_{pe}^2 \int_0^{+\infty} r'dr' n_{b_\perp}(r') K_0(k_{pe}|\vec{r} - \vec{r}'|) \\ &= k_{pe}^2 K_0(k_{pe}r) \int_0^r r'dr' n_{b_\perp}(r') I_0(k_{pe}r') \\ &+ k_{pe}^2 I_0(k_{pe}r) \int_r^{+\infty} r'dr' n_{b_\perp}(r') K_0(k_{pe}r') \end{aligned} \tag{C.13}$$

In summary, according to linear wakefield theory, the longitudinal wakefield E_z and the transverse wakefield E_r can be written as [62, 63]:

$$E_z(\xi, r) = \frac{dZ(\xi)}{d\xi} \cdot R(r), \qquad E_r(\xi, r) = Z(\xi) \cdot \frac{dR(r)}{dr} \tag{C.14}$$

where

$$\frac{dZ(\xi)}{d\xi} = \frac{e}{\epsilon_0} \int_{+\infty}^{\xi} n_{b_\parallel}(\xi') \cos k_{pe}(\xi - \xi') d\xi' \tag{C.15}$$

$$Z(\xi) = \frac{e}{\epsilon_0 k_{pe}} \int_{+\infty}^{\xi} n_{b_\parallel}(\xi') \sin k_{pe}(\xi - \xi') d\xi' \tag{C.16}$$

$$\begin{aligned} R(r) &= k_{pe}^2 \int_0^{+\infty} r'dr' n_{b_\perp}(r') K_0(k_{pe}|\vec{r} - \vec{r}'|) \\ &= k_{pe}^2 K_0(k_{pe}r) \int_0^r r'dr' n_{b_\perp}(r') I_0(k_{pe}r') \\ &+ k_{pe}^2 I_0(k_{pe}r) \int_r^{+\infty} r'dr' n_{b_\perp}(r') K_0(k_{pe}r') \end{aligned} \tag{C.17}$$

$$\begin{aligned} \frac{dR(r)}{dr} &= -k_{pe}^3 K_1(k_{pe}r) \int_0^r r'dr' n_{b_\perp}(r') I_0(k_{pe}r') \\ &+ k_{pe}^3 I_1(k_{pe}r) \int_r^{+\infty} r'dr' n_{b_\perp}(r') K_0(k_{pe}r') \end{aligned} \tag{C.18}$$

Comparison for different profiles

There are mainly two types of bunches to be considered here, one is uniform bunch with a linear rise profile and the other is uniform bunch with a sinusoidal rise profile. The charge density distributions are shown in Figure 3.2(a). Assuming the peak density is n_{b0}, the charge density of the uniform bunch with a linear rise profile can be written as (neglecting the radial component):

$$n_b(\xi) = \begin{cases} n_{b0}\frac{L}{\delta c}(1-\frac{\xi}{L}) & \text{if } L-\delta c \le \xi \le L \\ n_{b0} & \text{if } -(L-\delta c) \le \xi \le L-\delta c \\ n_{b0}\frac{L}{\delta c}(1+\frac{\xi}{L}) & \text{if } -L \le \xi \le -(L-\delta c) \end{cases} \tag{C.19}$$

For a uniform bunch with a sinusoidal rise profile, the bunch density can be written as:

$$n_b(\xi) = \begin{cases} n_{b0}\sin[\frac{\pi}{2\delta c}(L-\xi)] & \text{if } L-\delta c \le \xi \le L \\ n_{b0} & \text{if } -(L-\delta c) \le \xi \le L-\delta c \\ n_{b0}\sin[\frac{\pi}{2\delta c}(L+\xi)] & \text{if } -L \le \xi \le -(L-\delta c) \end{cases} \tag{C.20}$$

where $\xi = -v_b t + z$ is the relative distance from the middle of the bunch, v_b is the beam velocity in z direction (can be consider as c for ultrarelativistic beam), L is half of the longitudinal length of the bunch, and δ ($-L/c \le \delta \le L/c$) is the rise time. Once we know the bunch longitudinal profile, the longitudinal profile dependent transverse wakefield can be written as:

$$f(\xi) = \int_{+\infty}^{\xi} n_b(\xi')\sin k_{pe}(\xi-\xi')d\xi' \tag{C.21}$$

Bunch with linear rise profile

The wakefield analytical solution to a uniform bunch with linear rise time (assume n_{b0} is unit 1) is as follows:

1) If $L-\delta c \le \xi \le L$

$$\begin{aligned} f(\xi) &= \int_{+\infty}^{\xi} n_b(\xi')\sin k_{pe}(\xi-\xi')d\xi' = \int_{+L}^{\xi} \frac{L}{\delta c}(1-\frac{\xi'}{L})\sin k_{pe}(\xi-\xi')d\xi' \\ &= \frac{1}{\delta c k_{pe}^2}[k_{pe}(L-\xi)+\sin k_{pe}(\xi-L)] \end{aligned} \tag{C.22}$$

2) If $-(L-\delta c) \le \xi \le L-\delta c$

$$\begin{aligned} f(\xi) &= \int_{+L}^{L-\delta c} \frac{L}{\delta c}(1-\frac{\xi'}{L})\sin k_{pe}(\xi-\xi')d\xi' + \int_{L-\delta c}^{\xi} \sin k_{pe}(\xi-\xi')d\xi' \\ &= \frac{1}{\delta c k_{pe}^2}[k_{pe}\delta c+\sin k_{pe}(\xi-L)-\sin k_{pe}(\xi+\delta c-L)] \end{aligned} \tag{C.23}$$

3) If $-L \le \xi \le -(L-\delta c)$

$$\begin{aligned} f(\xi) &= \int_{+L}^{L-\delta c} \frac{L}{\delta c}(1-\frac{\xi'}{L})\sin k_{pe}(\xi-\xi')d\xi' + \int_{L-\delta c}^{-(L-\delta c)} \sin k_{pe}(\xi-\xi')d\xi' \\ &+ \int_{-(L-\delta c)}^{\xi} \frac{L}{\delta c}(1+\frac{\xi'}{L})\sin k_{pe}(\xi-\xi')d\xi' \\ &= \frac{1}{\delta c k_{pe}^2}[\sin k_{pe}(\xi-L)-\sin k_{pe}(\xi+\delta c-L)+k_{pe}(\xi+L)-\sin k_{pe}(\xi-\delta c+L)] \end{aligned} \tag{C.24}$$

Bunch with sinusoidal rise profile

The analytical wakefield solution to a uniform bunch with sinusoidal rise time is as follows (assuming n_{b0} is unit 1). We have to consider two situations: $k_{pe}\delta c = \pi/2$ and $k_{pe}\delta c \neq \pi/2$.

1. When $k_{pe}\delta c \neq \pi/2$

1) If $L-\delta c \le \xi \le L$

$$\begin{aligned} f(\xi) &= \int_{+L}^{\xi} \sin\frac{\pi}{2\delta c}(L-\xi')\sin k_{pe}(\xi-\xi')d\xi' \\ &= \frac{2\delta c}{\pi^2-4\delta^2c^2k_{pe}^2}[\pi\sin k_{pe}(L-\xi)-2\delta c k_{pe}\sin\frac{\pi}{2\delta c}(L-\xi)] \end{aligned} \tag{C.25}$$

2) If $-(L-\delta c) \le \xi \le L-\delta c$

$$\begin{aligned} f(\xi) &= \int_{+L}^{L-\delta c} \sin\frac{\pi}{2\delta c}(L-\xi')\sin k_{pe}(\xi-\xi')d\xi' + \int_{L-\delta c}^{\xi} \sin k_{pe}(\xi-\xi')d\xi' \\ &= \frac{2\delta c}{\pi^2 - 4\delta^2 c^2 k_{pe}^2}[\pi \sin k_{pe}(L-\xi) - 2\delta c k_{pe}\cos k_{pe}(\delta c+\xi-L)] \\ &+ \frac{1}{k_{pe}}[1-\cos k_{pe}(\delta c+\xi-L)] \end{aligned} \tag{C.26}$$

3) If $-L \le \xi \le -(L-\delta c)$

$$\begin{aligned} f(\xi) &= \int_{+L}^{L-\delta c} \sin\frac{\pi}{2\delta c}(L-\xi')\sin k_{pe}(\xi-\xi')d\xi' + \int_{L-\delta c}^{-(L-\delta c)} \sin k_{pe}(\xi-\xi')d\xi' \\ &+ \int_{-(L-\delta c)}^{\xi} \sin\frac{\pi}{2\delta c}(L+\xi')\sin k_{pe}(\xi-\xi')d\xi' \\ &= \frac{2\delta c\pi}{\pi^2 - 4\delta^2 c^2 k_{pe}^2}\sin k_{pe}(L-\xi) - \frac{4\delta^2 c^2 k_{pe}}{\pi^2 - 4\delta^2 c^2 k_{pe}^2}\sin\frac{\pi}{2\delta c}(L+\xi) \\ &+ \frac{1}{k_{pe}}[\cos k_{pe}(\xi+L-\delta c) - \cos k_{pe}(\delta c+\xi-L)] \end{aligned} \tag{C.27}$$

2. When $k_{pe}\delta c = \pi/2$

1) If $L-\delta c \le \xi \le L$

$$\begin{aligned} f(\xi) &= \int_{+L}^{\xi} \sin k_{pe}(L-\xi')\sin k_{pe}(\xi-\xi')d\xi' \\ &= \frac{\xi-L}{2}\cos k_{pe}(L-\xi) + \frac{1}{2k_{pe}}\sin k_{pe}(L-\xi) \end{aligned} \tag{C.28}$$

2) If $-(L-\delta c) \le \xi \le L-\delta c$

$$\begin{aligned} f(\xi) &= \int_{+L}^{L-\delta c} \sin k_{pe}(L-\xi')\sin k_{pe}(\xi-\xi')d\xi' + \int_{L-\delta c}^{\xi} \sin k_{pe}(\xi-\xi')d\xi' \\ &= \frac{1}{4k_{pe}}[2\sin k_{pe}(L-\xi) - \pi\cos k_{pe}(L-\xi)] + \frac{1}{k_{pe}}[1-\cos k_{pe}(\delta c+\xi-L)] \end{aligned} \tag{C.29}$$

3) If $-L \leq \xi \leq -(L-\delta c)$

$$
\begin{aligned}
f(\xi) &= \int_{+L}^{L-\delta c} \sin k_{pe}(L-\xi')\sin k_{pe}(\xi-\xi')d\xi' + \int_{L-\delta c}^{-(L-\delta c)} \sin k_{pe}(\xi-\xi')d\xi' \\
&+ \int_{-(L-\delta c)}^{\xi} \sin k_{pe}(L+\xi')\sin k_{pe}(\xi-\xi')d\xi' \\
&= \frac{1}{4k_{pe}}[2\sin k_{pe}(L-\xi) - \pi\cos k_{pe}(L-\xi)] \\
&+ \frac{1}{k_{pe}}[\cos k_{pe}(\xi+L-\delta c) - \cos k_{pe}(\delta c+\xi-L)] - \frac{L+\xi-\delta c}{2}\cos k_{pe}(L+\xi)
\end{aligned}
\tag{C.30}
$$

Comparison between two rise profiles

In the following, we compare the wakefield component $f(\xi)$ for the two different bunch rise profiles. It is considered that the total length of the bunch is 3000 μm (10 ps). The plasma period T_p is 1 ps (wavelength λ_p=300 μm). Firstly we consider the wakefield acted on the bunch with different linear rise times. In Figure C.1, the rise time is 0, $0.5T_p$, T_p, $1.5T_p$, and $2T_p$, respectively. It can be seen that all these fields are positive, which means they are all a focusing force on the long bunch. For bunch with a sharp edge (rise time= 0), the wakefield is fully periodic (the minimum is 0) and the seeding for self-modulation is the strongest. The larger the rise time, the smaller the wakefield amplitude.

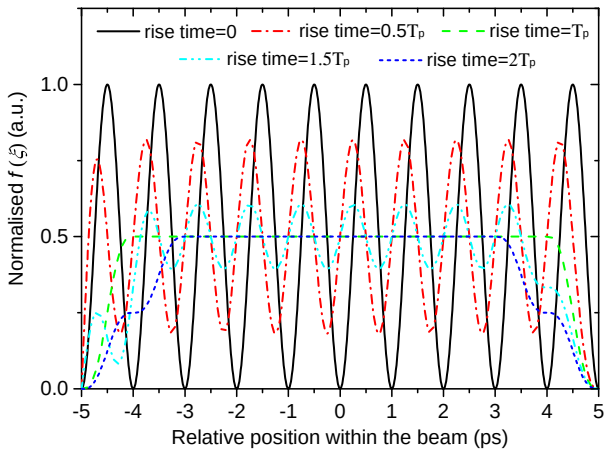


Figure C.1: Comparison of the transverse wakefield component $f(\xi)$ for bunches with different linear rise times.

Interestingly, the wakefield for bunches with rise times of T_p and $2T_p$ has a flat top in the middle, meaning that the bunch is unlikely to experience self-modulation. We can confirm this from Equation C.23. When the rise time $\delta = nT_p$, $\sin k_{pe}(\xi - L) = \sin k_{pe}(\xi + \delta c - L)$ in Equation C.23. In this case the oscillating component produced by the middle part is cancelled by the rise part of the bunch. Therefore $f(\xi)$ is constant in the middle as plotted in Figure C.1.

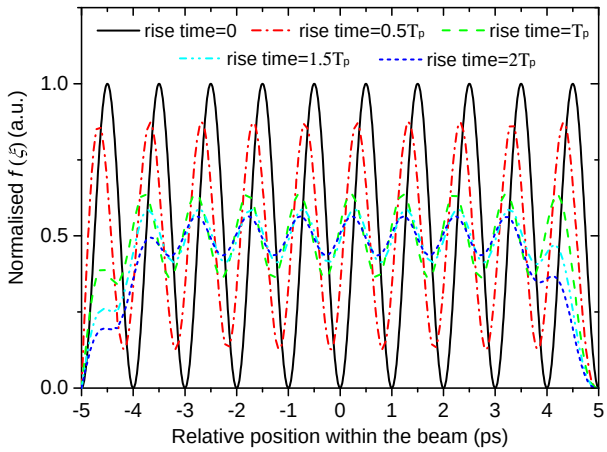


Figure C.2: Comparison of the transverse wakefield component $f(\xi)$ for bunches with different sinusoidal rise times.

We next compare the wakefield component for bunches with different sinusoidal rise times. In Figure C.2, the rise time is 0, $0.5T_p$, T_p, $1.5T_p$, and $2T_p$, respectively. Unlike the uniform bunch with a linear rise time, the wakefield component $f(\xi)$ oscillates for a sinusoidal rise bunch, even when the rise time equals to nT_p. As shown in Equations C.26 and C.29, the oscillating wakefield produced by the middle part of the bunch cannot be cancelled by the rise part.

Appendix D

THz detectors

The development of THz detectors has always been synchronised with the development of THz sources. There are many approaches for the detection of THz radiation based on different physical mechanisms. Two mechanisms, thermal detectors and Schottky barrier diodes are discussed in the following section.

Thermal detectors

In thermal detectors the EM radiation energy is absorbed by certain materials so that their temperatures are changed. The variation of temperature is related with the change of some other physical properties, such as the electrical resistance (in bolometer), the volume of gas (in Golay cell), and electrical charge (in pyroelectric), which can be transformed into voltage signals for measurements [12]. These detectors are normally broadband but with one common disadvantage, which is the relative slow responsivity. Normally, cryogenic cooling is required for bolometers, which could ensure a flat response and excellent responsivity (up to few 10^6 V/W) for THz frequencies from 0.15 THz to 20 THz. The Golay cell is an opto-acoustic detector and is designed to operate at room temperature. The responsivity is from more than 10^4 V/W at 0.02 THz to less than 5000 V/W at 20 THz [85]. This makes it suitable for the measurement of THz signals with moderate to high intensity. In the case of pyroelectric detector, the operating frequency covers most of the THz spectrum, with

relative low responsivity from 2600 V/W at 0.02 THz to around 600 V/W at 3 THz [85].

Schottky barrier diodes

Schottky barrier diode is named after a German physicist Walter H. Schottky. The mechanism follows. A potential energy barrier for electrons is formed by the junction of a semiconductor with a metal and this characteristic makes it suitable as a diode. By applying a sufficient forward voltage on the metal-semiconductor junction, a forward current can be generated. This property has been used for the detection of EM radiation.

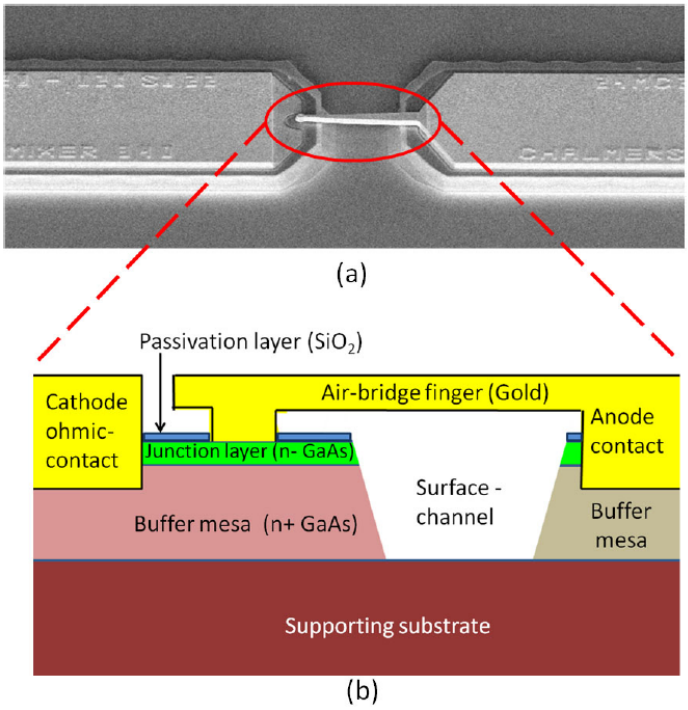


Figure D.1: (a) Scanning electron micrograph of a planar Schottky diode; (b) Schematic cross-section of the diode [86].

The typical structure of a planar Schottky barrier diode (SBD) is shown in Figure D.1. A metal-semiconductor junction is formed by connecting a low-doped n-type Gallium Arsenide layer (GaAs, green colour) with a narrow metal finger (gold). The finger is connected with a large anode contact pad. The cathode ohmic contact and the anode contact are separated by a surface channel (air) with a distance of several micrometres. The diode is supported by a semi-insulating GaAs substrate. Compared with silicon diodes, Schottky diodes have a lower

forward voltage requirement, which means higher switching speed and better efficiency.

Schottky barrier diodes have a fast response time and can be used for broadband detection or for specific frequency ranges by coupling to antennas or waveguide structures as filters. There are a number of zero-bias Schottky barrier diode (ZBD) detectors developed using rectangular waveguide housings (as high-pass filters). Here "zero-bias" means no bias voltage is required to overcome the barrier potential. The typical measured current-voltage characteristic of the zero-bias WR-10 Schottky detector diode is shown in Figure D.2.

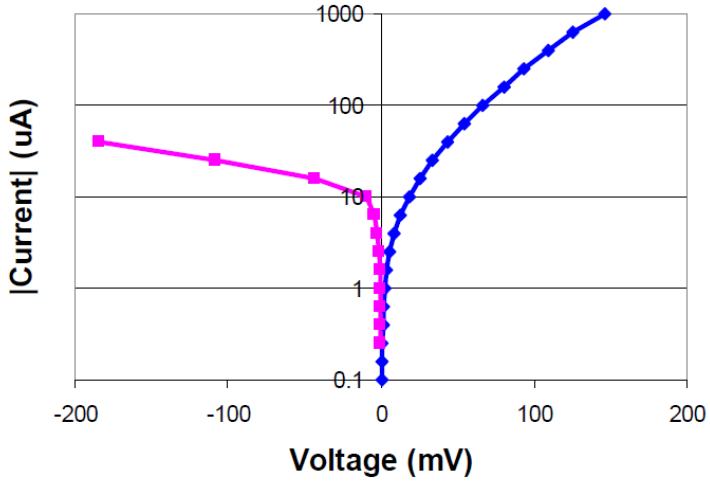


Figure D.2: Measured current-voltage characteristic of the zero-bias WR-10 Schottky detector diode [87].

There are a series of ZBD THz detectors developed by Virginia Diodes, Inc. The operating frequency is from 0.1 THz to 1.7 THz with typical responsivity range from around 2000 V/W at 0.1 THz to 100 V/W at 1.7 THz [69].

Bibliography

[1] S. S. Dhillon, M. S. Vitiello, E. H. Linfield, A. G. Davies, M. C. Hoffmann, J. Booske, C. Paoloni, M. Gensch, P. Weightman, G. P. Williams et al. *Journal of Physics D: Applied Physics*, **50**, 4 (2017) 043001.

[2] M. Naftaly. "Terahertz Metrology". Artech House (2015).

[3] J. F. Federici, B. Schulkin, F. Huang, D. Gary, R. Barat, F. Oliveira & D. Zimdars. *Semiconductor Science and Technology*, **20**, 7 (2005) S266.

[4] A. G. Davies, A. D. Burnett, W. Fan, E. H. Linfield & J. E. Cunningham. *Materials today*, **11**, 3 (2008) 18–26.

[5] T. May, G. Zieger, S. Anders, V. Zakosarenko, H. G. Meyer, M. Schubert, M. Starkloff, M. Rößler, G. Thorwirth & U. Krause. *Proc. SPIE*, **7309** (2009) 73090E.

[6] D. M. Mittleman, R. H. Jacobsen, R. Neelamani, R. G. Baraniuk & M. C. Nuss. *Applied Physics B: Lasers and Optics*, **67**, 3 (1998) 379–390.

[7] E. Gerecht, K. O. Douglass & D. F. Plusquellic. *Optics express*, **19**, 9 (2011) 8973–8984.

[8] K. Ishigaki, M. Shiraishi, S. Suzuki, M. Asada, N. Nishiyama & S. Arai. *Electronics letters*, **48**, 10 (2012) 582–583.

[9] C. Kulesa. *IEEE Transactions on Terahertz Science and Technology*, **1**, 1 (2011) 232–240.

[10] A. I. McIntosh, B. Yang, S. M. Goldup, M. Watkinson & R. S. Donnan. *Chemical Society Reviews*, **41**, 6 (2012) 2072–2082.

[11] Y. Kawano. *Contemporary Physics*, **54**, 3 (2013) 143–165.

[12] E. Brundermann, H.-W. Hubers & M. F. Kimmitt. "Terahertz techniques". Springer (2012).

[13] R. A. Lewis. *Journal of Physics D: Applied Physics*, **47**, 37 (2014) 374001.

[14] G. Dodel. *Infrared physics & technology*, **40**, 3 (1999) 127–139.

[15] "Edinburgh Instruments FIR System (7.5 THz to 0.25 THz)". `https://www.edinst.com/products/firl-100-pumped-fir-system/`.

[16] M. A. Belkin & F. Capasso. *Physica Scripta*, **90**, 11 (2015) 118002.

[17] B. S. Williams, S. Kumar, Q. Hu & J. L. Reno. *Electronics letters*, **42**, 2 (2006) 89–91.

[18] L. Li, L. Chen, J. Zhu, J. Freeman, P. Dean, A. Valavanis, A. G. Davies & E. H. Linfield. *Electronics Letters*, **50**, 4 (2014) 309–311.

[19] A. Wade, G. Fedorov, D. Smirnov, S. Kumar, B. S. Williams, Q. Hu & J. L. Reno. *Nature Photonics*, **3**, 1 (2009) 41–45.

[20] G. L. Carr, M. C. Martin, W. R. McKinney, K. Jordan, G. R. Neil & G. P. Williams. *Nature*, **420**, 6912 (2002) 153–156.

[21] S. Bielawski, C. Evain, T. Hara, M. Hosaka, M. Katoh, S. Kimura, A. Mochihashi, M. Shimada, C. Szwaj, T. Takahashi et al. *Nature Physics*, **4**, 5 (2008) 390–393.

[22] A. M. Cook, R. Tikhoplav, S. Y. Tochitsky, G. Travish, O. B. Williams & J. B. Rosenzweig. *Physical review letters*, **103**, 9 (2009) 095003.

[23] G. Andonian, O. Williams, X. Wei, P. Niknejadi, E. Hemsing, J. B. Rosenzweig, P. Muggli, M. Babzien, M. Fedurin, K. Kusche et al. *Applied Physics Letters*, **98**, 20 (2011) 202901.

[24] S. Antipov, M. Babzien, C. Jing, M. Fedurin, W. Gai, A. Kanareykin, K. Kusche, V. Yakimenko & A. Zholents. *Physical review letters*, **111**, 13 (2013) 134802.

[25] Z. Zhang, L. Yan, Y. Du, Z. Zhou, X. Su, L. Zheng, D. Wang, Q. Tian, W. Wang, J. Shi et al. *Physical review letters*, **116**, 18 (2016) 184801.

[26] J. H. Booske, R. J. Dobbs, C. D. Joye, C. L. Kory, G. R. Neil, G.-S. Park, J. Park & R. J. Temkin. *IEEE Transactions on Terahertz Science and Technology*, **1**, 1 (2011) 54–75.

[27] V. L. Ginzburg. *Physica Scripta*, **1982**, T2A (1982) 182.

[28] A. P. Potylitsyn. *Nuclear Instruments and Methods in Physics Research Section B: Beam Interactions with Materials and Atoms*, **145**, 1-2 (1998) 169–179.

[29] G. Doucas, V. Blackmore, B. Ottewell, C. Perry, P. G. Huggard, E. Castro-Camus, M. B. Johnston, J. L. Hughes, M. F. Kimmitt, B. Redlich et al. *Physical Review Special Topics-Accelerators and Beams*, **9**, 9 (2006) 092801.

[30] H. L. Andrews, F. Bakkali Taheri, J. Barros, R. Bartolini, V. Bharadwaj, C. Clarke, N. Delerue, G. Doucas, N. Fuster-Martinez, M. Vieille-Grosjean, I. V. Konoplev, M. Labat, S. Le Corre, C. Perry, A. Reichold & S. Stevenson. *Physical Review Special Topics - Accelerators and Beams*, **17** (2014) 1–13.

[31] S. I. Bajlekov, M. Heigoldt, A. Popp, J. Wenz, K. Khrennikov, S. Karsch & S. M. Hooker. *Physical Review Special Topics - Accelerators and Beams*, **16** (2013) 1–14.

[32] T. J. Maxwell, C. Behrens, Y. Ding, A. S. Fisher, J. Frisch, Z. Huang & H. Loos. *Physical Review Letters*, **111** (2013) 1–5.

[33] J. G. Neumann, R. B. Fiorito, P. G. OShea, H. Loos, B. Sheehy, Y. Shen & Z. Wu. *Journal of Applied Physics*, **105**, 5 (2009) 053304.

[34] Y. Shen, X. Yang, G. L. Carr, Y. Hidaka, J. B. Murphy & X. Wang. *Physical review letters*, **107**, 20 (2011) 204801.

[35] A. Aryshev, M. Shevelev, Y. Honda, N. Terunuma & J. Urakawa. *Applied Physics Letters*, **111**, 3 (2017) 033508.

[36] M. Shevelev, A. Aryshev, N. Terunuma & J. Urakawa. *Physical Review Accelerators and Beams*, **20**, 10 (2017) 103401.

[37] Y. Du, L. Yan, J. Hua, Q. Du, Z. Zhang, R. Li, H. Qian, W. Huang, H. Chen & C. Tang. *Review of Scientific Instruments*, **84**, 5 (2013) 053301.

[38] S. Antipov, C. Jing, M. Fedurin, W. Gai, A. Kanareykin, K. Kusche, P. Schoessow, V. Yakimenko & A. Zholents. *Physical review letters*, **108**, 14 (2012) 144801.

[39] P. Muggli, V. Yakimenko, M. Babzien, E. Kallos & K. P. Kusche. *Physical review letters*, **101**, 5 (2008) 054801.

[40] Y.-E. Sun, P. Piot, A. Johnson, A. H. Lumpkin, T. J. Maxwell, J. Ruan & R. Thurman-Keup. *Physical review letters*, **105**, 23 (2010) 234801.

[41] N. Kumar, A. Pukhov & K. Lotov. *Physical review letters*, **104**, 25 (2010) 255003.

[42] Y. Fang, V. E. Yakimenko, M. Babzien, M. Fedurin, K. P. Kusche, R. Malone, J. Vieira, W. B. Mori & P. Muggli. *Physical review letters*, **112**, 4 (2014) 045001.

[43] S. J. Smith & E. M. Purcell. *Physical Review*, **92**, 4 (1953) 1069.

[44] G. Toraldo Di Francia. *Il Nuovo Cimento (1955-1965)*, **16**, 1 (1960) 61–77.

[45] P. M. Van den Berg. *JOSA*, **63**, 12 (1973) 1588–1597.

[46] P. M. Van den Berg & T. H. Tan. *JOSA*, **64**, 3 (1974) 325–328.

[47] O. Haeberlé, P. Rullhusen, J. M. Salomé & N. Maene. *Physical Review E*, **49**, 4 (1994) 3340.

[48] A. S. Kesar, M. Hess, S. E. Korbly & R. J. Temkin. *Physical Review E*, **71**, 1 (2005) 016501.

[49] J. H. Brownell, J. Walsh & G. Doucas. *Physical Review E*, **57**, 1 (1998) 1075.

[50] G. Doucas, M. F. Kimmitt, A. Doria, G. P. Gallerano, E. Giovenale, G. Messina, H. L. Andrews & J. H. Brownell. *Physical review special topics-accelerators and beams*, **5**, 7 (2002) 072802.

[51] J. H. Brownell & G. Doucas. *Physical review special topics-accelerators and beams*, **8**, 9 (2005) 091301.

[52] A. P. Potylitsyn. *Nuclear Instruments and Methods in Physics Research Section B: Beam Interactions with Materials and Atoms*, **145**, 1-2 (1998) 60–66.

[53] D. V. Karlovets. *Journal of Experimental and Theoretical Physics*, **113**, 1 (2011) 27.

[54] D. Y. Sergeeva, A. P. Potylitsyn, A. A. Tishchenko & M. N. Strikhanov. *Optics Express*, **25**, 21 (2017) 26310–26328.

[55] C. Nieter & J. R. Cary. *Journal of Computational Physics*, **196**, 2 (2004) 448–473.

[56] K. S. Yee, D. Ingham & K. Shlager. *IEEE Transactions on Antennas and Propagation*, **39**, 3 (1991) 410–413.

[57] D. V. Karlovets & A. P. Potylitsyn. *Physical Review Special Topics-Accelerators and Beams*, **9**, 8 (2006) 080701.

[58] I. Blumenfeld, C. E. Clayton, F. J. Decker, M. J. Hogan, C. Huang, R. Ischebeck, R. Iverson, C. Joshi, T. Katsouleas, N. Kirby et al. *Nature*, **445**, 7129 (2007) 741.

[59] M. Litos, E. Adli, W. An, C. I. Clarke, C. E. Clayton, S. Corde, J. P. Delahaye, R. J. England, A. S. Fisher, J. Frederico et al. *Nature*, **515**, 7525 (2014) 92.

[60] A. Caldwell, K. Lotov, A. Pukhov & F. Simon. *Nature Physics*, **5** (2009) 363–367.

[61] AWAKE Collaboration. *Nature*, **561** (2018) 363–367.

[62] S. W. T. Katsouleas, J. M. Su & J. J. Dawson. *Part. Accel*, **22** (1987) 81–99.

[63] Y. Fang, J. Vieira, L. D. Amorim, W. Mori & P. Muggli. *Physics of Plasmas*, **21**, 5 (2014) 056703.

[64] R. Govil, W. P. Leemans, E. Y. Backhaus & J. S. Wurtele. *Physical review letters*, **83**, 16 (1999) 3202.

[65] P. Muggli, B. Allen, V. E. Yakimenko, J. Park, M. Babzien, K. P. Kusche & W. D. Kimura. *Physical Review Special Topics-Accelerators and Beams*, **13**, 5 (2010) 052803.

[66] J. Vieira, L. D. Amorim, Y. Fang, W. B. Mori, P. Muggli & L. Silva. *Plasma Physics and Controlled Fusion*, **56**, 8 (2014) 084014.

[67] K.-J. Kim. *Nuclear Instruments and Methods in Physics Research Section A: Accelerators, Spectrometers, Detectors and Associated Equipment*, **275**, 2 (1989) 201–218.

[68] "Virginia Diodes Zero Bias Detectors - VDI Model: WR2.2ZBD". `http://vadiodes.com/index.php/en/products/detectors?id=122/`.

[69] "Virginia Diodes, VDI Zero Bias Detector Specifications". `http://vadiodes.com/en/products-6/detectors`.

[70] P. Piot, Y. E. Sun, T. J. Maxwell, J. Ruan, A. H. Lumpkin, M. M. Rihaoui & R. Thurman-Keup. *Applied Physics Letters*, **98** (2011) 1–4.

[71] G. L. Bourdet & A. G. Orszag. *Applied optics*, **18**, 2 (1979) 225–7.

[72] F. Bien, M. Camac, H. J. Caulfield & S. Ezekiel. *Applied optics*, **20**, 3 (1981) 400–3.

[73] "Bolometer System". `http://www.infraredlaboratories.com/Bolometers.shtml`.

[74] R. Winston. *J. Opt. Soc. Am.*, **60** (1970) 245–247.

[75] H. Harrison, G. Doucas, A. J. Lancaster, I. V. Konoplev, H. Zhang, A. Aryshev, M. Shevelev, N. Terunuma & J. Urakawa. *5th Int. Beam Instrumentation Conf.(IBIC'16), Barcelona*, pages 472–475.

[76] "10 Micron Wire Grid Polarizer". `https://www.purewavepolarizers.com/wire-grid-polarizers/10-micron-wire-far-ir-thz-polarizer`.

[77] V. Blackmore. "Determination of the Time Profile of Picosecond-Long Electron Bunches through the use of Coherent Smith-Purcell Radiation". Ph.D. thesis, University of Oxford (2008).

[78] A. Aryshev, A. Potylitsyn, G. Naumenko, M. Shevelev, K. Lekomtsev, L. Sukhikh, P. Karataev, Y. Honda, N. Terunuma & J. Urakawa. *Physical Review Accelerators and Beams*, **20**, 2 (2017) 024701.

[79] "Astra Manual". `http://www.desy.de/mpyflo/Astra-manual/Astra-Manual-V3.2.pdf`.

[80] H. Harrison, A. J. Lancaster, I. V. Konoplev, G. Doucas, A. Aryshev, M. Shevelev, N. Terunuma, J. Urakawa & P. G. Huggard. *Review of Scientific Instruments*, **89**, 3 (2018) 035116.

[81] "High Power Q-Switched Diode Pumped UV Lasers". `https://www.lumentum.com/en/products/laser-solid-state-q-switched-high-power-q-series`.

[82] O. Grimm & P. Schmüser. *10th biennial European Particle Accelerator Conference, Edinburgh*, pages 1040–1042.

[83] M. Reiser. "Theory and Design of Charged Particle Beams". Wiley-Vch (2008).

[84] K. Floettmann. *Physical Review Special Topics-Accelerators and Beams*, **6**, 3 (2003) 034202.

[85] "MICROTECH THz Detectors". `http://www.mtinstruments.com/thzdetectors/`.

[86] A. Y. Tang. "Modelling of terahertz planar Schottky diodes". Chalmers University of Technology (2011).

[87] J. L. Hesler & T. W. Crowe. *Proc. ISSTT*, pages 89–92.